Hypersonic Jayhawks Reusable Penetrating Hypersonic ISR Platform Design

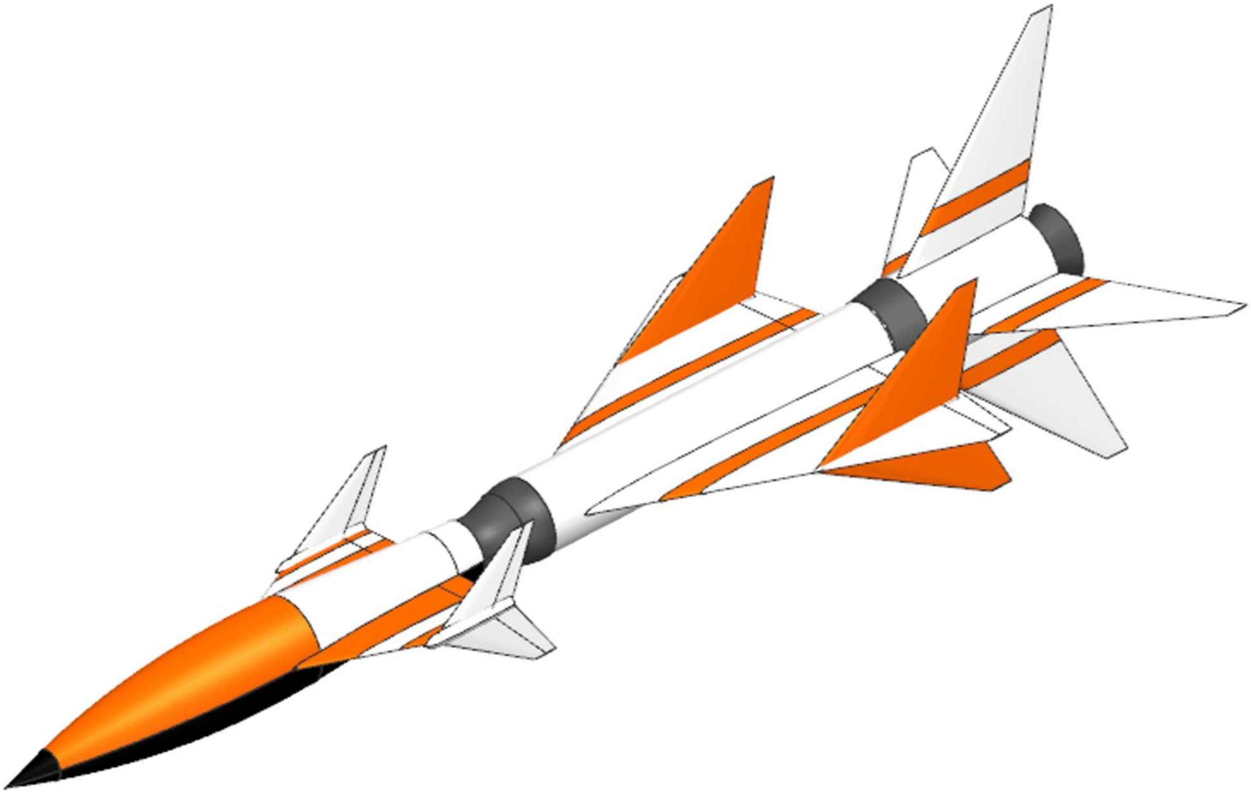

Team Members







Nathan Wolf	Gerell Miller	Zachary Rhodes	Justin Clough	Garin McKenna	Jack Schneider	Isaac Beech
Nathan Wolf	Gerell Miller	Zachary Rhodes	Justin Clough	Garin McKenna	Jack Schneider	Isaac Beech
ID: 998647	ID: 1253067	ID: 1013785	ID: 1340125	ID: 1356191	ID: 965150	ID: 1194272

Team Advisor
Dr. Ron Barrett
ID: 022393

KU THE UNIVERSITY OF KANSAS

ACKNOWLEDGEMENTS

The team would like to take this opportunity to thank several groups of people and individuals who have influenced the design work completed in this project. Firstly, we would like to thank our parents and families for supporting us in our youth and for encouraging us to pursue our dreams in the field of aerospace engineering. Secondly, we would like to thank the subject matter experts who provided insight into the various aspects of this design. Finally, we would like to acknowledge Dr. Ron Barrett for his support throughout this project.

COMPLIANCE MATRIX

RFP Requirement	Demonstrated	Page No.
Cruise speed: Mach 5 (threshold), Mach 8 (objective)	Mach 10	36
Cruise altitude: 80 kft (threshold), 100 kft (objective)	328 kft (Karman line)	36
Maximum range: 2500 nautical miles (threshold), 3000 nautical miles (objective)	3000+ nmi	38/44, 47
Takeoff/Landing: traditional landings on paved runways; required runway length should not exceed 8000 ft	GPS guided parachute landing	42
Mission: capable of performing both round-trip missions and one-way missions	One way (endo-atmospheric) Round-trip (exo-atmospheric)	43,44 46,47
Pilot: remotely piloted, unmanned system	Autonomous with optional command inputs from ground station	55
Reusability: reusable, with turn-around time between sorties not to exceed 24 hours	Baby Jay reusable within 24 hours	43/44, 46/47
Payload: ISR payload (3x3x12ft), weighing 1000 lb, requiring 2000 Watts of power, 2 downward facing windows with a diameter of 12 inches transparent for EO/IR imager (contiguous to the payload space). Provide options for RF antenna aperture (1x2 ft) on both sides of the fuselage.	3x3x12ft ISR payload with options for 1x2ft RF antennas 2 downward EO/IR windows 2000 Watts of ISR payload	52, 42, 55
Costing: Assume a production run of 100 aircraft over 10 years plus 5 aircraft for testing	RDT&E cost of 1,100 million USD and a cost per airframe of 520 million USD for 100 aircraft	91
Technology readiness: system initial operational capability (IOC) shall occur no later than December 2030.	All technology and systems have flight heritage on previous launch vehicles	Entire report

TABLE OF CONTENTS

LIST OF SYMBOLS

Acronym	Definition	Units
AEP	Airplane Estimated Price	USD
ATM	Adjusted Total Mass	~
BTM	Base Total Mass	~
COPUS	Committee on the Peaceful Uses of Outer Space	~
DME	Dry Mass Estimate	~
FCS	Flight Control Systems	~
IOC	Initial operating capability	~
ISR	Intelligence, surveillance, and target acquisition	~
OMS	Orbital Maneuvering System	~
OTV	Orbital test vehicle	~
PM	Payload Mass	
RDT&E	Research, Development, Test, and Evaluation	USD
RFP	Request for proposal	~
SATCOM	Satellite Communication	~
UN	United Nations	~
VPVHF	Vertically Polarized Very High Frequency	~
C_{Lu}	Lift Coefficient due to Forward Velocity	~
C_{Du}	Drag Coefficient due to Forward Velocity	~
C_{mu}	Pitching Moment Coefficient due to Forward Velocity	~
$C_{L\alpha}$	Lift Coefficient due to Angle of Attack	rad^{-1}
$C_{D\alpha}$	Drag Coefficient due to Angle of Attack	rad^{-1}
$C_{m\alpha}$	Pitching Moment Coefficient due to Angle of Attack	rad^{-1}
$C_{L}\dot{\alpha}$	Lift Coefficient due to Angle of Attack Rate	rad^{-1}
$C_{D}\dot{\alpha}$	Drag Coefficient due to Angle of Attack Rate	rad^{-1}
$C_{m}\dot{\alpha}$	Pitching Moment Coefficient due to Angle of Attack Rate	rad^{-1}
C_{Lq}	Lift Coefficient due to Pitch Rate	rad^{-1}
C_{Dq}	Drag Coefficient due to Pitch Rate	rad^{-1}
C_{mq}	Pitching Moment Coefficient due to Pitch Rate	rad^{-1}
$C_{L\delta el}$	Lift Coefficient due to Elevator Deflection Angle	rad^{-1}
$C_{m\delta el}$	Pitching Moment Coefficient due to Elevator Deflection Angle	rad^{-1}
$C_{y\beta}$	Side Force Coefficient due to Side Slip Angle	rad^{-1}
$C_{l\beta}$	Rolling Moment Coefficient due to Side Slip Angle	rad^{-1}
$C_{n\beta}$	Yawing Moment Coefficient due to Side Slip Angle	rad^{-1}

$C_y\dot{\beta}$	Side Force Coefficient due to Side Slip Angle Rate	rad^{-1}
$C_l\dot{\beta}$	Rolling Moment Coefficient due to Side Slip Angle Rate	rad^{-1}
$C_n\dot{\beta}$	Yawing Moment Coefficient due to Side Slip Angle Rate	rad^{-1}
C_{yp}	Side Force Coefficient due to Roll Rate	rad^{-1}
C_{lp}	Rolling Moment Coefficient due to Roll Rate,	rad^{-1}
C_{np}	Yawing Moment Coefficient due to Roll Rate	rad^{-1}
C_{yr}	Side Force Coefficient due to Yaw Rate	rad^{-1}
C_{lr}	Rolling Moment Coefficient due to Yaw Rate	rad^{-1}
C_{nr}	Yawing Moment Coefficient due to Yaw Rate	rad^{-1}
$C_{y\delta el}$	Side Force Coefficient due to Aileron Deflection Angle	rad^{-1}
$C_{l\delta el}$	Rolling Moment Coefficient due to Aileron Deflection Angle	rad^{-1}
$Cn\delta el$	Yawing Moment Coefficient due to Aileron Deflection Angle	rad^{-1}
$Cy\delta r$	Side Force Coefficient due to Rudder Deflection Angle	rad^{-1}
$Cl\delta r$	Rolling Moment Coefficient due to Rudder Deflection Angle	rad^{-1}
$Cn\delta r$	Yawing Moment Coefficient due to Rudder Deflection Angle	rad^{-1}
ωnsp	Short Period Natural Frequency	rad/s
ζsp	Short Period Damping Coefficient	~
ωnph	Phugoid Natural Frequency	rad/s
ζph	Phugoid Damping Coefficient	~
ωndr	Dutch Roll Natural Frequency	rad/s
ζdr	Dutch Roll Damping Coefficient	~

LIST OF TABLES

LIST OF FIGURES

1. INTRODUCTION, MISSION SPECIFICATION, AND PROFILE

The objective of this project is to respond to the 2021-2022 request for a proposal by AIAA to design a reusable penetrating hypersonic Intelligence, Surveillance, and Reconnaissance (ISR) platform. The platform must be unmanned, remotely piloted, and/or autonomous. In addition, the platform must be reusable and capable of carrying a piece of ISR equipment (details seen below in **Error! Reference source not found.**). The system may reuse components of existing aircraft or flight vehicles as needed. Finally, this report provides engineering analysis and total system design associated with this missile system including personnel effects. This report determines a system concept that best satisfies mission requirements and goals stated in the RFP and describes the design process, the physical and performance characteristics of the final system design and its components, operational concept, cost estimate, development plan, and necessary support equipment and other resources necessary to comply with the technical requirements [1].

Table 1-1: Technical requirements [1]

Cruise Speed	Mach 5 (threshold) – Mach 8+ (objective)
Cruise Altitude	80 kft (threshold) – 100 kft (objective)
Range	2,500 nmi (threshold) – 3,000 nmi (objective) Capable of both round-trip and one-way missions
Runway Length	≤ 8,000 ft
Control	Remotely piloted unmanned system (autonomy permitted but not required)
Turn-around time	≤ 24 hr
ISR payload	≥ 3 × 3 × 12 ft ISR volume ≥ 1,000 lb ISR mass ≥ 2,000 W ISR power 2 downward-looking 12 in diameter transparent windows for EO/IR imagery contiguous to the payload Provide option for 1 × 2 ft RF antenna located on both sides of the fuselage with minimal occlusion from vehicle and heat flux
Production rate	10 aircraft and 2 ground control stations per year for 10 years plus 5 aircraft and 2 ground stations for development testing
System IOC	≤ December 2030

1.1. ENDO-ATMOSPHERIC MISSION PROFILES

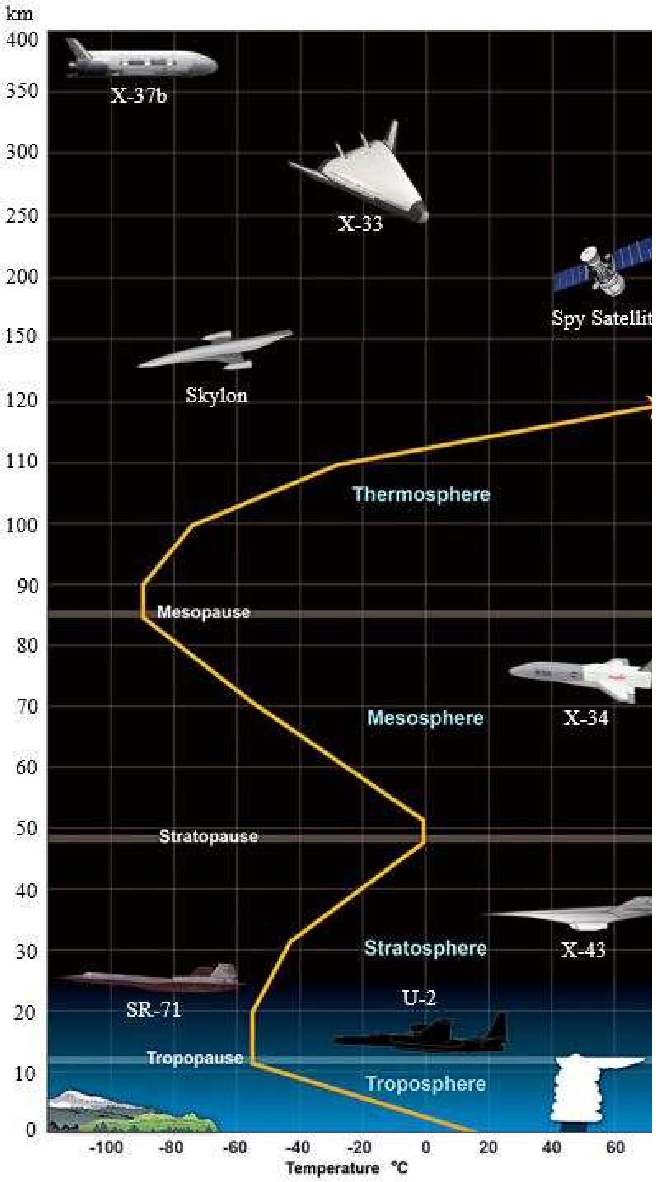

Figure 1.1.1: Historical ISR Platforms at Altitude

Based on initial technical requirements multiple mission profiles could satisfy this RFP. The primary differentiation between historical ISR platforms has been the altitude they operate at as seen on the right. Platforms such as the U-2 and the SR-71 operate in relatively low altitudes when compared to other ISR platforms. Both the SR-71 and the U-2 follow a rather conventional mission profile such as the one shown in Figure 1.1.2 wherein they takeoff from a friendly base and cruise to the target location using high altitude or a combination of altitude and speed to avoid detection and/or attack. Developed during the Cold War, these systems performed admirably. However, modern warfare and technology can easily see and intercept these aircraft leading to the retirement of the SR-71 and the limited use of the U-2 on targets that haven’t developed the sensors or technology to hit it.

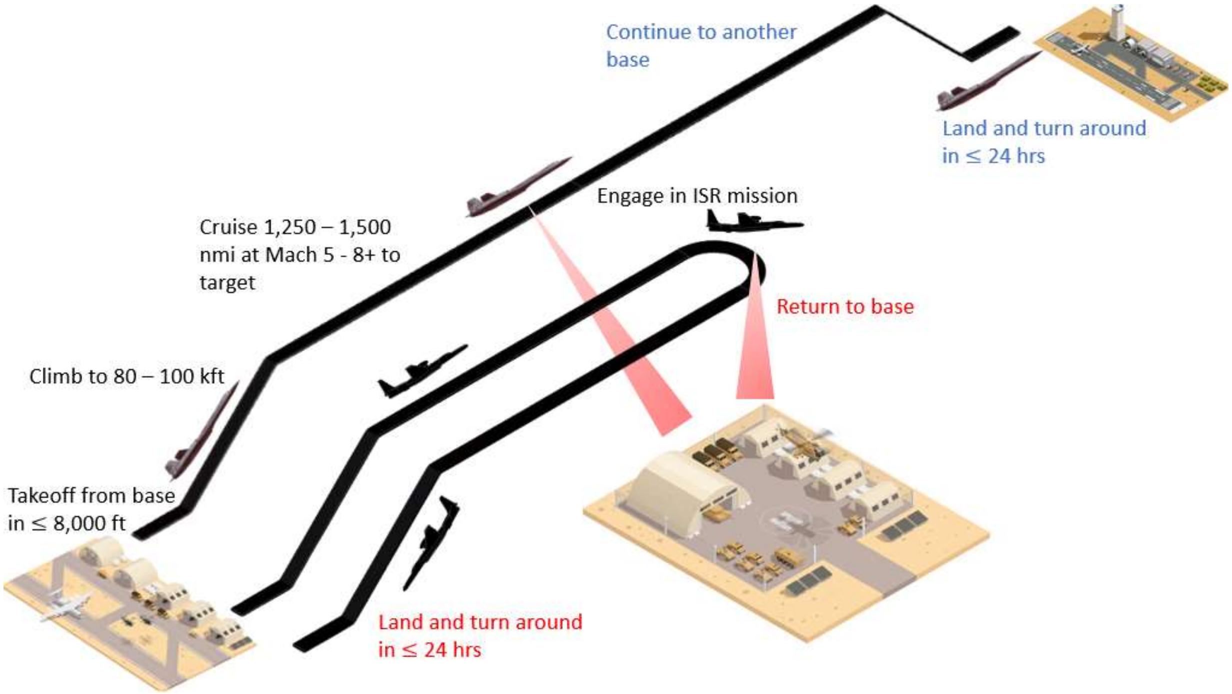

Figure 1.1.2: Endo-atmospheric mission profiles

1.2. EXO-ATMOSPHERIC ISR MISSION PROFILES

On the opposite side of the spectrum are modern spy satellites operating in low Earth orbit. Spy satellites have the benefit of being relatively safe since historically nations have been hesitant to engage other nations' satellite infrastructure, can have much larger sensors, and once deployed have a very long lifespan. However, satellites being targeted and destroyed is still possible. Some nations have successfully tested the technology to do so on their own decommissioned satellites. Satellites are also limited with what they can view as their orbits are relatively fixed and large maneuvers are extremely costly to make. They can be crippled in the case of a hardware issue as they are irreparable, and they are very expensive both to build and launch although this is a one-time price for a relatively long lifetime of service. The primary issue with satellites is that it takes multiple satellites to cover the orbits necessary to see all areas of the world and modern militaries and even enthusiasts can often determine satellite flight paths allowing countries to effectively hide from satellites when they pass overhead if they so desire.

Other ISR platforms, often called "space planes," span the altitudes between these two extremes as they ride the line between spacecraft and airplanes. Some of these can take off much like a traditional aircraft while others are deployed from another larger aircraft and still others are launched on a rocket, like satellites. They are usually more versatile in their missions and more maneuverable than satellites while avoiding the lower atmosphere that the SR-71 and U-2 operate in. Figure 1.2.1 illustrates a typical Exo-atmospheric mission profile.

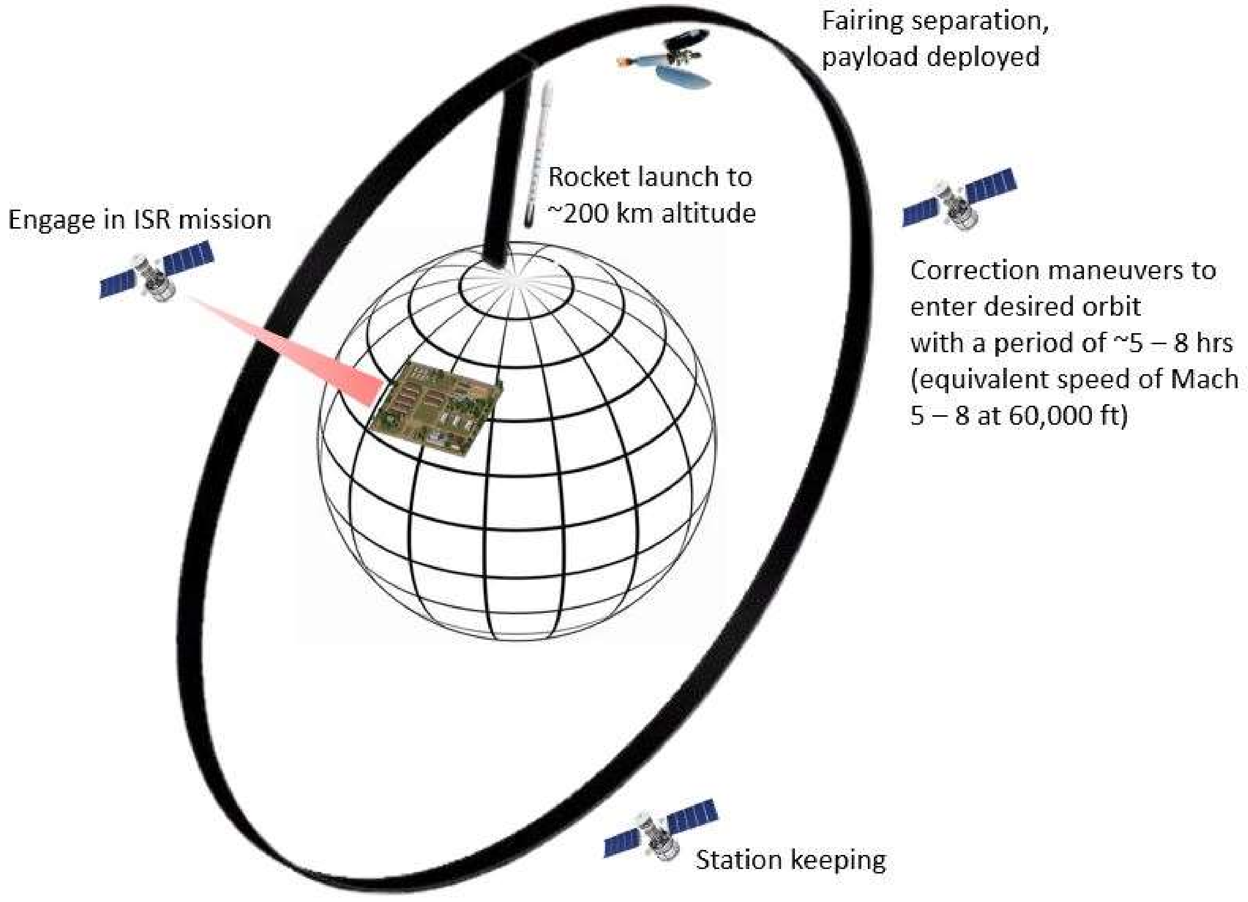

Figure 1.2.1: Possible Exo-atmospheric Mission Profile

1.3. EXO-ATMOSPHERIC PLATFORMS

Throughout the history of flying, aircraft have been pushed to higher speeds and altitudes. The development of this technology was and is still done often with experimental aircraft. One of these, the North American X-15, was a manned rocket-powered aircraft that could fly hypersonically. The aircraft achieved

Mach 6.7 at an altitude of slightly over 100K ft. This experimental aircraft first flew on June 8th of 1959 and the final flight was on October 24th, 1968. [2]

Figure 1.3.1: X-34 [3]

In 1996, NASA initiated the X-34 program, which was a demonstrator that was unmanned with high-altitude and high-speed capabilities. This aircraft was projected to have a top speed of Mach 8 at an altitude of 264K ft and was to deliver payloads to Low Earth Orbit at a less expensive price compared to the Space Shuttle. The aircraft had two glide flights before the program's contract expired on March 31, 2001. The first flight was on June 29th of 1999. During this flight, it used a Lockheed L-1011 as a mothership. NASA identified the risk of single-string avionics and the auto-land program when reassessing the program. [3]

Figure 1.3.2: X-37 [5]

As a follow-up to the X-34 program, the X-37B program was started. The X-37 is referred to as the Orbital Test Vehicle (OTV). The OTV was designed to be a reusable spacecraft that is fully autonomous. The X-37 has the capability of landing on runways like that of the Space Shuttle. The first glide flight of the OTV was on April 7, 2006. Then the first spaceflight was on April 22, 2010. The X-37B was designed to fly in an orbit at the range of 150-500 km with a mission duration of 270 days. The spacecraft has performed three missions with a flight duration of over 670 days, the longest being 779 days. It utilizes orbital-class rockets to launch the spacecraft into Low Earth Orbit, such as the Falcon 9 and Atlas V. The spacecraft was launched on May 17, 2020, and is still in orbit with an unknown landing date. [5]

2. ENDO-ATMOSPHERIC PLATFORMS

Figure 2.1: U-2 [6]

Dating back to the end of the second world war, United States intelligence deemed it necessary to develop an aircraft capable of undergoing reconnaissance missions to investigate the capabilities of the Soviet Union. The Lockheed U-2 was developed and brought into production to fulfill this need. The Lockheed U-2 was first introduced in 1956, and over the 34 years of its production, 104 U-2s were produced [6]. The U-2 is capable of high-altitude, subsonic flight, however, following the downing of Francis Gary Powers by the Soviet Union in May of 1960, the United States began to reevaluate their use of subsonic reconnaissance aircraft and began developing hypersonic platforms [7].

Figure 2.2: SR-71 [8]

Shortly after, Lockheed began the development of its new supersonic ISR aircraft, the SR-71 Blackbird. The SR-71 achieved its first test flight in the final weeks of 1964 before being fully introduced into use by the United States Air Force, and later NASA, in January of 1966. The SR-71 achieved its goal of reaching supersonic flight with a cruise speed of Mach 3.2 at an altitude of 85,000 feet. Although the Blackbird could outperform the U-2 regarding speed, range, and survivability, the program was eventually retired by the United States Air Force in 1998 and by NASA in 1999 due to its high costs [8].

Figure 2.3: Bomarc [9]

High-speed and high-altitude aircraft have also been used for other missions besides ISR. One example of this can be seen in the Boeing “Bomarc”. This aircraft, shown in Figure 2.3, was a ramjet powered surface-to-air missile in service from 1959 to 1972. The objective of this aircraft was to destroy incoming bomber aircraft by using either conventional or nuclear warheads. To deliver this payload, the aircraft climbed to 60,000 ft before leveling out and accelerating to Mach 2.5. It had a maximum range of 430 mi. [9]

3. INTERNATIONAL LAW

Performing ISR missions can greatly impact the political relationship between countries. The impact can be minimized by understanding international law regarding airspace and surveillance. When discussing airspace sovereignty, the agreement generally looked on is the Convention on International Civil Aviation, which states that each State has complete and exclusive sovereignty over the airspace above its territory. In this case flying an aircraft over another country without its permission could have negative political consequences and could be considered an act of war. Airspace has not been directly defined and outer space is a separate entity. This means if flown at a high enough altitude ISR platforms could avoid violating international law.

Laws regarding space are adopted through international treaties and organizations such as the United Nations (UN) and the International Telecommunication Union. An organization was established to handle outer space international space law. The Committee on the Peaceful Uses of Outer Space (COPUOS) has played an integral part in developing and amending international treaties regarding outer space. The Outer Space Treaty was the first such document drafted by COPUOS in 1967. This treaty set the basis for all laws and regulations regarding outer space. It established it as a space for all mankind, free of sovereignty claims. It also prohibited the militarization of outer space but was not specific and considered ineffective. The Liability Convention set the standards for liability of any damage, injuries, or death that were related to space activities. It stated that a group would be held responsible for any damage occurring on the earth's surface. There are a large number of treaties related to space usage, but it is important to note that some are not signed but certain countries and the legal restrictions may not be observed by all parties. A vehicle that can fly within the atmosphere, continue into space, re-enter the atmosphere, and continue flight enters an unrefined section in terms of legal development. The classifications and therefore legal restrictions and liability have not been outlined for such a vehicle. This means that under certain circumstances air law will apply and under others space law will apply. This provides an opportunity to potentially exploit the restrictions as they currently stand. A vehicle could fly either within the atmosphere or in space to avoid the consequences associated with one of the legal systems [10].

Another aspect to consider are international laws referring to espionage. These will likely not restrict the potential applications of the hypersonic missile being designed for this report but could make other options more viable. One such agreement is the Treaty of Open Skies. This allowed mutual observation between agreeing parties. The goal was to allow some knowledge to be gathered by each party to build trust and avoid conflict. However, recently groups have been withdrawing from this deal. The United States dropped in 2020 and then Russia in 2021 [10]. This makes ways to gain intelligence without inciting war or conflict extremely valuable. A vehicle being used in space holds less political risk than one that operates within other countries sovereign airspace. Established by the Chicago convention, air sovereignty is limited to the atmosphere, which was not directly defined. A widely accepted separation between the atmosphere and space is the Karman Line which is currently defined at an altitude of 100 kilometers or 60 miles [11].

4. GENERAL DESIGN PHILOSOPHY

The design philosophy of the Hypersonic Jayhawks is to provide a hypersonic ISR platform that delivers secure, reliable, and multi-spectral ISR missions over hostile areas with the lowest cost, chance for interception, and political impact.

5. OPTIMIZATION FUNCTION

This chapter outlines the generation of an optimization function used to evaluate preliminary designs. The requirements for the mission specification are such that if they are not met, the design will not be considered. As such, the values for each are binary. The requirements sourced from the RFP [1] are below.

Table 5-1: Design requirements [1]

R1	Cruise Speed	$\begin{cases} 1\ if\ capable\ of\ \geq Mach\ 5\ Cruise \\ 0\ if\ cruise\ speed < Mach\ 5\ Cruise \end{cases}$
R2	Cruise Altitude	$\begin{cases} 1\ if\ capable\ of\ \geq 80kft\ Cruise \\ 0\ if\ cruise\ altitude < 80kft \end{cases}$
R3	Maximum Range	$\begin{cases} 1\ if\ capable\ of\ \geq 2{,}500nm\ Range \\ 0\ if\ not\ capable\ of\ \geq 2{,}500nm\ Range \end{cases}$
R4	Take-off Distance	$\begin{cases} 1\ if\ TO/landing\ distance \leq 8{,}000ft \\ 0\ if\ TO/landing\ distance > 8{,}000ft \end{cases}$
R5	Capable of Round Trip	$\begin{cases} 1\ if\ capable\ of\ round\ trip \\ 0\ if\ not\ capable\ of\ round\ trip \end{cases}$
R6	Remotely Piloted or Autonomous	$\begin{cases} 1\ if\ remotely\ piloted\ or\ autonomous \\ 0\ if\ not\ remotely\ piloted\ or\ autonomous \end{cases}$
R7	Reusability	$\begin{cases} 1\ if\ capable\ of\ reuse\ in \leq 24\ hours \\ 0\ if\ not\ capable\ of\ reuse\ in\ 24\ hours \end{cases}$
R8	Payload Integration	$\begin{cases} 1\ if\ capable\ of\ accomodating\ a\ payload\ of\ 3x3x9ft \\ 0\ if\ not\ capable\ of\ accomodating\ a\ payload\ of\ 3x3x9ft \end{cases}$
R9	Payload Capacity	$\begin{cases} 1\ if\ capable\ of\ carrying\ payload\ \geq 1000lbm \\ 0\ if\ payload\ capacity\ < 1000lbm \end{cases}$
R10	ISR Electrical Power Capability	$\begin{cases} 1\ if\ capable\ of\ providing\ \geq 2000W\ electrical\ power \\ 0\ if\ capable\ of\ providing\ < 2000W\ electrical\ power \end{cases}$
R11	ISR Sensor Visibility	$\begin{cases} 1\ if\ it\ supports\ two\ 12in\ diameter\ windows \\ 0\ if\ it\ does\ not\ support\ two\ 12in\ diameter\ windows \end{cases}$
R12	RF Antenna Accommodation	$\begin{cases} 1\ if\ capable\ of\ accomodating\ two\ 1x2ft\ antenna\ ports \\ 0\ if\ not\ capable\ of\ accomodating\ 1x2ft\ anntena\ ports \end{cases}$
R13	Initial Operational Capability (IOC)	$\begin{cases} 1\ if\ IOC\ before\ 2030 \\ 0\ if\ IOC\ after\ 2030 \end{cases}$

Assuming a design meets all these requirements, it is then to be evaluated based on objectives. The following shows the quantification of these objectives and the definition of the definition of the optimization function. By using this optimization function, the team was able to make configuration decisions based on both the requirements that the design must meet as well as other desirable characteristics of each.

Table 5-2: Design and ancillary objectives

O1	Cruise Speed	$\begin{cases} \frac{Mach\ Number - 5}{3}\ if\ 5 < Mach\ Number < 8 \\ 10\ if\ Mach\ Number\ \geq 10 \end{cases}$
O2	Cruise Altitude	$\begin{cases} \frac{Cruise\ Altitude - 80{,}000ft}{20{,}000}\ if\ 80{,}000ft < Mach\ Number < 100{,}000ft \\ 10\ if\ Cruise\ Altitude\ \geq 100{,}000\ ft \end{cases}$
O3	Maximum Range	$\begin{cases} \frac{Maximum\ Range - 2{,}500nmi}{500}\ if\ 2{,}500nmi < Max\ Range < 3{,}000nmi \\ 10\ if\ Maximum\ Range\ \geq 3{,}000nmi \end{cases}$
O4	Minimum Cost	$\begin{cases} \frac{Cost_{Competitive\ System} - Cost_{Our\ System}}{Cost_{Competitive\ System}} \end{cases}$
O5	Capability to Maneuver	$\begin{cases} 1\ Capable\ of\ aerodynamic\ manuevers \\ 0\ not\ capable\ of\ aerodynamic\ manuevers \end{cases}$
AO1	Sensor Capabilities	$\begin{cases} \frac{1}{Max\ Sensor\ Resolution\ in\ cm}\ if\ 1\ cm < Resolution < 1000\ cm \\ 1\ if\ Resolution\ \leq 10 \end{cases}$
AO2	Beam Steering Capability	$\begin{cases} 1\ Capable\ of\ Beam\ Steering \\ 0\ if\ not\ capable\ of\ beam\ steering \end{cases}$
AO3	Probability of Communication Intercept	$\begin{cases} \frac{1}{\%\ Chance\ of\ Itercept/Year}\ if\ 1\% <\ Chance < 100\% \\ 1\ if\ \%\ Chance\ of\ Intercept\ \leq 1\% \end{cases}$
AO4	Observation Persistence	$\begin{cases} 1\ if\ observation\ period > 1\ minute \\ 0\ if\ observation\ period \leq 1\ minute \end{cases}$
AO5	Seismic Profile	$\begin{cases} 1\ if\ not\ possible\ to\ determine\ craft\ details\ with\ seismology \\ 0\ if\ not\ possible\ to\ determine\ craft\ details\ with\ seismology \end{cases}$
AO6	Ability to Resist Atmospheric Disturbances	$\begin{cases} 1\ if\ resistant\ to\ atmospheric\ disturbances \\ 0\ if\ not\ resistant\ to\ atmospheric\ disturbances \end{cases}$
AO7	Ability to Launch/Recover from a Small Area	$\begin{cases} 1\ if\ launch/recovery\ area < 100\ sq\ ft \\ 0\ if\ launch/recovery\ area \geq 100\ sq\ ft \end{cases}$
AO8	Suitability for Weaponization	$\begin{cases} 1\ if\ launch/recovery\ area < 100\ sq\ ft \\ 0\ if\ launch/recovery\ area \geq 100\ sq\ ft \end{cases}$
AO9	Potential to Escalate Conflict	$\begin{cases} 2\ if\ capable\ of\ operating\ without\ political\ consequence \\ 0\ if\ not\ capable\ of\ operating\ without\ political\ consequence \end{cases}$

Using these variables, the general form of the optimization equation is shown as:

$$OF = \prod_{i=1}^{13} R_i \left(\frac{1}{5} \sum_{i=1}^{5} O_j + \frac{1}{9} \sum_{i=1}^{9} AO_k \right)$$

6. STAMPED ANALYSIS

For the size of the designed system, the small lift launch vehicle category is best suited as its range of payload capabilities is less than 2000 kg. Data was collected for 188 different launching platforms including traditional rocket platforms and airplane launching systems. Out of these 66, different small lift launchers provide cost per kg values. Using this, cost per kg per kilometer ratios were made for all the systems the results of which can be shown below. This analysis demonstrates convergence of 100 \$/kg/km. This platform also allows for rapid reusability and versatile launching locations as some of these small lift launchers can be packed into shipping containers and transported in cargo aircraft [12]. The statistical time and market predictive engineering design (STAMPED) data was compiled and is shown in the figures below.

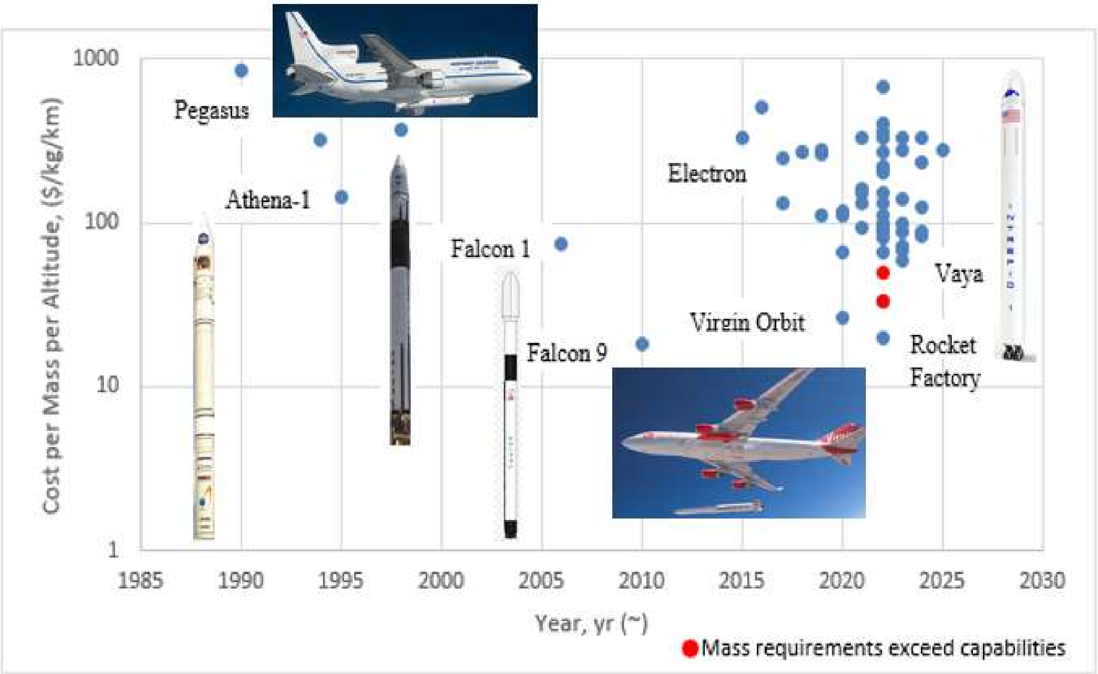

Figure 6.1: Cost per mass per altitude STAMPED Data

A similar process can also be conducted for other aircraft design parameters such as the: empty weight, takeoff weight, maximum takeoff weight (MTOW), wingspan (b), wing area (S), aspect ratio (AR), thrust, maximum velocity, cruise velocity, and the range of the aircraft. For this set of STAMPED data, 23 air and spacecraft were analyzed over 64 years from 1957 to 2021. The STAMPED data plots for each of these parameters can be seen in the subsequent figures.

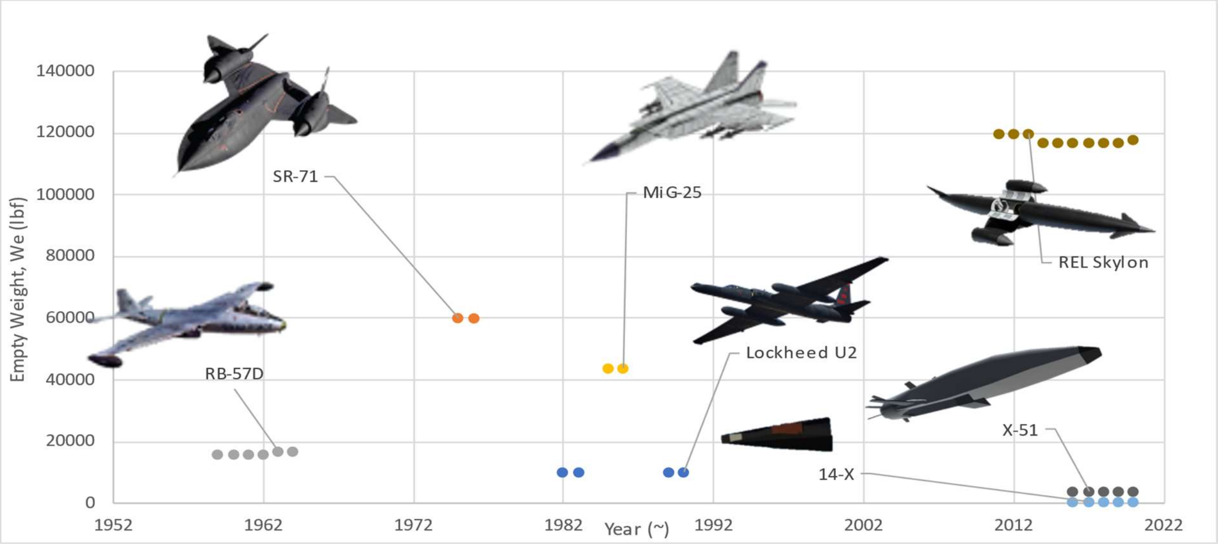

Figure 6.2: Empty weight STAMPED data for ISR and hypersonic aircraft

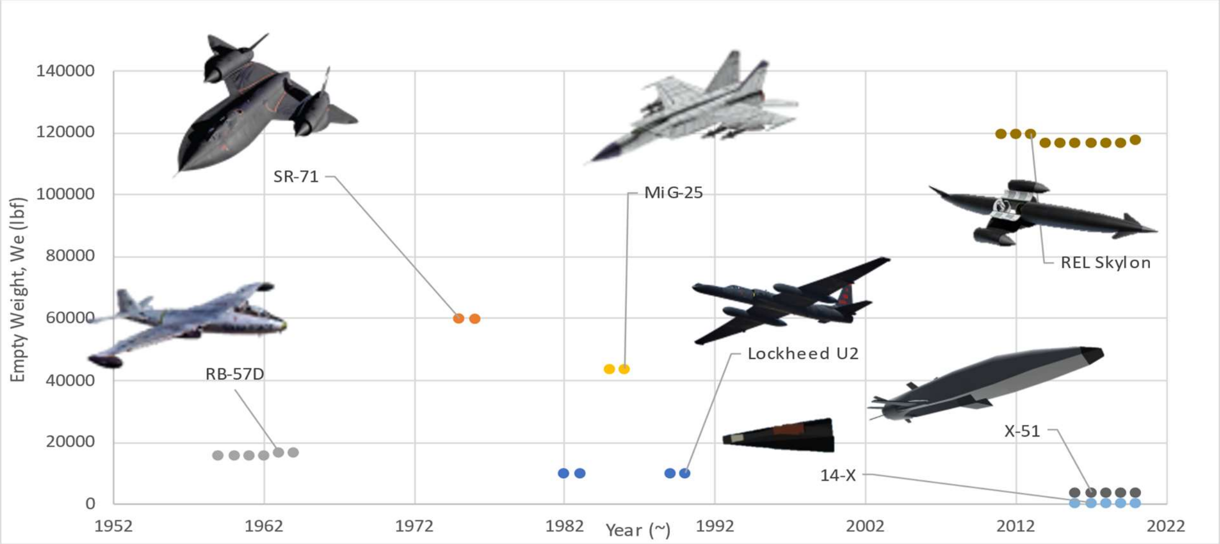

Figure 6.3: Empty weight STAMPED data for ISR and hypersonic aircraft

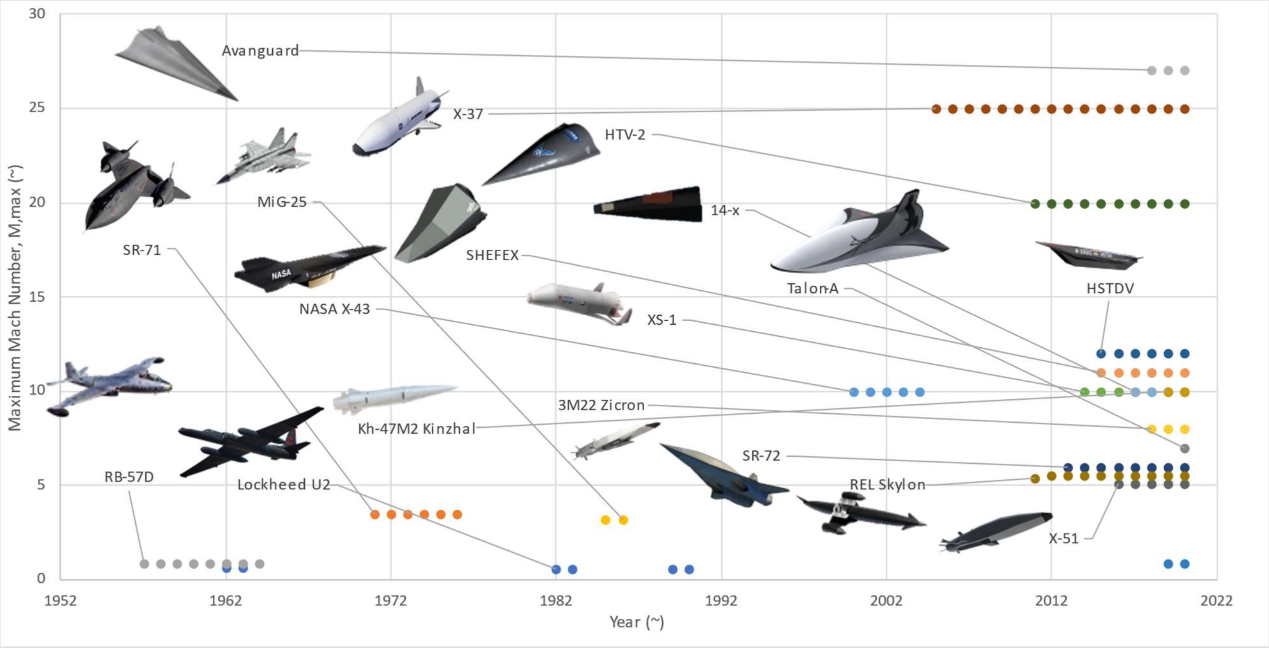

Figure 6.4: Maximum Mach number STAMPED data for ISR and hypersonic aircraft

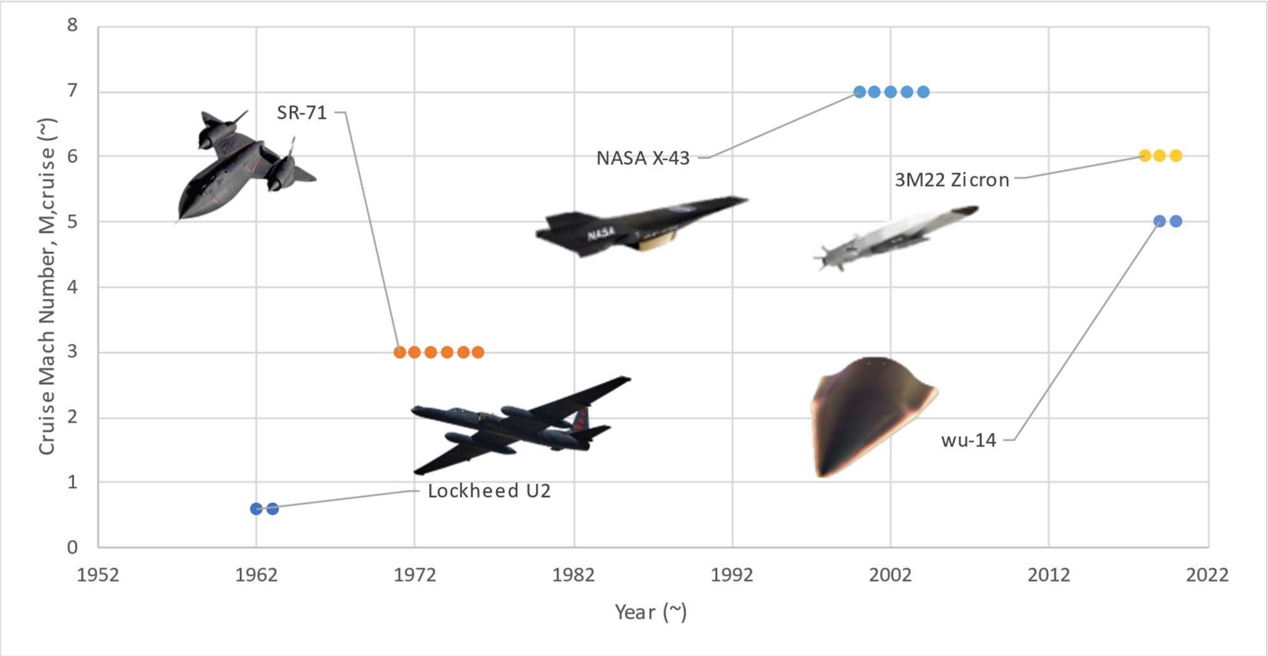

Figure 6.5: Cruise Mach number STAMPED data for ISR and hypersonic aircraft

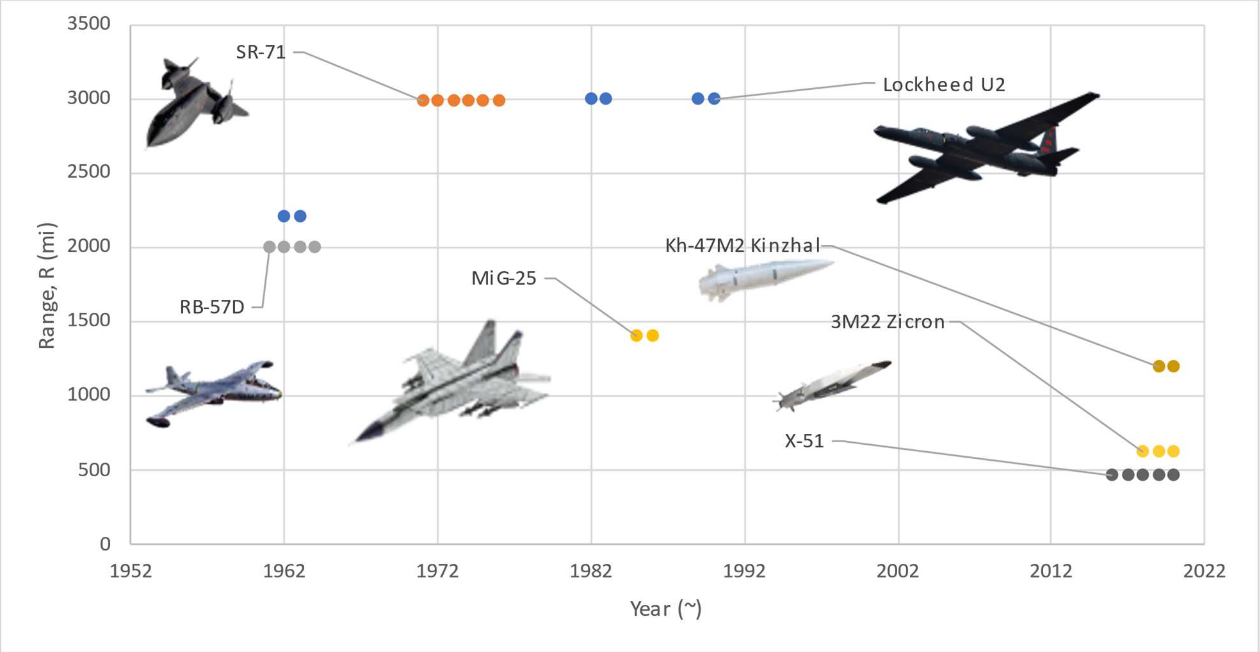

Figure 6.6: Range STAMPED data for ISR and hypersonic aircraft

As can be observed by the above figures, there is a non-trivial amount of data missing for STAMPED data techniques for these selected design parameters. It should be noted that due to the missing data for these design parameters, adequate trendlines could not be generated for the STAMPED analysis. This is largely because many of the reconnaissance or supersonic aircraft used in this analysis were not in service during the same years (with some of the only exceptions being for more modern aircraft) thus not allowing for standard deviations to be plotted. Even in the circumstances where the standard deviation trend lines could be plotted, there were some instances where negative values were reported, such as with the empty weight and max takeoff weight. Overall, for the STAMPED data techniques to be beneficial, more data would have to be made available for accurate trends to be developed.

7. PRELIMINARY WEIGHT SIZING OF TRADITIONAL SR-71 DESIGN, WHY IT'S NOT ACCEPTABLE

This chapter outlines the preliminary weight sizing of an endo-atmospheric and exo-atmospheric ISR platform to meet the RFP similar to the SR-71.

7.1. ENDO-ATMOSPHERIC WEIGHT SIZING

Using Dr. Jan Roskam’s *Airplane Design Part I: Preliminary Sizing of Airplanes* [13] initial values for various terms required for initial sizing can be found (seen in the Table at right). However, because of the high speed and altitude of the hypersonic ISR platform, Kristen Robert’s master’s thesis analyzing the performance of scramjet engines above Mach 4 [14] was used to gain accurate specific fuel consumption data for analysis.

Table 7.1-1: Technical information for weight sizing [13,14]

Term	Mach 5 (80,000 ft)
$c_{j_{cr}}$	2.57 lbs/lbs/hr
$(L/D)_{cr}$	6
R_{cr}	3,000 nmi
V_{cr}	2,900 kts
W_1/W_{TO}	0.99
W_2/W_1	0.995
W_3/W_2	0.995
W_4/W_3	0.92
W_6/W_5	0.985
W_7/W_6	0.992
W_{PL}	1,000 lb
$W_{F_{res}}$	10% of W_F

Once this was done reference 13, Section 2.4, Equation 2.9 can be used to find the weight fraction associated with the cruise stage of flight. Having all weight fractions calculated the mass fuel fraction can be found from reference 13, Section 2.4, Equation 2.13. Also, from reference 13, Section 2.4, Equation 2.14 the total weight of all fuel can be estimated. Finally, the empty weight can be calculated from reference 13, Section 2.1, Equation 2.4.

Equation 2.9: $R_{cr} = \left(V/c_{j_{cr}}\right) * \left(L/D\right)_{cr} * \ln\left(W_i/W_{i+1}\right)$

Equation 2.13: $M_{ff} = \left(W_1/W_{TO}\right)\prod_{i=1}^{i=7}\left(W_{i+1}/_{i}\right)$

Equation 2.14: $W_F = (1 - M_{ff})W_{TO} + W_{F_{res}}$

Equation 2.4: $W_E = W_{TO_{guess}} - W_F - W_{PL}$

Using hypersonic aircraft trends found on the figure of reference 13 the takeoff weight corresponding to the calculated empty weight can be found. If the takeoff weight found using this figure is not within 0.5% of the guessed takeoff weight, a new iteration is done with a new guess for the takeoff weight. This process was done for Mach 5 at 80,000 ft with the known takeoff weight of the SR-71 Blackbird as an initial guess. This process resulted in **Error! Reference source not found.** below:

Table 7.1-2: Converged values for weight sizing

Term	**Mach 5 (80,000 ft)**
W_{to}	258,000 lb

This estimated takeoff weight of 258,000 lb is reasonable being approximately 50% more than the known takeoff weight of the SR-71 which only reached a maximum speed of Mach 3.

7.2. ENDO-ATMOSPHERIC COST ANALYSIS - THE NAIL IN THE COFFIN

The purpose of this chapter is to present the costs associated with a theoretical SR-72, a modern equivalent of the SR-71. The cost analysis detailed by Roskam in *Airplane Design Part VIII: Airplane Cost Estimation: Design, Development, Manufacturing and Operating* [15] was used to assess the total costs. Using the methods above a code was created to estimate the cost of the SR-71 as it has a known cost per aircraft of approximately 34 million USD in 1962 (approximately 317 million USD in 2022). By calibrating the code to the known SR-71 cost a reasonable approximation of a Mach 5 ISR platform following the SR-71 design approach can be approximated.

Research, development, test and evaluation costs are given in Table 7.2-1 and Figure 7.2.1. Manufacturing, acquisition, operating, and total life cycle costs are given in Table 7.2-2. An estimated price per plane based on production runs is shown in Figure 7.2.2.

Table 7.2-1: RDT&E endo-atmospheric (Mach 5) cost analysis

RDT&E Stage	Cost (Million $)
Airframe Engineering Design Costs	$125,208
Development and Support Costs	$1,118
Flight Test Aircraft Cost	$44,895
Flight Test Operations Cost	$675
Test and Simulation Facilities Cost	$34,379
RDT&E Profit	$9,282
Cost to Finance RDT&E Phases	$10,778
Total RDT&E Cost	**$226,338**

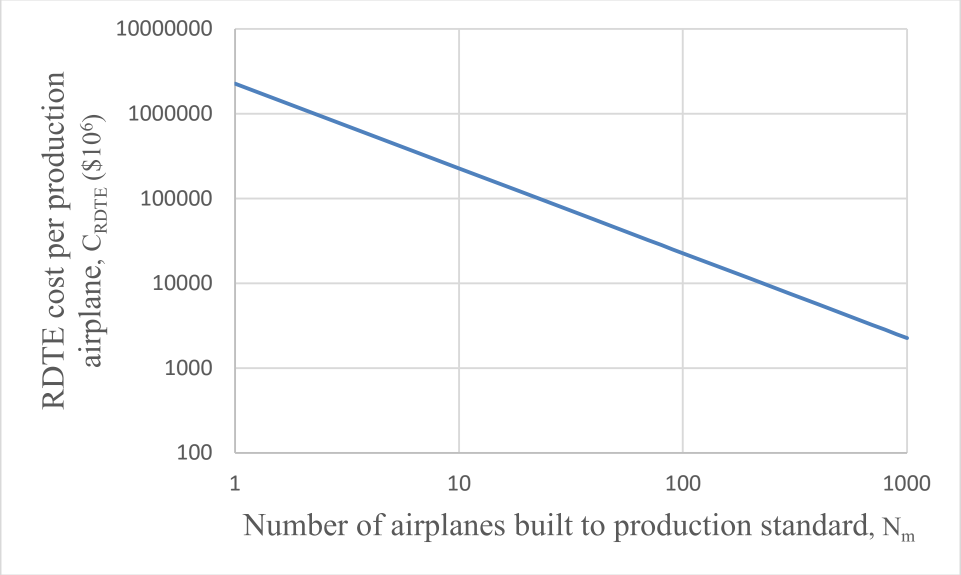

Figure 7.2.1: RDT&E cost per production airplane (logarithmic scale)

Table 7.2-2: Acquisition cost for endo-atmospheric solution (100 airframes)

Cost of Acquisition Breakdown	Cost (Million $)
Acquisition Cost	$87,124
Manufacturing Profit	$7,920
Manufacturing Cost	$79,204
Airframe Engineering and Design Cost	$19,212
Cost of Engineering and Avionics	$19,212
Aircraft Program Production Cost	$48,111
Labor Cost for Manufacturing	$38,912
Estimated Cost Per Airframe	**$1,097**

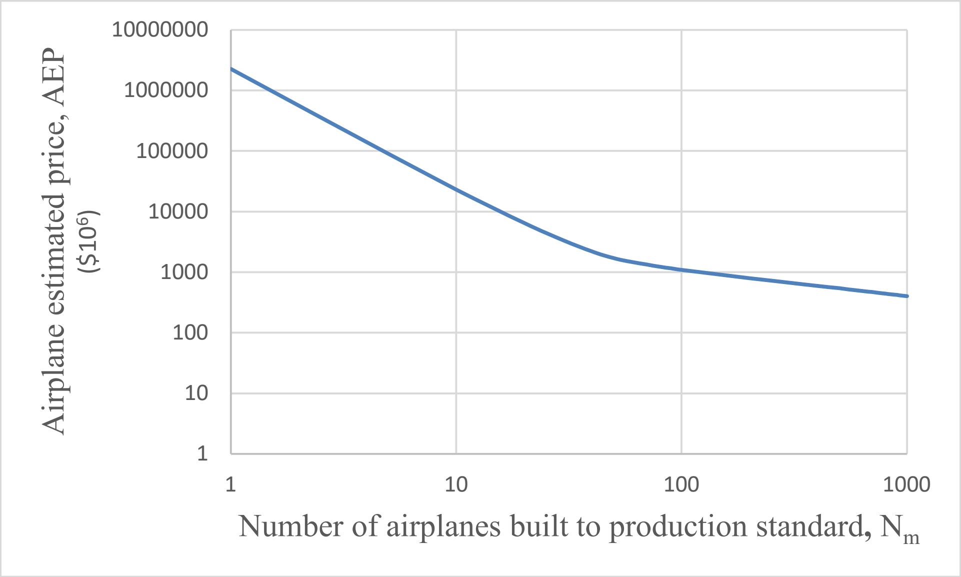

Figure 7.2.2: Airplane estimated price per production airplane (logarithmic scale)

As is evident in the Figures above, the cost of a traditional endo-atmospheric aircraft like the SR-71 would be over a billion USD per airframe and the RDTE would be several hundred billion USD. This would be extremely costly and most likely prohibitive to the development of the program. Therefore, if at all possible, methods other than traditional aircraft design should be employed to reduce cost.

8. EXO-ATMOSPHERIC APPROACH - THE LOGICAL SOLUTION

Exo-atmospheric sizing was conducted using the bottom-up method from *Space Mission Engineering: The New SMAD*. [16] The bottom-up method was developed from the RFP masses for a spacecraft design. The functions provided were created using an exponential best fit. [17] The base total mass (BTM) is the base dry mass of a spacecraft without additional consideration to the mission spec. The dry mass of a spacecraft is the entire mass of the space excluding propellant mass. The BTM was estimated using the 1000 lbm payload mass (PM) in Equation 8.1 The resultant BTM was 3988 lbm.

Equation 8.1: $BTM\ (lbm) = 105.38\ lbm\ (PM)^{0.594}$

Equation 8.2: $ATM = \frac{BTM}{(1-0.118)}$

Equation 8.3: $DME = \frac{ATM}{0.85}$

The BTM was used to calculate the Adjusted Total Mass (ATM). The ATM is an adjusted dry mass that considers unusual mission components such as payload power consumption, precise camera and attitude pointing, and high data usage. The ATM is 4522 lbs from the Equation 6.2. The ATM was used to approximate the Dry Mass Estimate (DME) of the vehicle in Equation 6.3. The DME is the final expected dry mass of the overall vehicle. The DME is calculated by adding 15% to the ATM as almost all flown mission will fall within 15%. The DME of the spacecraft is 5320 pounds mass.

8.1. PROPULSION SYSTEMS

Chemical propulsion converts energy stored in chemical bonds to thrust. This is done with monopropellant and bipropellant systems. Monopropellant systems differ from bipropellant ones in that they do not require an oxidizer. This has the advantage of being less expensive, lighter, and more reliable. The bipropellant system's complexity provides increased performance and efficiency. All chemical propulsion systems require a large amount of fuel to provide consistent thrust resulting in a limited burn time. This prevents their use in long-term orbital

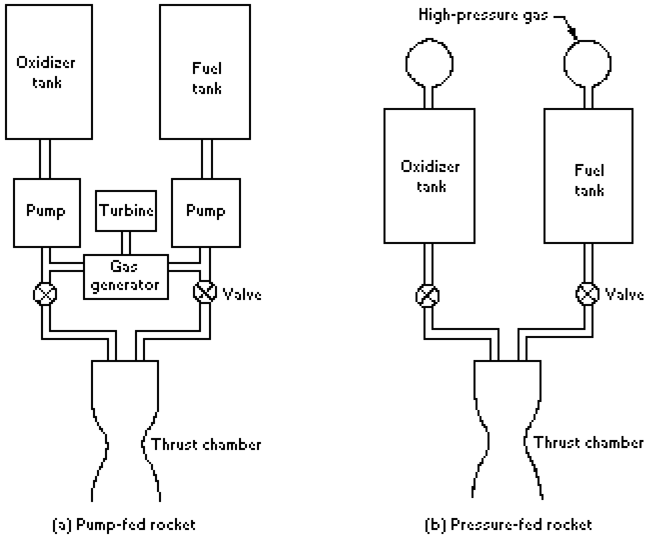

Figure 8.1: Schematic of liquid-propellant rocket [Error! Reference source not found.]

applications [19]. To provide long-term thrust, many high altitude and space vehicles use solar panels to capture the energy that can be used in electric propulsion systems.

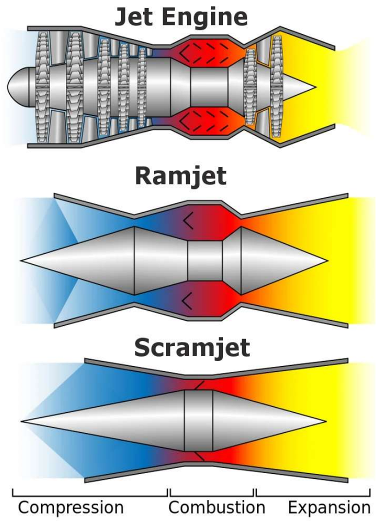

Figure 8.1.2: Air breathing engines [20]

Air breathing engines are limited by the density of the air and therefore the altitude. A scramjet can operate at high speeds and altitudes. Theoretically they can operate at up to 250,000 ft. While scramjets allow flight speeds above Mach 5, they are extremely inefficient at lower speeds. This means the aircraft would require another source of thrust to reach the scramjet's optimal Mach number [21]. Scramjets function by having air be compressed by the high flight speeds. The reason scramjets can only operate at such high speeds is they require immense airflow to remain supersonic in the engine [22].

A propulsion system that combines the attributes of cycle engines and rocket engines could provide a unique set of benefits for different mission requirements. By combining the principles of ducted jet engines and rocket engines they can provide a higher specific impulse than a standard rocket engine. There are multiple main ways these engines can be combined. Solid rocket propellant can be exhausted and then reconfigured into a ramjet chamber, or the systems can interoperate allowing increased air intake into the rocket exhaust. The rocket engine can burn fuel rich, and then combine with the extra air intake to provide more thrust from the flammable exhaust [23].

9. CLASS I CONFIGURATION MATRIX

The initial overall concept configurations can be shown in section 7.1. From these configurations, resulted in the concept of creating a family of Hyperhawks to incorporate a range of mission profiles which are discussed later.

Satellite

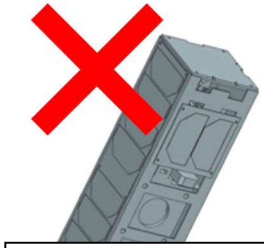

Swarm satellite

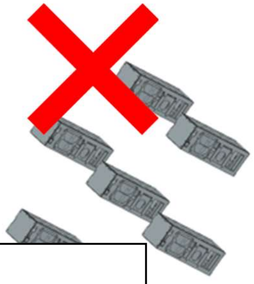

- + Small & inexpensive
- + Large aperture & redundancy
- - Predictable trajectory
- - Non reusable

Beechcraft AQM-37 Jayhawk

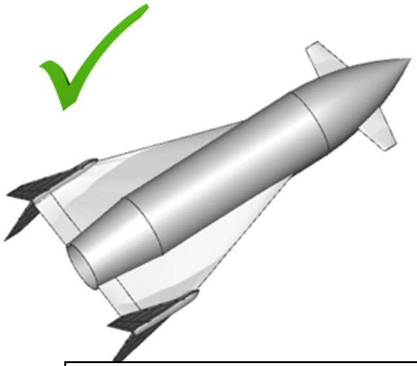

CIM-10 Bomarc

SM-64 Navajo

+ Ballistic mission profiles	- Requires heat shielding at tip
+ Redundant control surfaces	- Not designed for reusability

X-34 space plane

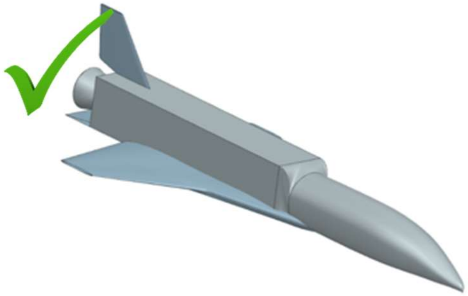

SR-72 with lower engines

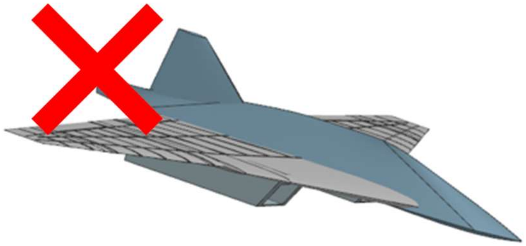

U-2

+ Versatile mission options	- Requires extended runway
+ Interchangeable payload capabilities	- Increased mass

+ Flight heritage	- Large increase in mass
+ Safe design for the Spec	- High fuel usage

9.1. DESIGN LAYOUT OF THE HYPERHAWK FAMILY

To incorporate both an exo-atmospheric mission and an endo-atmospheric mission a unique platform that these authors have named the “Hyperhawk” was designed based on the desirable design qualities listed in the previous chapter. The Hyperhawk has two main variants. Both versions of the Hyperhawk share a 90% common parts count. The endo-atmospheric variant can be shown in Figure 9.1.1. The endo-atmospheric Hyperhawk is a three stage missile, with a solid rocket booster, a liquid rocket core stage with a wing, and a final reusable third stage called the “Baby Jay”. During an exo-atmospheric mission the final reusable stage (the Baby Jay) would be placed on a traditional launch vehicle provided by a reliable launch provider and deployed in a way similar to Boeing’s X-37B described in the historical review. The performance, mission profiles, and subsystems will be described in depth in later chapters.

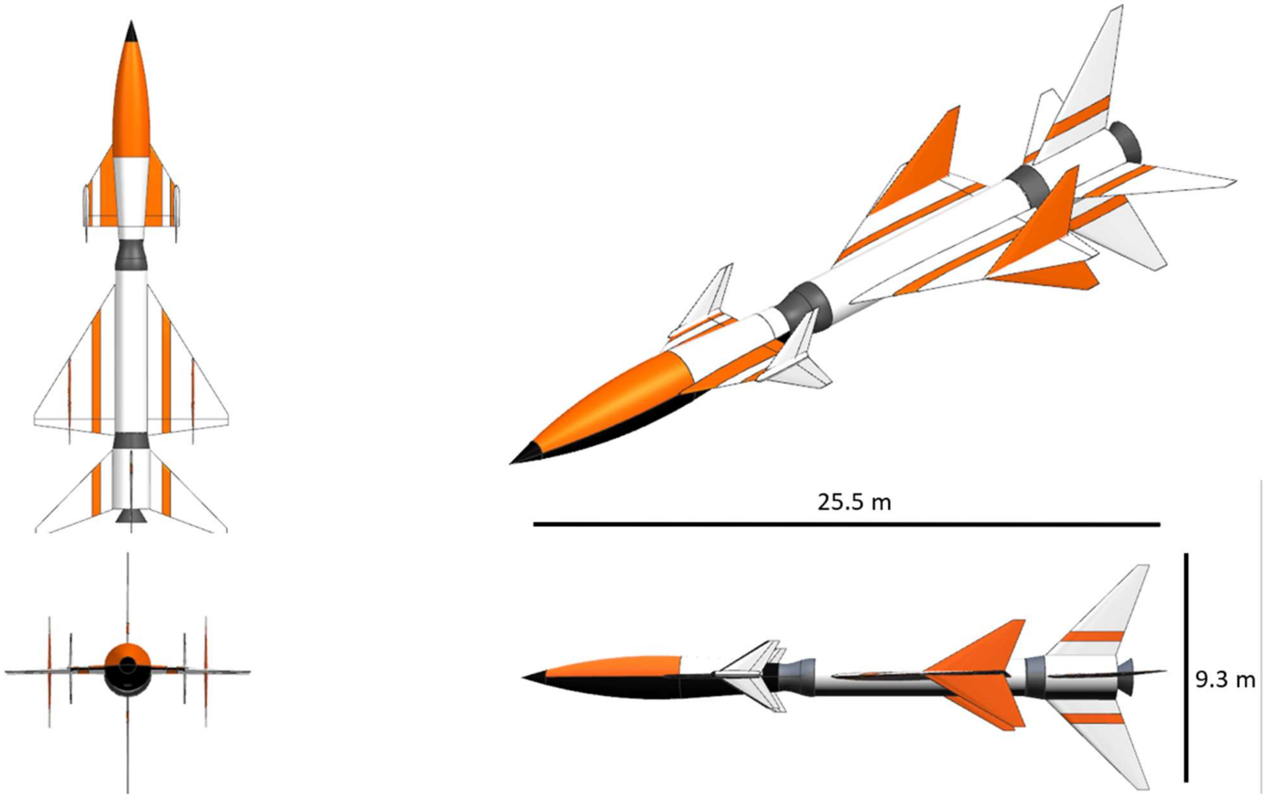

Figure 9.1.1: 3-View of the entire Hyperhawk (SRB, liquid rocket core, and Baby Jay)

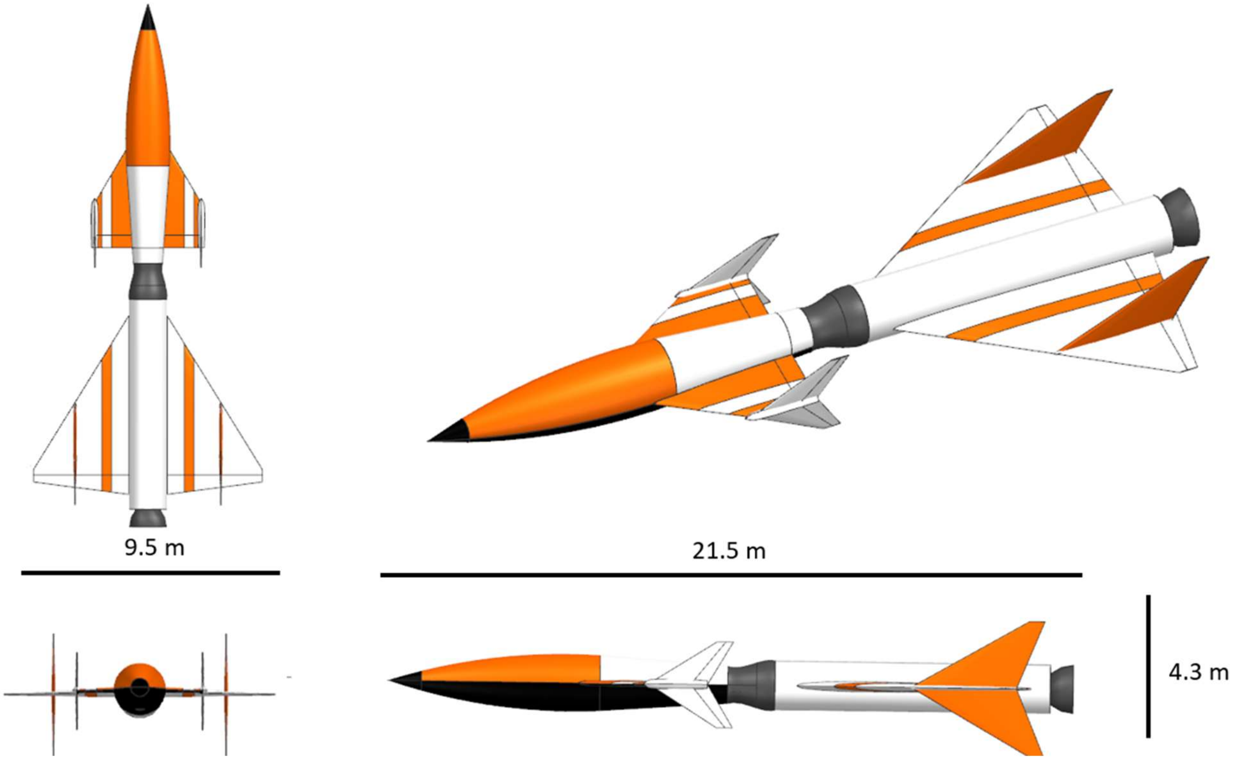

Figure 9.1.2: 3-View of Hyperhawk Baby Jay and core stages (after SRB separation)

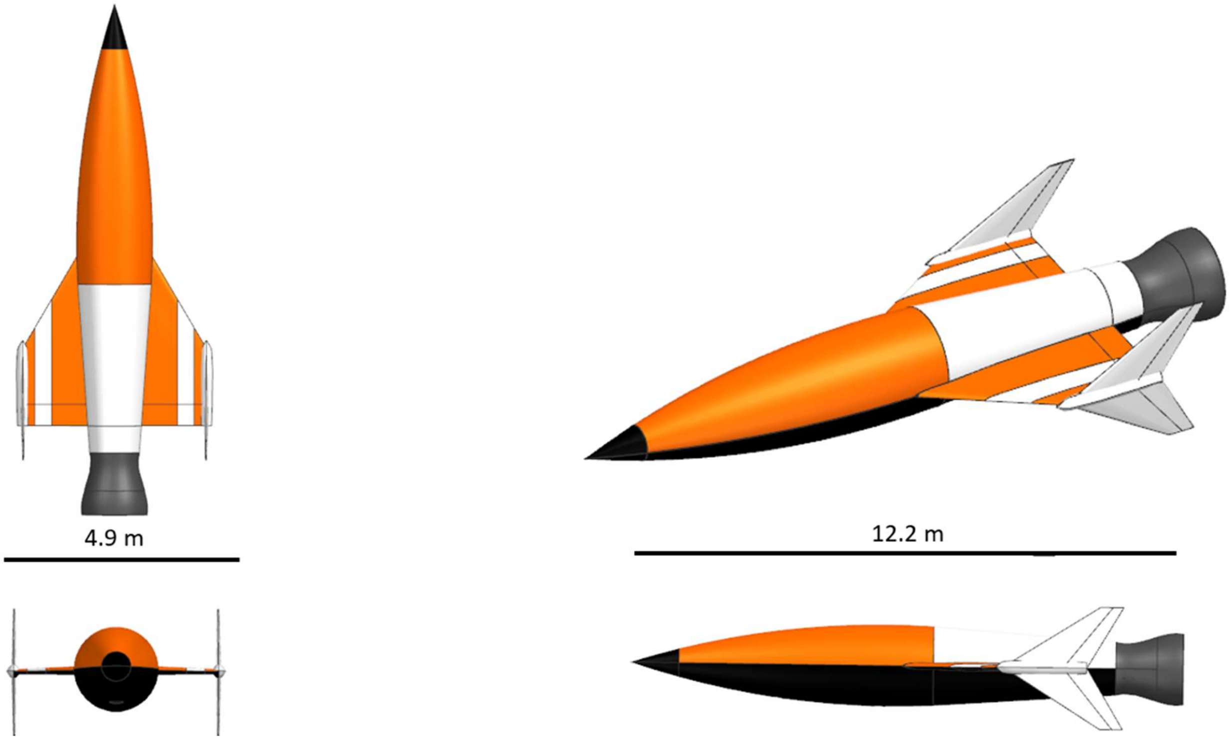

Figure 9.1.3: 3-View of Baby Jay

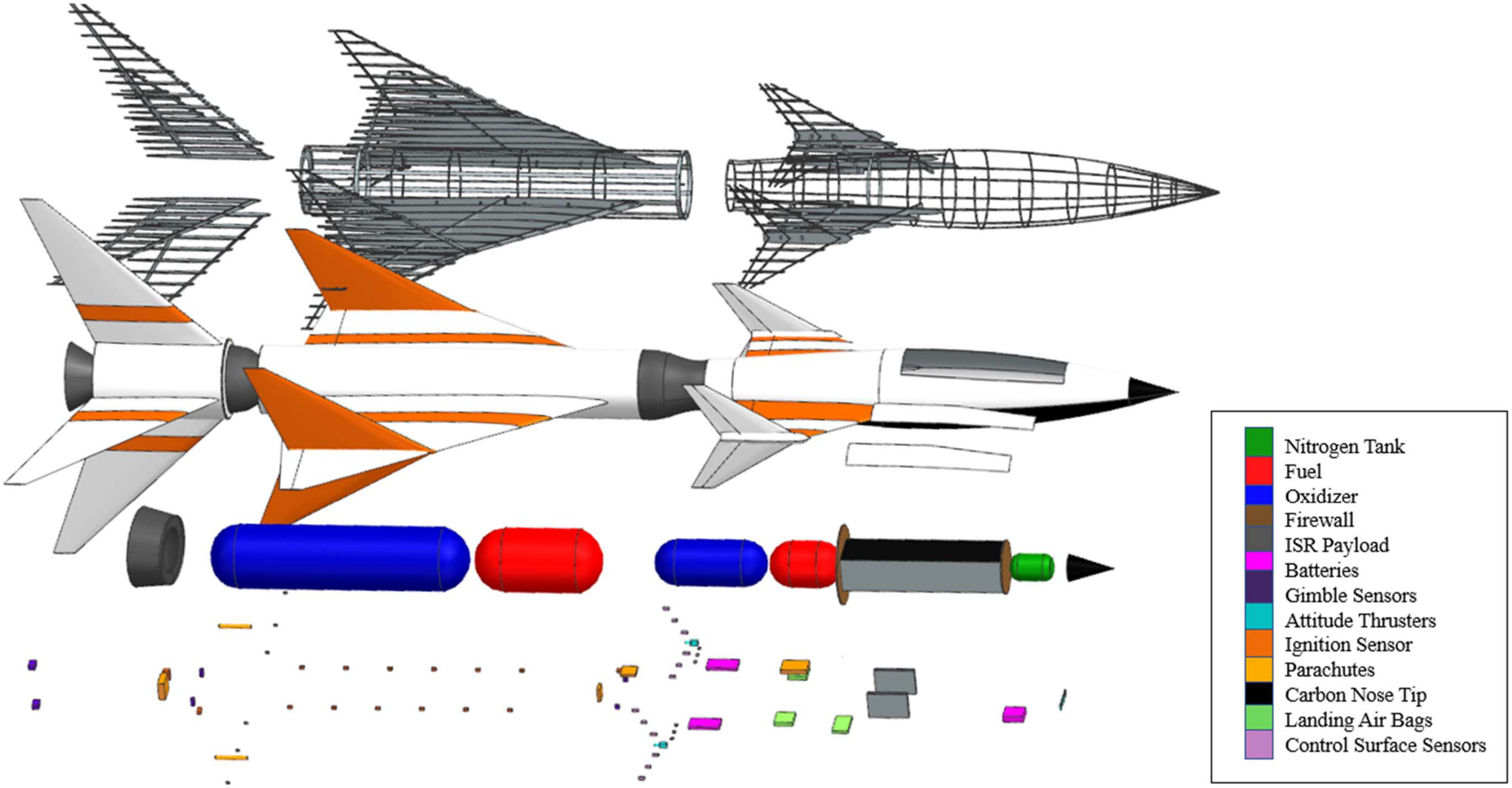

Figure 9.1.4: Exploded view of entire Hyperhawk

10. SOLID ROCKET BOOSTER DESIGN

The costliest portion of a rocket's flight is always launch as the vehicle starts with no velocity and at maximum weight. Understanding this, a reliable yet inexpensive solid rocket booster was chosen as the first stage of the Hyperhawk.

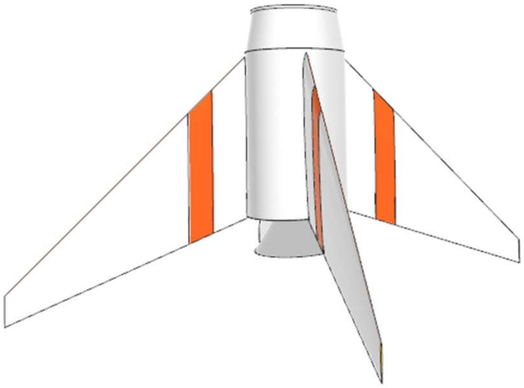

Figure 10.1: Solid rocket booster

The objective for the solid rocket booster (SRB) is to propel the vehicle to a velocity of Mach 1.5 at or near an altitude of 15,000 feet. The SRB is composed of 68% of ammonium perchlorate, 19% of aluminum, and 13% hydroxyl-terminated polybutadiene. This is the same composition as the SRBs of the Atlas V rocket chosen for its reliability and reduction of cost when using flight proven and currently manufactured hardware. The SRB of the Hyperhawk has a diameter of 72 inches with a length of 88.33 inches. The SRB is designed to have chamber pressure of 1000 psi and temperature of 6067.8 R. This SRB will be able to produce 300,000 lbf of thrust with a burn time of 26.5 seconds. The grain configuration will be an internal burning tube with additional conocyl to increase the burning surface. The grain will have an outer diameter 70.23 inches and inner diameter of 27.83 inches. The case of the SRB will be Graphite IM with a thickness of 0.284 inches, and to protect the case from the heat, 0.1 insulation will be used, this is similar to the Atlas V SRB booster. This results in an SRB that has 30,485 pounds of propellant, a case mass of 310.8 lbs. The nozzle designed for this SRB has a throat diameter of 14.57 inches and an exit diameter of 93.13 inches. The flight profile requires the SRB to pitch the vehicle down range to achieve the low angle of attack when burnout occurs. The required pitch over maneuver was modeled to confirm that the SRB was able to achieve the low angle of attach, Mach 1.5, and an altitude of 15,000 ft. This can be seen in Figure 10.2; the downrange distance is 13,000 ft and an altitude of 15,000 ft, the SRB was capable of all requirements.

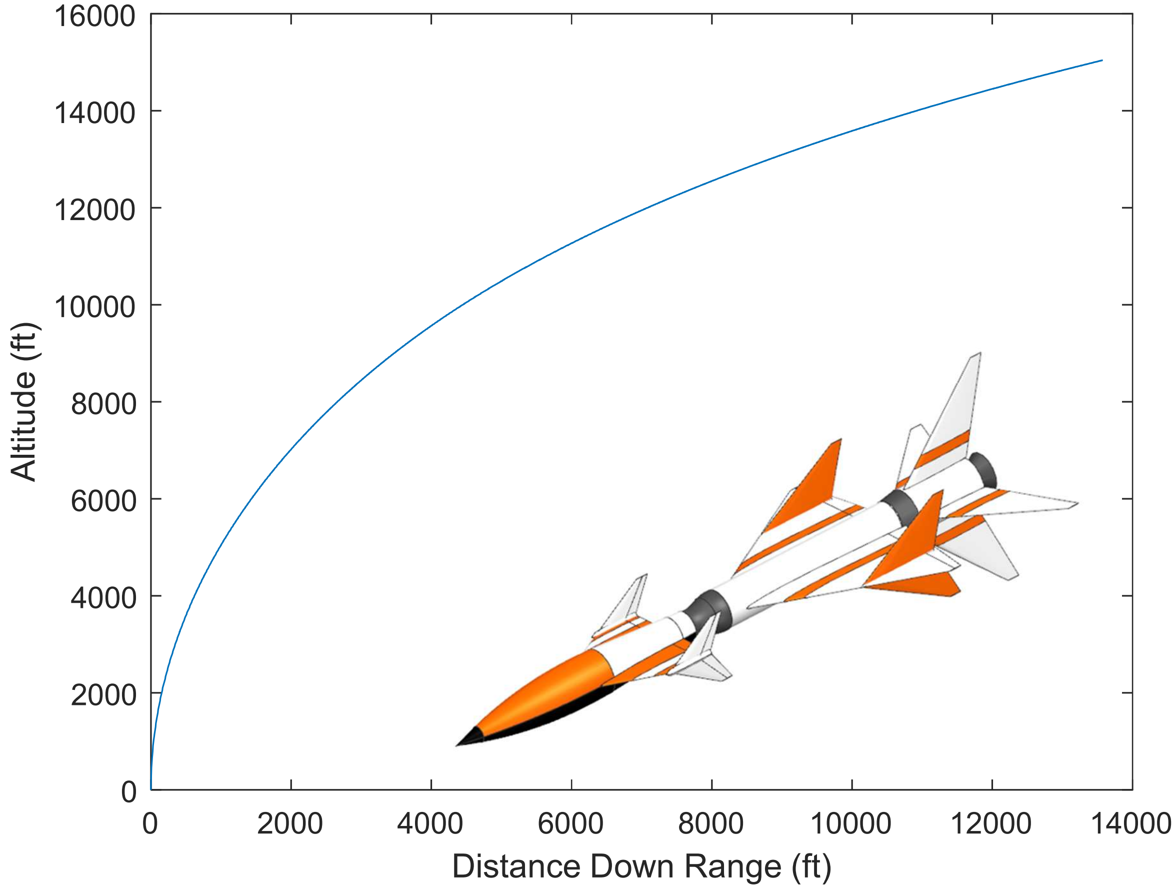

Figure 10.2: Solid rocket booster trajectory

11. ROCKET LAUNCH BALLISTIC CODE

To properly analyze the performance of the aircraft after the solid rocket booster first stage at many configurations, altitudes, and speeds, it was necessary to create a rocket launch ballistic code program to calculate various characteristics at finite time steps to analyze the performance. A pseudo-code representation of the performance code can be seen on the next page. The exact performance and mission profile that results from this code can be seen in the next chapters.

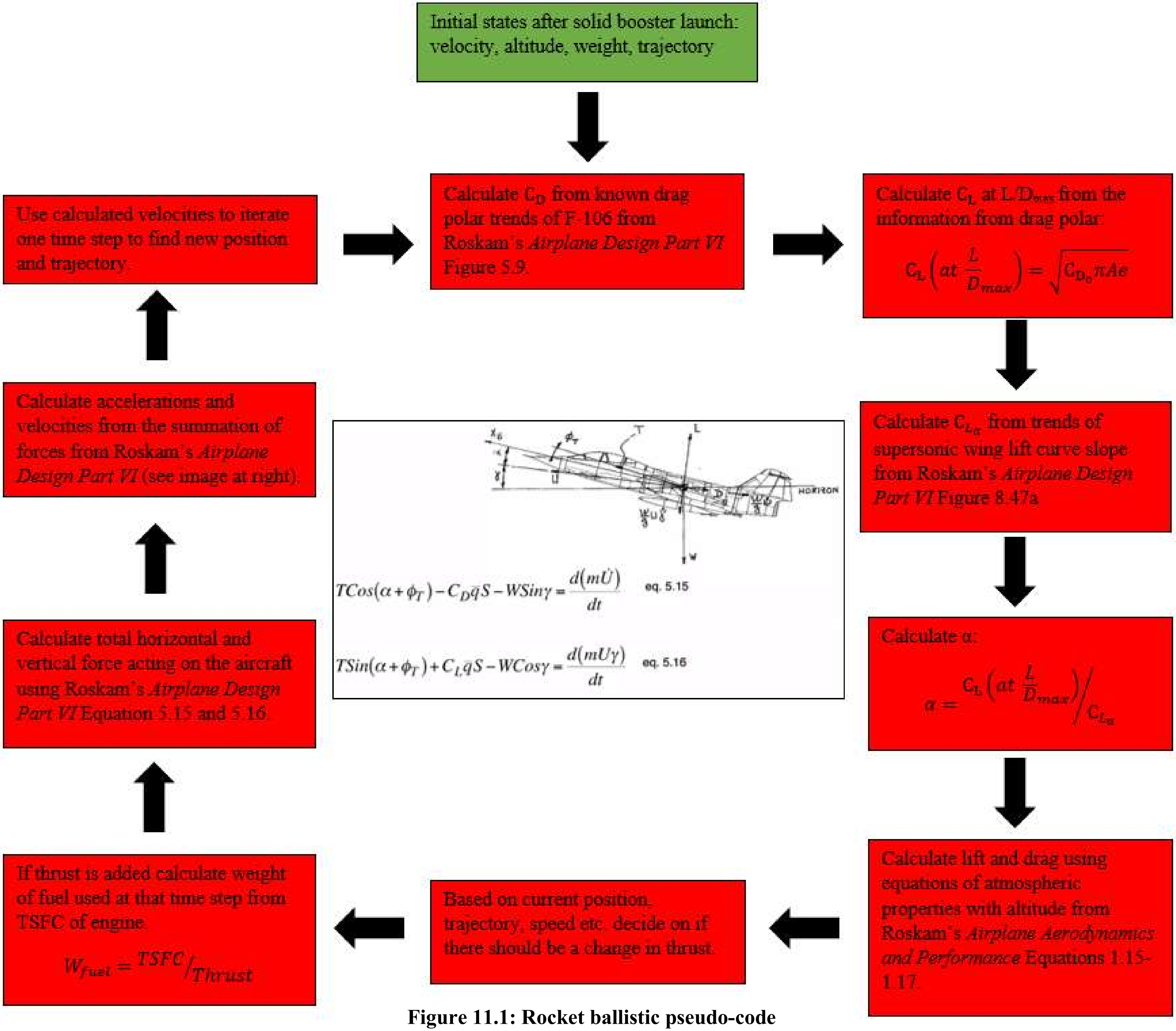

Initial states after solid booster launch: velocity, altitude, weight, trajectory

Calculate C_D from known drag polar trends of F-106 from Roskam's *Airplane Design Part VI* Figure 5.9.

Calculate C_L at L/D_{max} from the information from drag polar:

$$C_L\left(at\ \frac{L}{D_{max}}\right) = \sqrt{C_{D_0}\pi Ae}$$

Calculate C_{L_α} from trends of supersonic wing lift curve slope from Roskam's *Airplane Design Part VI* Figure 8.47a

Calculate α:

$$\alpha = {C_L\left(at\ \frac{L}{D_{max}}\right)}\Big/{C_{L_\alpha}}$$

Calculate lift and drag using equations of atmospheric properties with altitude from Roskam's *Airplane Aerodynamics and Performance* Equations 1.15-1.17.

Based on current position, trajectory, speed etc. decide on if there should be a change in thrust.

If thrust is added calculate weight of fuel used at that time step from TSFC of engine.

$$W_{fuel} = {TSFC}\Big/{Thrust}$$

Calculate total horizontal and vertical force acting on the aircraft using Roskam's *Airplane Design Part VI* Equation 5.15 and 5.16.

$$TCos(\alpha+\phi_T)-C_D\bar{q}S-WSin\gamma=\frac{d(mU)}{dt} \quad \text{eq. 5.15}$$

$$TSin(\alpha+\phi_T)+C_L\bar{q}S-WCos\gamma=\frac{d(mU\gamma)}{dt} \quad \text{eq. 5.16}$$

Calculate accelerations and velocities from the summation of forces from Roskam's *Airplane Design Part VI* (see image at right).

Use calculated velocities to iterate one time step to find new position and trajectory.

Figure 11.1: Rocket ballistic pseudo-code

12. LIQUID ROCKET CORE STAGE

Of particular importance for analysis was the second liquid rocket core stage. This stage brings the rocket up to its final cruise altitude and speed in two distinct phases. During the first phase the rocket separates from the first stage solid rocket booster and has both a wing and "canard" (which is in fact the wing of the final stage "Baby Jay"). This configuration is similar to that of modern jet fighters like the Eurofighter Typhoon. This phase begins at the end of the solid rocket booster burn at 15,000 ft and Mach 1.5 and climbs at a maximum lift to drag ratio while maintaining Mach 1.5 until the density of the atmosphere is reduced to the point where the wing no longer produces lift at approximately 100,000 ft. At this point the liquid core stage enters its second phase of flight.

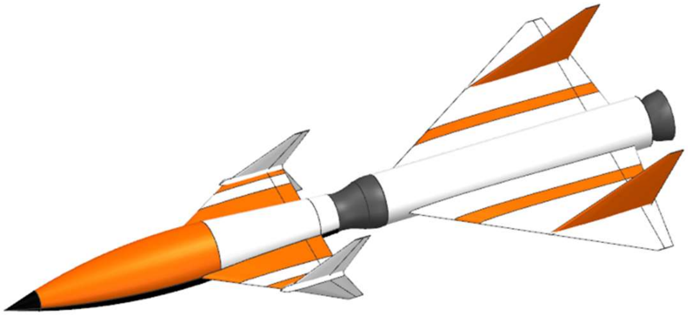

Figure 12.1: Cores stage 1 configuration

The second phase begins at Mach 1.5 and 100,000 ft. Because the wing is no longer useful the wing is separated as it serves no further purpose. With the wing separated, the orbital maneuvering system of the Baby Jay and the gimbal of the core stage engine pitches the aircraft up to maintain a flight path angle of 60°. In this configuration the aircraft resembles a traditional rocket launch vehicle in an optimal climb to the edge of space at the Karman Line (100 km altitude) exceeding the altitude requirement in the RFP. It also accelerates the Baby Jay to Mach 10 also exceeding the cruising speed requirement in the RFP. The Karman Line was specifically chosen as the operational to allow mission planners to decide whether to fly in what international law considers in

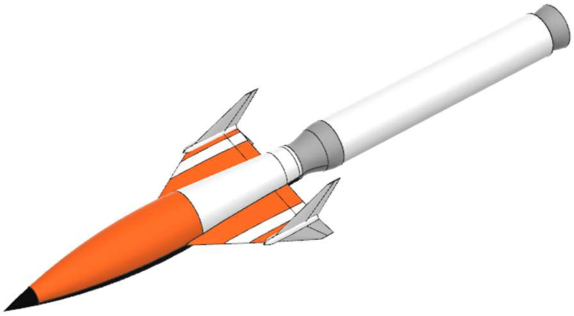

Figure 12.2: Cores stage 2 configuration

atmosphere (below the Karman Line) or in space (above the Karman Line) to effectively decide what laws or regulations the user wants to follow. The analysis of this space law is described in Chapter 3 above.

The ballistic code described in the previous chapter was used to analyze various engines, and wings. After much consideration and analysis, a scaled version of the 60° delta wing of the F-106 was used for the wing on the core stage. This wing was chosen due to its flight heritage and proven reliability, its simplicity for manufacturing (and therefore a reduction in cost), and its supersonic aerodynamic characteristics being favorable and readily available in Dr. Jan Roskam’s *Airplane Design Part VI: Preliminary Calculation of Aerodynamic, Thrust and Power Characteristics* [24]. The details of these characteristics are described in a later chapter.

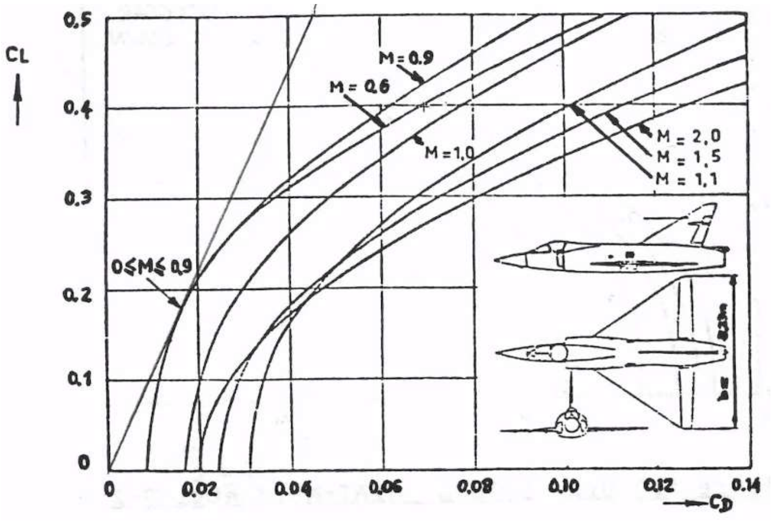

Figure 12.3: Convair F-106 drag polar [24]

Similarly, after analyzing various engines the Newton 3 engine manufactured by Virgin Orbit was chosen for the core stage. Most liquid rocket engines are either two large, adding unnecessary weight, complexity, and fuel consumption, or too small meant for satellites. Fortunately, Virgin Orbit offers a unique launch vehicle called the LauncherOne. This is a small rocket meant to launch from the underbelly of a modified Boeing 747 [25]. Because of this, the launch vehicle is similar in size and weight as the Hyperhawk and is meant to perform at the same altitudes as the Hyperhawk having already been carried to altitude and speed by the 747 aircraft. The Newton 3 characteristics can be seen in the Table below.

Table 12-1: Newton 3 engine characteristics [25]

Characteristic	Value
Specific impulse	~300 seconds
Fuel	RP-1
Oxidizer	Liquid Oxygen
Thrust	75,000 lbf

13. BABY JAY

The Baby Jay is similar to the core stage in that it also uses a scaled F-106 60° delta wing for the same reasons stated above. In addition, it also uses an engine used for the LauncherOne, the Newton 4 used on the LauncherOne's second stage. At the Karmin line there is little friction and therefore this engine is capable of maintaining the Mach 10 cruise at the Karman Line for the 3,000 nmi required in the RFP according to the code described previously. The characteristics of this engine can be seen in the Table below.

Table 13-1: Newton 4 engine characteristics [25]

Characteristic	Value
Specific impulse	~300 seconds
Fuel	RP-1
Oxidizer	Liquid Oxygen
Thrust	6,000 lbf

13.1. THERMAL PROTECTION SYSTEM

The Baby Jay will have to withstand two different thermal loads. In the endo-atmospheric mission it will have to survive Mach 10 flight at 328,000 ft. In addition, for the exo-atmospheric mission it will have to withstand the heat of reentry. Secondary considerations for the heat shield include the cost of the heat shield and the turn-around time of the system as the RFP requires a turnaround 24 hours or less. Based on these three different heat shields where considered: high-strength carbon-carbon composites, space shuttle silica tiles, an ablative fiberglass honeycomb filled with epoxy resin, and the new Phenolic Impregnated Carbon Ablator (PICA-X) material used by SpaceX on its Crew Dragon.

Of the two thermal loads reentry is by far the greater of the two. Reentry heat shielding is primarily determined on the speed and orbit the spacecraft is coming from. This is why the Apollo missions that came from lunar orbit at very high speeds had to have much greater shielding than the Shuttle missions that never left Earth's orbit. The possible exo-atmospheric missions of the Baby Jay will never be greater than the flight regime of the Space Shuttle and the Baby Jay is relatively similar in shape and profile to the Shuttle. Therefore, the heat shielding requirements of the Baby Jay can be assumed to be similar to that of the Space Shuttle or SpaceX's Crew Dragon which can reach as high as 3,000 degrees Fahrenheit.

Carbon-carbon composites have only successfully been deployed on the Parker Solar Probe successfully so have not shown high degrees of reliability in many successful missions like silica tiles of the Space Shuttle or the honeycomb filled epoxy resin of the Apollo thermal protection system.

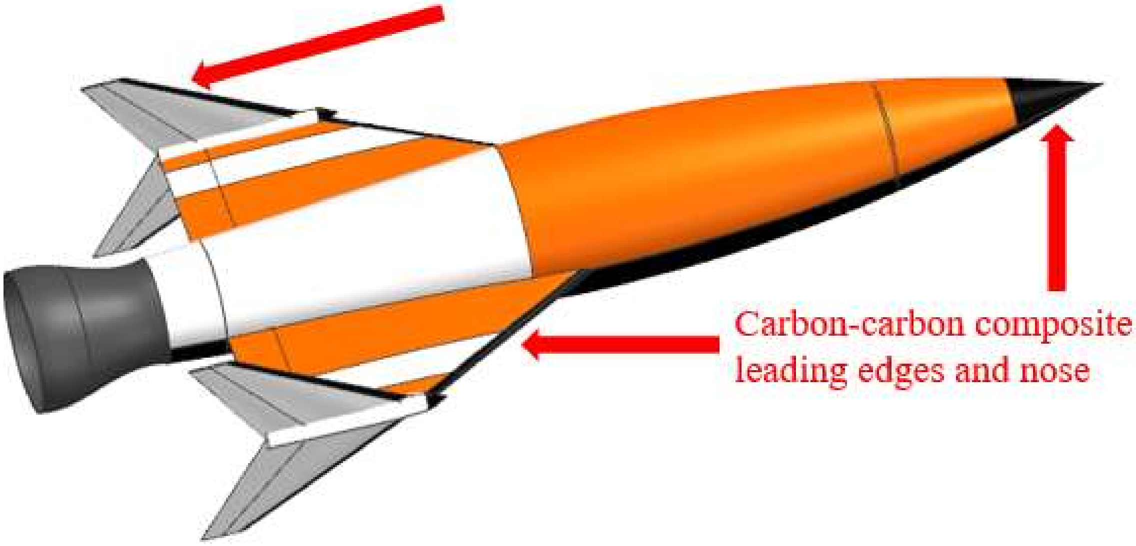

Figure 13.1.1: Baby Jay Thermal Protection

With reliability being a serious concern carbon-carbon epoxy was removed from the list of possible thermal protection systems for reentry. However, carbon-carbon composites are useful for the leading edge of the wing and the nose of the aircraft during hypersonic flight where the leading edge will heat to extreme temperatures during the Mach 10 cruise stage of endo-atmospheric flight. For this reason, carbon-carbon composites were selected for the leading edge of our Baby Jay to protect the leading edges and nose of the aircraft during its Mach 10 cruise flight.

By far the highest reliability in thermal protection has been on the space shuttle with 133 successful missions. However, the space shuttle had to be made up of 24,000 silica tiles each of which had to be individually inspected for repair and replacement after every launch with the fastest turnaround time ever being 54 days although this was not due to the shielding alone. Although this system may offer high reliability the inspection time, complex manufacturing process, and each tile having to be uniquely shaped for its exact position on the spacecraft means that this system would most likely not meet the turnaround requirement of at least 24 hours.

Another option is the Apollo’s thermal protection system made from ablative fiberglass honeycomb filled with epoxy resin. Because this shielding is ablative it is meant to be replaced after every use. As long as the spacecraft was built with this in mind there is no reason that the used thermal protection system couldn’t be removed and a new one added in the turnaround window of 24 hours. However, this thermal protection system had a much smaller mission history with only 17 missions. In addition, although it’s ablative properties may help with the turnaround time the cost would be significant to replace such an expensive part every launch.

The final thermal protection system is the PICA-X material co-developed by NASA and SpaceX for its Crew Dragon capsule. This unique material is near the density of solid cork (0.24 g/cm^3) and only needs to be a few centimeters thick (on average around 6 cm). In addition, the material is so heat resistant it could potentially be used to survive lunar or even Mars re-entry far exceeding that of the Apollo or Space Shuttle’s thermal protection system. After reentry less than a centimeter of the heat shield pyrolyzes and must be removed revealing untouched PICA-X material underneath. With the shield being over 3 inches thick in places this removal of charred material has little to no effect on the overall protection system allowing for the reuse of the system for multiple missions [26]. Furthermore, the Dragon capsule has successfully been launched over 20 times as of the time or writing and has been reused successfully as many as nine times with more predicted.

Overall, the PICA-X material used by Space-X offers the best mixture of reliability, reusability, cost, and weight of the thermal protection systems considered. Therefore, it was decided to use this thermal protection system on the Baby Jay in order to meet a low overall cost and quick turnaround time. These thermal protection systems should keep both the ISR payload and RF antennas cool for the mission thus meeting the RFP requirement.

Figure 13.1.2: PICA-X heat shield on Baby Jay Underbelly

The final thermal protection system that must be discussed is the requirement of two downward-looking windows, each with a diameter of 12 inches, transparent for EO/IR imagery, and contiguous to the payload space. For this purpose, two different materials where considered. The first was the fused silica glass used on the Space Shuttle that could withstand loads of 900°C for extended periods and even up to 1200°C for short periods [27]. As discussed above the Shuttle Program was very successful and shows the reliability of the material used. However, a better material can be found in the Russian Soyuz spacecraft that uses synthetic single crystal ruby grown to the same shape and approximate size as required for the request for proposal. This single crystal ruby that has a melting point of 2209°C [28]. It is for this reason that single crystal ruby was used to meet the request for proposal's requirement for EO/IR imagery at the bottom of the Baby Jay under protective heat shield doors similar to the way the Space Shuttle had doors for its landing gear.

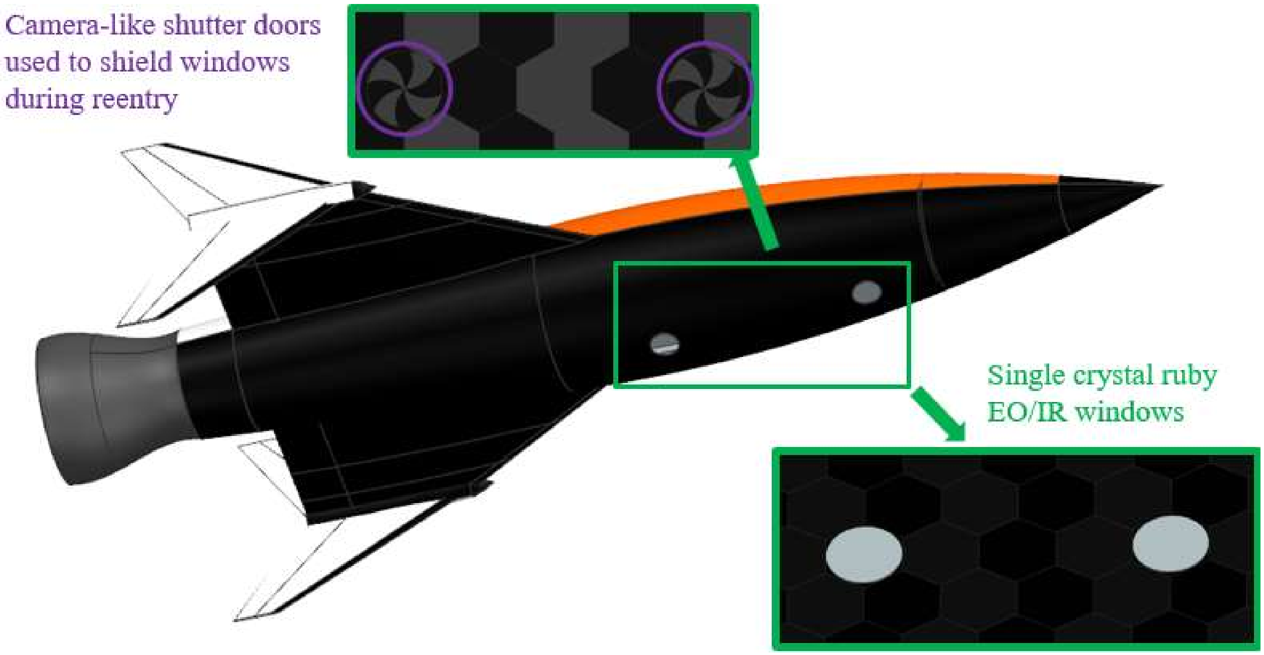

Figure 13.1.3: Single-crystal ruby EO/IR windows with heat shield doors

13.2. RECOVERY

The two options considered for the recovery of the Baby Jay reusable section of the Hyperhawk were a traditional runway landing and a parachute recovery with air bags. Understanding that one of the primary mission objectives for this design was to be versatile in the areas it could operate in both for landing and takeoff the decision was made to use a parachute recovery on air bags. Modern parachutes have effective glide ratios of 3:1 and can be GPS directed to land within a 100 ft square if needed. In addition, the air bag landing allows for the recovery of the Baby Jay on both land and sea. In the case of a water landing or an abort over water the Baby Jay could safely abort into the ocean and even in rough seas where the entire system is flipped it would still be recoverable.

This recovery method would start at the cruise altitude and speed of 100 km and Mach 10. After the Baby Jay had successfully completed its ISR mission it would use its orbital maneuvering system (OMS) to pitch up and maintain a high angle of attack to quickly bleed of speed until the Baby Jay was flying at Mach

< 1. After this was done the OMS would then pitch the Baby Jay back down and a drogue parachute would deploy to further decrease the speed to Mach < 0.3 as well as to help avoid a flat spin. After the speed was below Mach 0.3 the main parachute would deploy and the Baby Jay would be able to successfully glide with a L/D of 3 to a designated target via GPS at which point the air bags would deploy to cushion the Baby Jay for touchdown and recovery. This meets the requirement of landing on traditional runways in the RFP. In addition this allows a less than 24 hour turnaround time for the Baby Jay as only the parachute would be repacked and then the system could be launched on a new solid rocket booster and liquid core stage.

Figure 13.2.1: Baby Jay landing procedure

14. ENDO-ATMOSPHERIC MISSION PROFILE

Once the performance of the Hyperhawk is analyzed using the rocket ballistic code in the section above, the mission profiles can be visualized below:

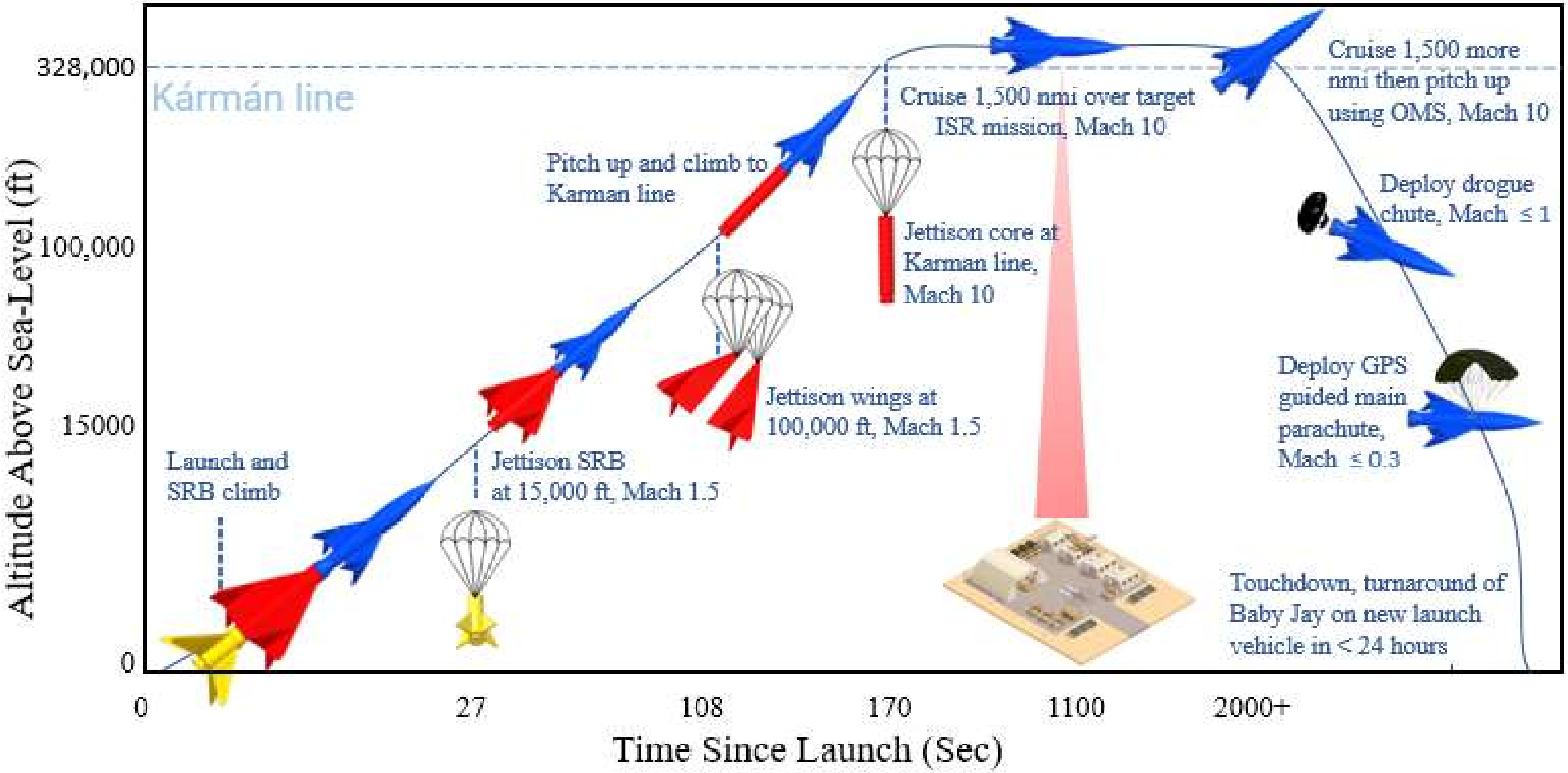

Figure 14.1: Endo-atmospheric mission profile

15. EXO-ATMOSPHERIC MISSION

Figure 15.1: Baby Jay deployment from Falcon 9 second stage

For missions that require prolong surveillance, an exo-atmosphere mission will be utilized. This will also provide the capability to gain intelligence over multiple passes. For this mission, the Baby Jay will be placed within the fairings of a SpaceX Falcon 9. This will only require the addition of an adaption ring for proper fitment. This will then roll out to a launch pad at either Cape Canaveral Space Force Station or Vandenburg Air Force Base. The launch complex will be decided on the required inclination of the orbit for the mission. If the mission requires observations above 57 degrees latitude, the Baby Jay will have to launch out of Vandenburg Air Force Base. This is due to regulations of launching a rocket over populated areas and this restricts Cape Canaveral to launching at a maximum inclination angle of 57 degrees. On the ascend portion of the mission there will be five major events that occur, this will be maximum dynamic pressure (Max-Q), main engine cutoff (MECO), second engine startup (SES), second engine cutoff (SECO), and payload deployment. Max-Q will occur roughly a minute and 15 seconds into the flight, MECO will occur about two minutes and 40 seconds into the flight. This is when the first stage of the Falcon 9 and the second stage separate and a delay five second occurs before SES. The second stage will insert the Baby Jay into an elliptical orbit that has an apogee of 250 miles and a perigee of 155 miles. The first orbit will be utilized to stabilize the vehicle and properly orientate the camera for the upcoming pass over the intended target. While this occurs, the spacecraft will release a solar array to power all the onboard electronics and payloads. Baby Jay will start using the communication system to connect to friendly ground stations to receive commands and

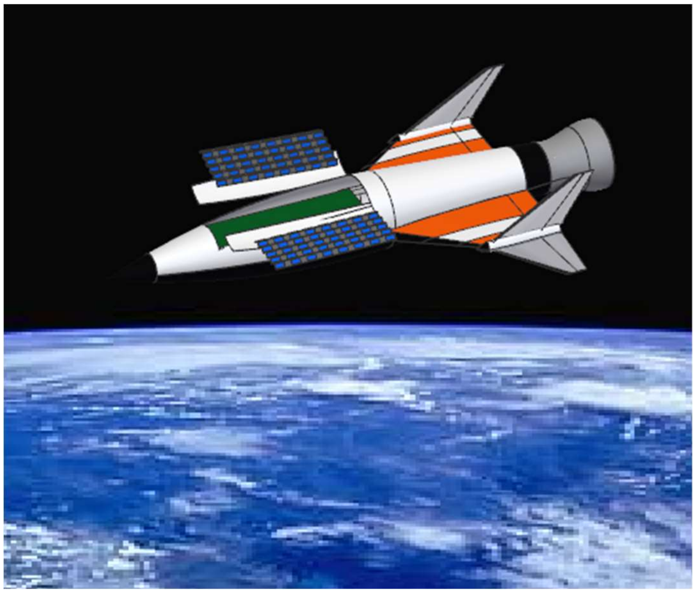

Figure 15.2: Baby Jay in orbit

provide vehicle life data. Once this initial startup phase is complete, Baby Jay will go into reconnaissance mode. This is when the ISR payload will be activated over the intendent target to record the necessary information. Then Baby Jay will relay the data through a secured connection to an overhead government satellite that can transmit it through the satellite network to be transferred to ground. This process will be repeated through the duration of the mission, the target will be able to be changed through the mission. Once the reconnaissance is complete, Baby Jay will complete a deorbit burn and reenter back into the atmosphere for a parachute landing as described in a previous chapter. This overall mission profile is similar to that of the X39-B/ Orbital Test Vehicle built by Boeing. The key difference is in the landing phase, as Baby Jay will land on airbags, the X39-B lands on a runway like a conventional aircraft

During the mission, if the target location is changed, the vehicle can utilize the elliptical orbit and the drag at perigee and the propulsion system to change inclination. This is a similar capability to that of the Orbital Test Vehicle. In addition, the orbit can be changed such that the Baby Jay would return safely to its launch site meeting the RFP requirement and allowing for a quick turnaround time of 24 hours as long as another launch vehicle was ready.

16. EXO-ATMOSPHERIC MISSION PROFILE

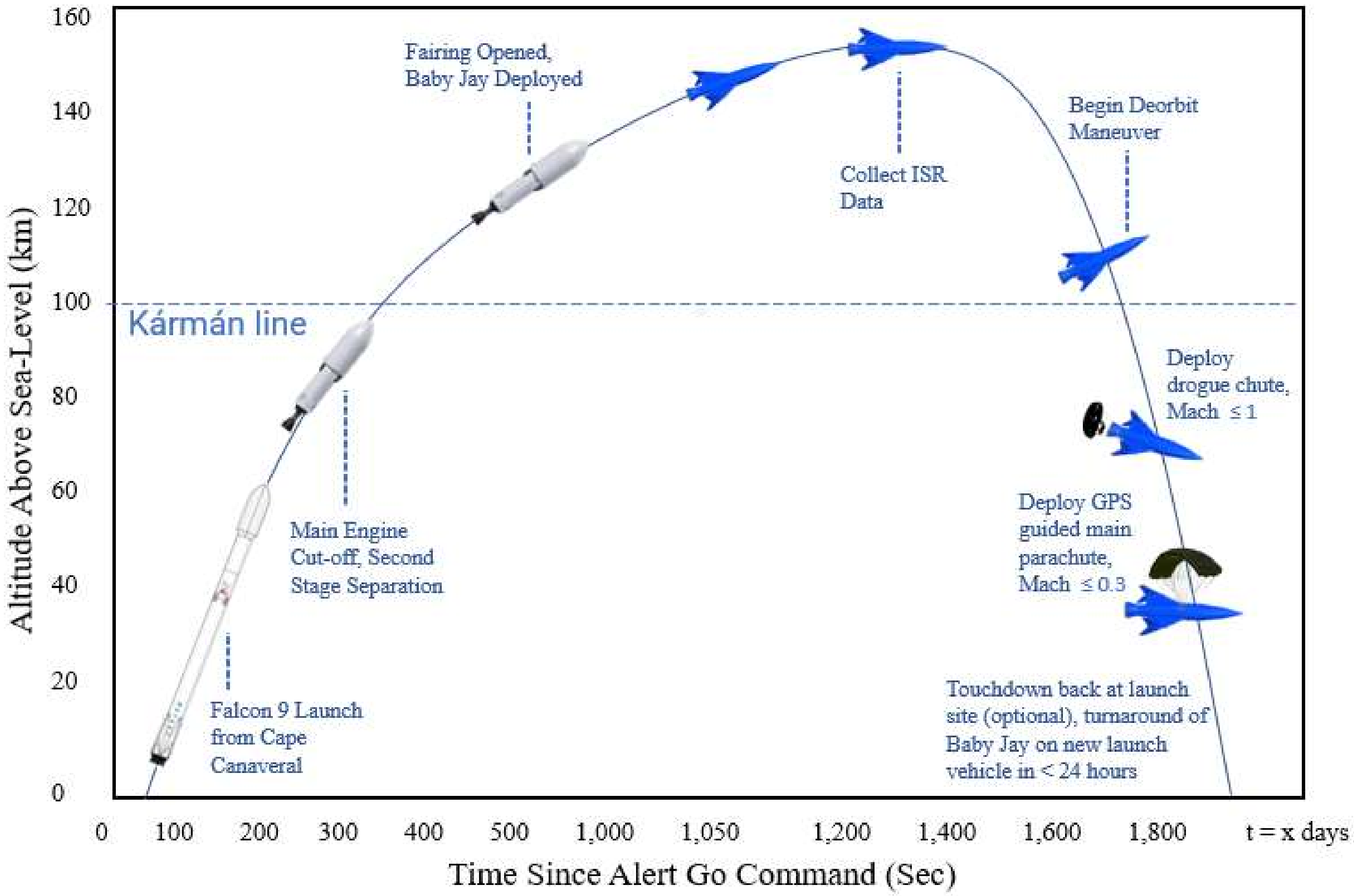

Figure 16.1: Exo-atmospheric mission profile

17. DRAG POLAR AND PERIMETER PLOT

From methods presented in Roskam's *Airplane Design Part I* [13] Section 3.4.1 as well as the F-106 drag polar data presented in Roskam's *Airplane Design Part VI* []. The drag polar of all three configurations: the entire Hyperhawk, the core stage, and the Baby Jay can be determined based of the wing area, and wetted area as all configurations use the F-106 wing and thus follow its trends extrapolated and reevaluated at larger or smaller wing areas (depending on the configuration) and at higher Mach numbers. These can be seen graphically below.

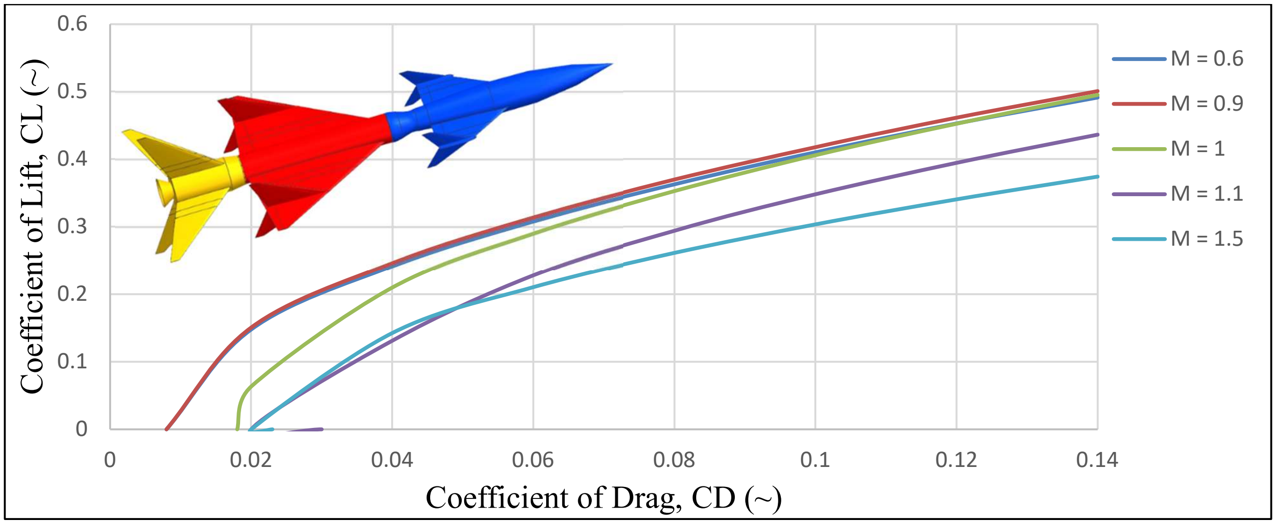

Figure 17.1: Hyperhawk Drag Polar

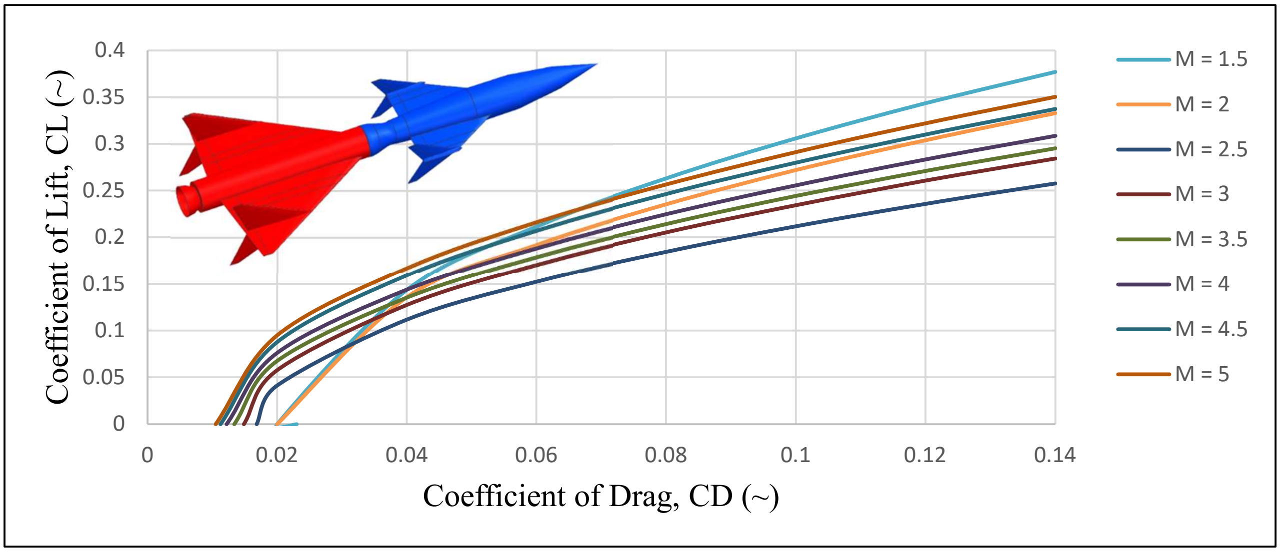

Figure 17.2: Baby Jay and Wing Drag Polar

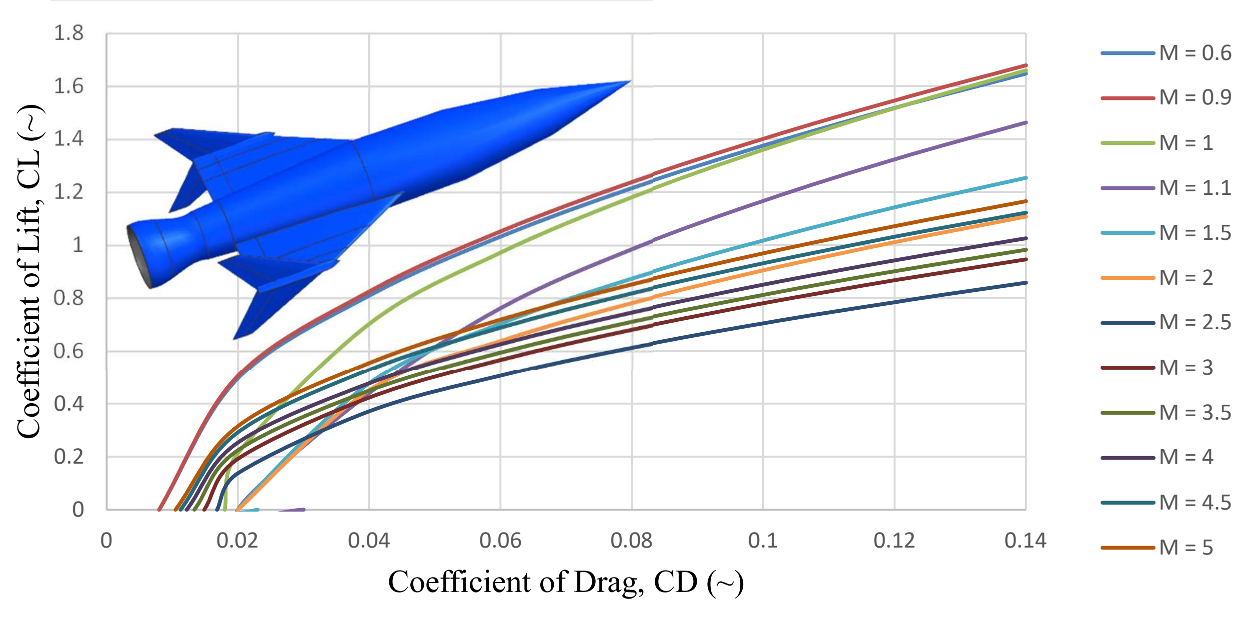

Figure 17.3: Baby Jay Drag Polar

In addition, a perimeter plot can be made of the Hyperhawk and the Baby Jay based on the CAD in the previous sections. This is seen in the Figures below.

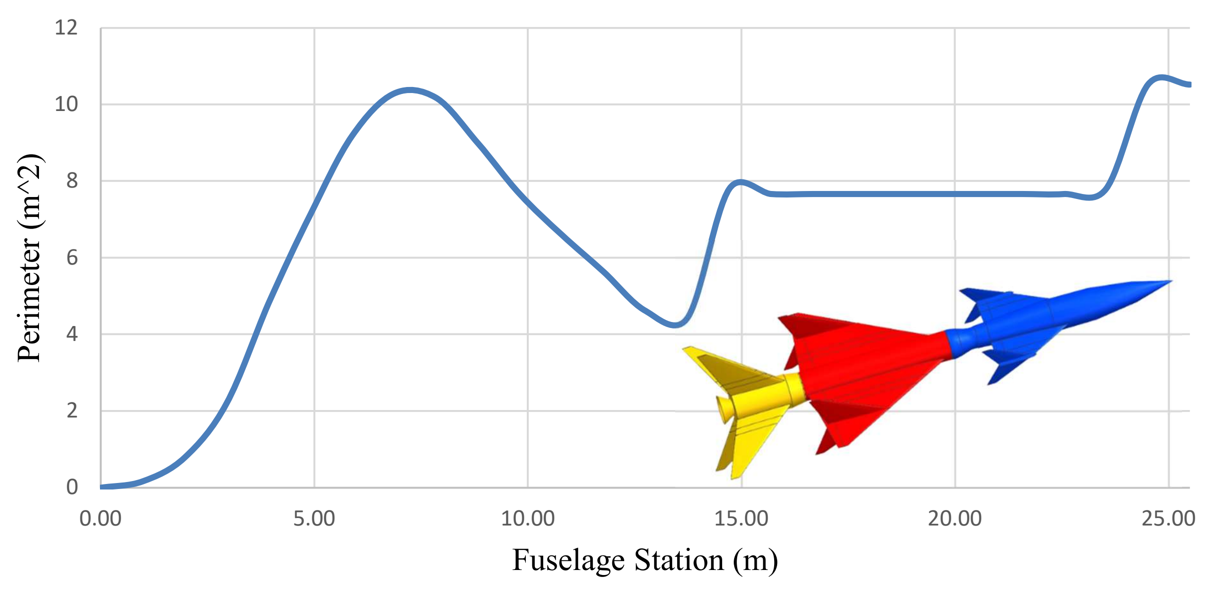

Figure 17.4: Hyperhawk perimeter plot

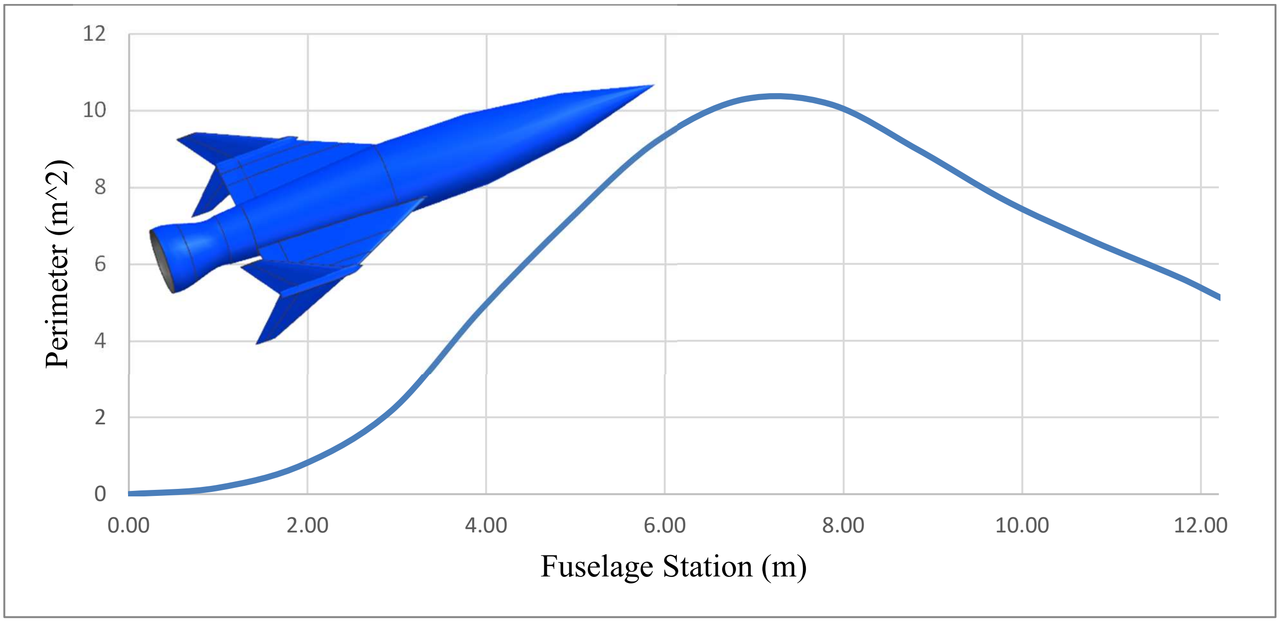

Figure 17.5: Baby Jay perimeter plot

18. ELECTRICAL AND MECHANICAL SUBSYSTEMS

Given the criticality of the Hyperhawk's mission, its systems are designed to provide high reliability and redundancy. Safety of flight is assured through the use of triple redundant power and flight control systems. In addition, the control surfaces of the Baby Jay are divided into three sections where any two can override an issue with the third in the unlikely event that a control surface actuater failed. This is illustrated in the electrical schematic shown in Figure 18.1. Also shown are the electrical power, staging, ignition, air data, communication and ISR data systems. These systems are described in more detail below.

Electrical power is provided by three independent Lithium-Ion batteries. Lithitum-Ion batteries are used due to their lightweight, relatively high energy density, and reusability. These batteries are positioned away from each other in the craft to ensure that even in the event of damage to one component the Hyperhawk will still have electrical power.

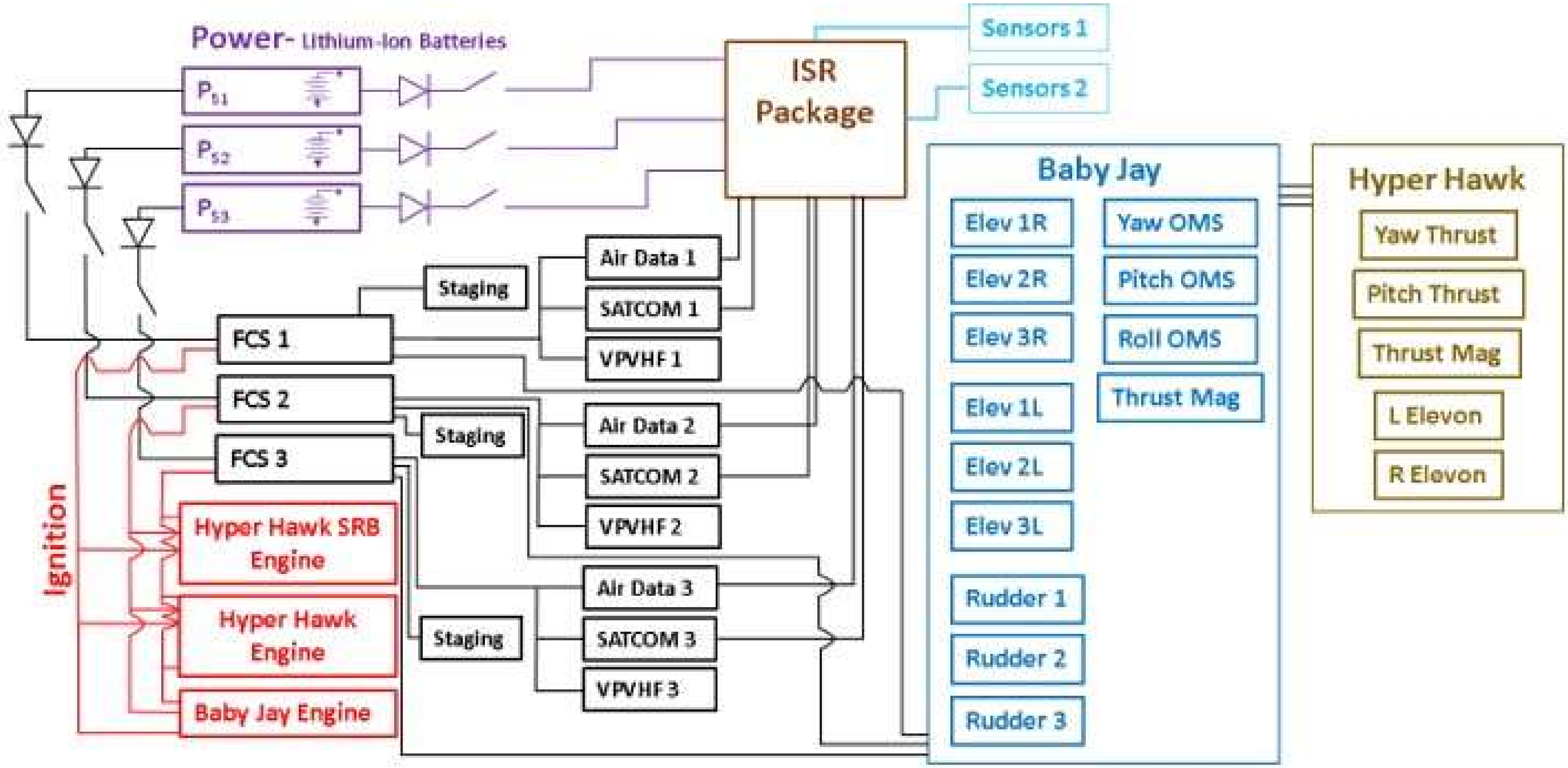

Figure 18.1: Wiring Diagram

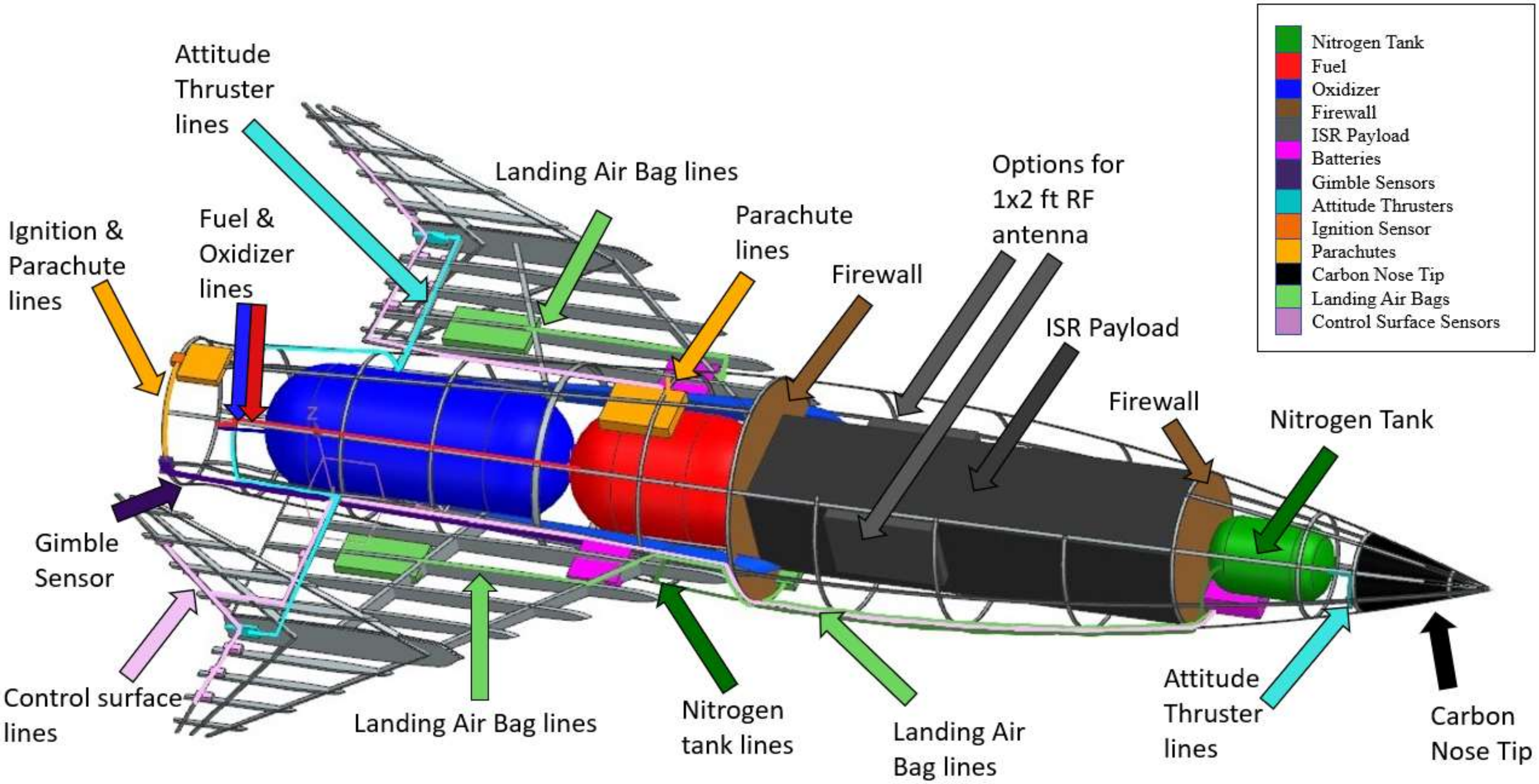

Figure 18.2: Baby Jay internal systems diagram

Since the Hyperhawk includes multiples stages, a reliable way to jettison each stage is required. Both the solid rocket and the wing sections use explosive bolts on joining ring frames to disconnect. To be sure that the expended stages are jettisoned, two charges are placed on each connecting bolt, and both are trigged when the staging command is given.

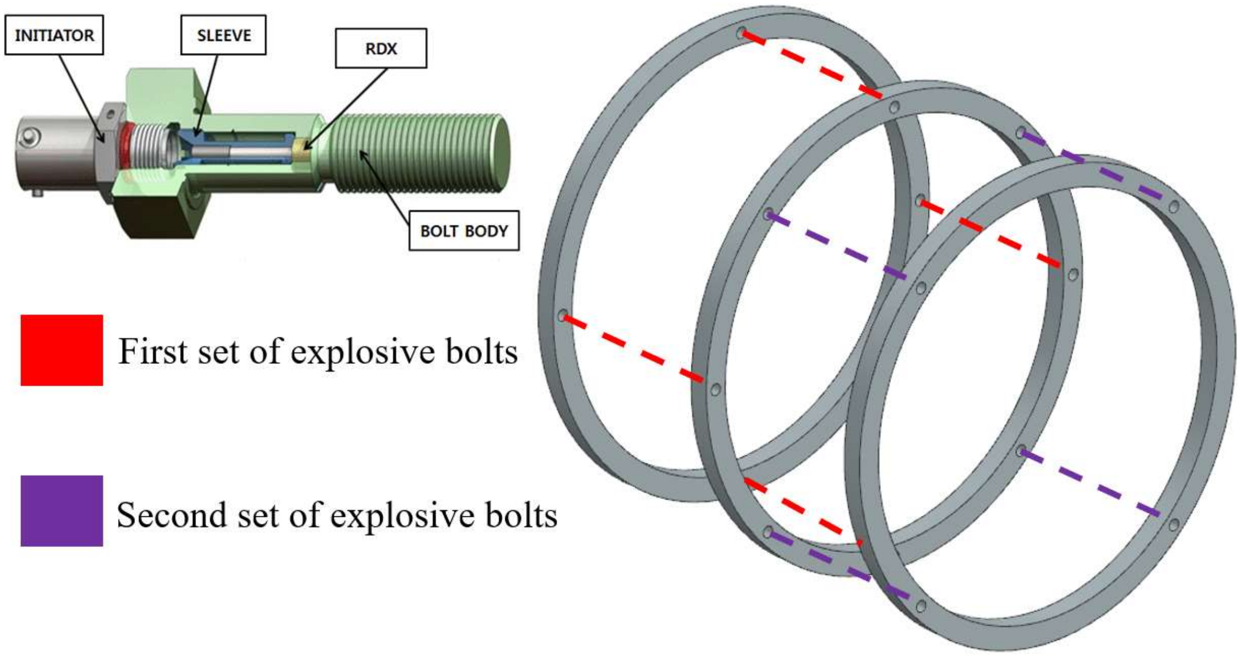

Figure 18.3: Redundant explosive bolt ring assembly

After the bolts are severed, pre-tensioned rods assure that the expended stages are pushed away from the craft. This method of separation is most prominatly used on SpaceX rockets. This system relies on compressed gas already required to pressurize fuel and oxider tanks to push a rod into the nozzle of the next stage engine thereby pushing the detached used stage away from the next stage allowing for the next stage to ignite safely.

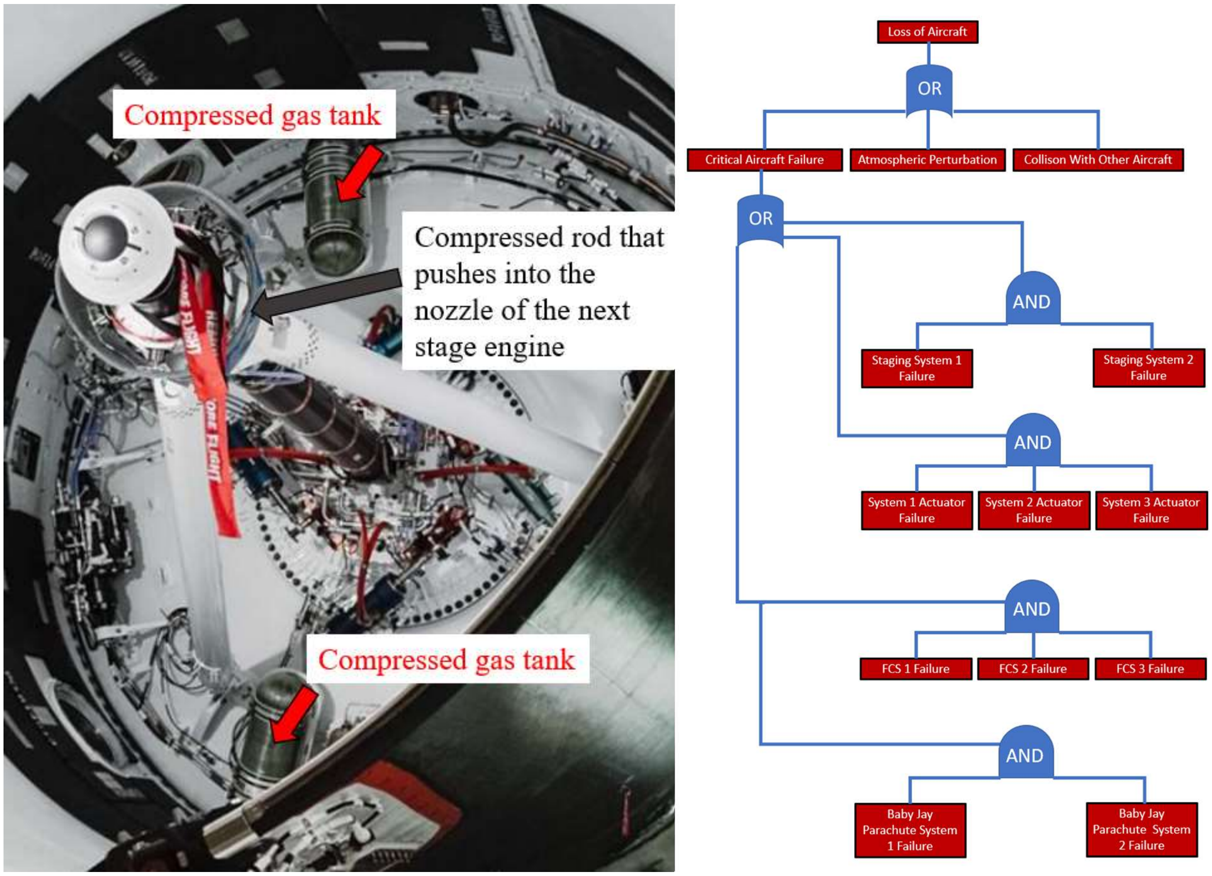

Figure 18.4: Separation mechanism on SpaceX Falcon 9 (left) and fault tree analysis (right)

The air data system provides important information about the environmental conditions, notably, Mach number. Three independent air data systems are used with each feeding independent flight control systems. This ensures that even if one air data system malfunctions or is obstructed, the two systems still functioning will be able to vote it out allowing the flight to continue safely. Besides using air data for flight control, the data is also sent to the ISR payload. This allows for the onboard sensors to adjust to current conditions. For instance, when high Mach numbers are reached, a plasma sheath could impact the sensors and certain parameters might need to be adjusted. To evaluate the redundancy and potential failure points of the Hyperhawk system, the fault tree shown above was developed. The full breakdown of all electrical subysystems can bee seen below.

Table 18-1: Power Budget

Baby Jay			
Item	Engaged Power (W)	Engaged Time (s)	Engaged Energy (J)
Flight Computer / Avionics	200	10800	2160000
ISR Package	2000	10800	21600000
Radio Link	100	10800	1080000
Elevon Actuators	3000	300	900000
Engine Gimbal Actuators	2000	300	600000
Engine Start	1000	5	5000
RCS Solenoids	300	10800	3240000
Cooling	500	1800	900000
Engine output req.	6300	Varies on mission	Varies with mission
Hyperhawk			
Item	Engaged Power (W)	Engaged Time (s)	Engaged Energy (J)
Elevon Actuators	10000	120	1200000
Engine Gimbal Actuators	5000	120	600000
Engine Ignition System	5000	120	600000
Engine output req.	15000	120	1800000

19. COMMUNICATION SUBSYSTEM

The Hyperhawk is meant to be completely autonomous or optionally commanded by a ground station to meet the RFP requirements. For this reason, the communication system will utilize two different forms of communication, a radio frequency (RF) signal and a free-space optical system via the use of lasers. The RF signal communication system will utilize two separate bands of frequencies, the Ka band and S band. Laser based free-space optical communication systems have capability to transmit gigabits of data per second. A current project by Ball Aerospace is working on a data rate of 100 gigabits per second. Whereas the backup Ka band communication system can transmit around 300 megabits per second. Then the S band is down around 10 megabits per second in data transfer. The bandwidth of the laser system is much greater than that of the RF signal-based communication systems. A laser communication system only has one way for the message to be intercepted, that is by getting in between the sender and the receiver. Thus, making it difficult to eavesdrop whereas a RF signal has a large beam width, and the signal isn't entirely consumed by the receiver. RF signals tend to propagate through the ionosphere and increase the travel distance of the message. The RF transmissions and received messaged will be encrypted to protect the security of the vehicle and the mission. The RF antennas will be in the wings and the laser system will be located near the nose of the vehicle. This will enable the laser to be aimed precisely on the intended satellite.

Operational use of these systems will be dependent on the situation of the mission. During the endo-atmospheric mission, all communications will be conducted through the laser system. As the vehicle is ascending to the operational altitude, the laser system will connect to a nearby ground station to provide vehicle life data and receive commands for the upcoming operation. Once Baby Jay is released from the core stage, all communications from the laser system will go through a network of government satellites. Baby Jay will aim the laser system to nearest friendly satellite and secure connection as seen in the Figure below.

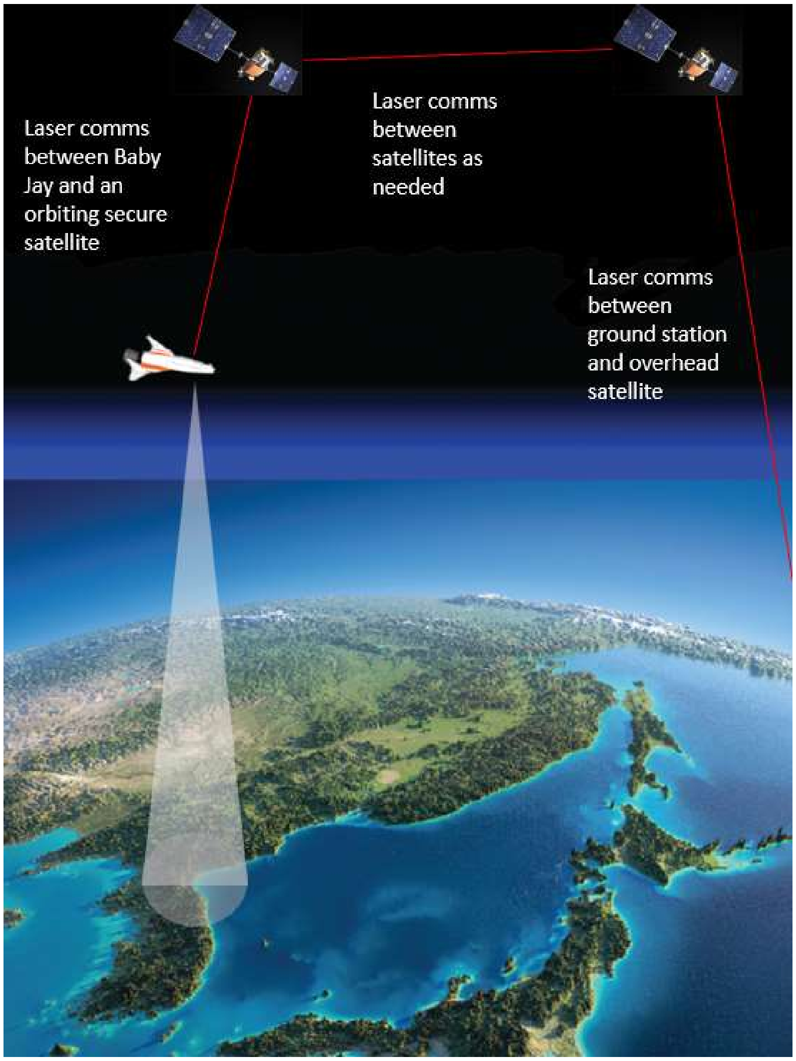

Figure 19.1: Laser Comms Diagram

This makes the connection and transfer of data secure and reliable. The Ka band and S band RF communication systems will only operate if the laser system is inoperable. This communication system will send and receive all data and commands from overhead satellites. Transmissions will occur before and after the ISR payload records data over the target. This will reduce the likeliness of the RF signal from reaching unwanted ground station antennas.

Operation of the communication system during an exo-atmospheric will not start until Baby Jay is inserted into the desired orbit. This is due to the communication from the ground stations and the launch vehicle. After separation, Baby Jay will be connected shortly by an RF signal to gain tracking details and vehicle life data. During this time the laser system will begin to be aimed at either at a ground station or a nearby satellite. This will depend on the availability of both and the location of Baby Jay. Once the laser communication system is operable, the RF transceivers in Baby Jay will turned receive mode. This will make the system quiet and have the capability of receiving messages if the laser systems fail. Otherwise, all data transfers will be as such; Baby Jay to a nearby satellite, then satellite to satellite till the final satellite is in the field of view of the intendent ground station. At which point, the data packet will be transferred to the ground. This process will be reverse for messages being transmitted to Baby Jay. If Baby Jay happens to be within the field of view of the ground station while recording the ISR data or right after, Baby Jay can transmit directly to the ground. This could be used during military operations, as providing a secure overhead view during a ground troop operation can provide a strategic tactical advantage if the information is time sensitive.

Once the mission life is complete for either mission profiles a signal from the ground station will be sent to the vehicle to deorbit. There will be a moment where the plasma caused by reentry will create a communication blackout. Once the Baby Jay is back in the atmosphere and gliding to the landing zone, all communication will be through the S band antenna till touch down. This RF band requires the lease amount of power to operate and has an abundant amount of ground stations that can be operated.

20. CLASS II WEIGHT AND BALANCE

To find the weight and balance for such a unique vehicle, many assumptions and estimations must be made. The overall weight of the Baby Jay is based on the performance code and made to match the X-37b which has a maximum takeoff weight of 5 metric tons. The fuel weight of the vehicle, however, is not in the public domain and is estimated using the space shuttle's orbital maneuvering system fuel weight to empty weight ratio. The RCS system weight is based on the Apollo service module. Structural components are estimated using Roskam's *Airplane Design Part V* [29] with some multiplying coefficients for the higher structural loads and specialized materials required at high speeds. The weight estimation of some of the smaller items were based on ratios to comparable systems. Given that the recovery parachute will deploy in a deep stall at similar speeds and altitudes as a skydiver, the parachute weight is estimated using the T-10 parachute in service with US armed forces. This parachute weighs 14 kg and can safely slow a 160 kg payload. This ratio is multiplied by the empty weight of the Baby Jay. The airbags are likewise estimated based on the Mars Pathfinder landing system which used two dozen spherical airbags to safely arrest the vehicle upon impact with the Martian surface. The fuel tank weights were estimated using the following equation found in Rocket Propulsion Elements.

$$\boldsymbol{Tank\ empty\ weight = 0.7266 \times (Pressure \times Volume)^2 + 2.5119 \times Pressure \times Volume + 2.9826}$$

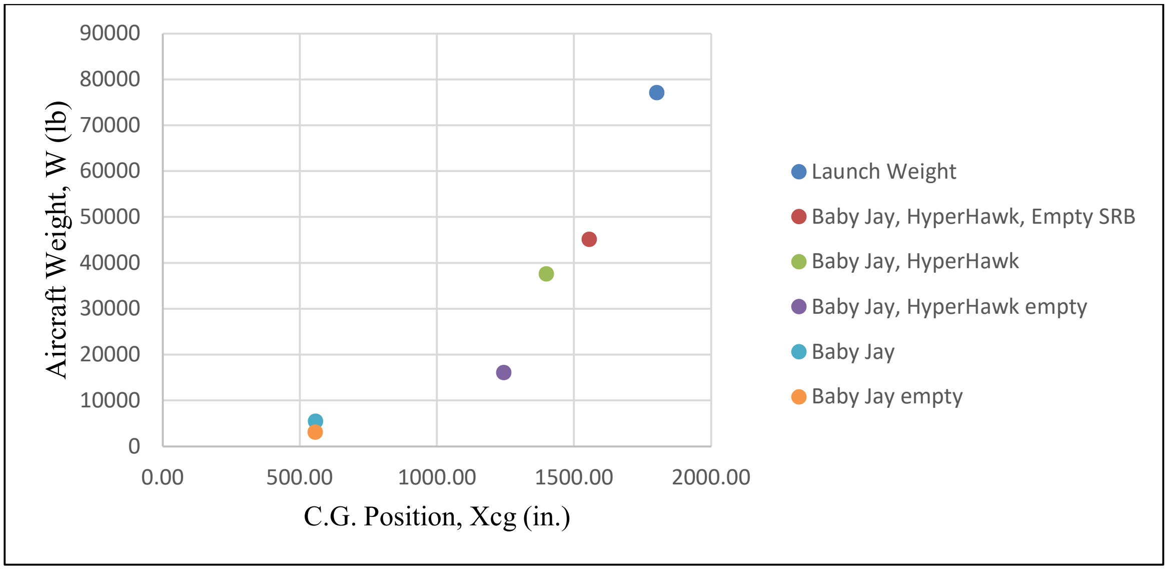

Figure 20.1: C.G. excursion at each stage

Table 20-1: Weight and balance breakdown

Component	Weight (kg)	Weight Fraction	Xcg (cm)	Ycg (cm)	Zcg (cm)
Aircraft Total (Launch Weight)	77132.11	100.00%	1802	-4	0
Payload	460	0.60%	230	0	0
Flight Computer / Avionics	60	0.08%	50	0	0
VHF SATCOM 1	5	0.01%	230	20	0
VHF SATCOM 2	5	0.01%	230	-20	0
Parachute	263	0.34%	250	0	0
Airbag Port	50	0.06%	750	640	0
Airbag Starboard	50	0.06%	750	-640	0
Airbag Forward	50	0.06%	80	0	0
Gas generator	100	0.13%	650	20	0
Main Wing Structure	500	0.65%	650	0	0
Stabilizer Structure Port Upper	125	0.16%	680	640	-50
Stabilizer Structure Starboard Upper	125	0.16%	680	-640	-50
Stabilizer Structure Port Lower	125	0.16%	680	640	50
Stabilizer Structure Starboard Lower	125	0.16%	680	-640	50
Rudder Hydraulic Sys Port	150	0.19%	800	100	0
Rudder Hydraulic Sys Starboard	150	0.19%	800	-100	0
Elevon Hydraulic Sys Port	150	0.19%	800	100	0
Elevon Hydraulic Sys Starboard	150	0.19%	800	-100	0
4 way RCS forward port	75	0.10%	25	35	0
4 way RCS forward starboard	75	0.10%	25	-35	0
2 way RCS wing port	40	0.05%	790	120	0
2 way RCS wing starboard	40	0.05%	790	-120	0
Engine	120	0.16%	1100	0	0
Helium Tank	19	0.02%	110	0	0
Fuel Tank	46	0.06%	450	0	0
LOX Tank	55	0.07%	630	0	0
Fixed Total	3112	4.03%	553	1	0
Fuel (RP-1)	938	1.22%	450	0	0
Oxidizer (LOX)	1482	1.92%	630	0	0
Baby Jay (Stage 3)	5532	7.17%	556	0	0

Table 20-1: Weight and balance breakdown (continued)

Main Wing Structure	3400	4.41%	1680	0	0
Stabilizer Structure Port Upper	250	0.32%	1750	830	120
Stabilizer Structure Starboard Upper	250	0.32%	1750	-830	120
Stabilizer Structure Port Lower	250	0.32%	1750	830	-120
Stabilizer Structure Starboard Lower	250	0.32%	1750	-830	-120
Rudder Hydraulic Sys Port	300	0.39%	1750	750	0
Rudder Hydraulic Sys Starboard	300	0.39%	1750	-750	0
Elevon Hydraulic Sys Port	300	0.39%	1720	800	0
Elevon Hydraulic Sys Starboard	300	0.39%	1720	-800	0
Fuel Tank	1455	1.89%	1200	0	0
LOX Tank	3567	4.62%	1600	0	0
Fixed Total	10622	13.77%	**1600**	**0**	**0**
Fuel (RP-1)	6630	8.60%	1150	0	0
Oxidizer (LOX)	14848	19.25%	1680	0	0
Core (Stage 1)	32100	41.62%	**1544**	**0**	**0**
Fin 1	1500	1.94%	2340	100	100
Fin 2	1500	1.94%	2340	100	-100
Fin 3	1500	1.94%	2340	-100	100
Fin 4	1500	1.94%	2340	-100	-100
Fuselage / Tank	1500	1.94%	2340	0	0
Fixed Total	7500	9.72%	**2340**	**-40**	**0**
Fuel (Solid)	32000	41.49%	2150	0	0
SRB (Stage 1)	39500	51.21%	**2186**	**-8**	**0**
Empty Weight Complete	21234	27.53%			

21. CLASS I STABILITY AND CONTROL

The purpose of this section of the report document is to analyze both the longitudinal and directional stability of the Baby Jay, core stage, and the entire Hyperhawk. To do this, X-Plots were created for each of the possible flight conditions for the aircraft: The Baby Jay in subsonic and supersonic conditions, the core stage in supersonic flight, and the Hyperhawk in both subsonic and supersonic conditions. The main equation used to find $\bar{X}_{AC,\,A}$ for the longitudinal X-Plots can be seen below.

$$\bar{X}_{AC,A} = \frac{\bar{X}_{AC,wf} * C_{L,\alpha,wf} + C_{L,ah}\left(1 - {}^{d\varepsilon_h}/_{d\alpha}\right)\frac{S_h}{S}\bar{X}_{AC,h} - C_{L,ac}(1 + {}^{d\varepsilon_c}/_{d\alpha})\frac{S_c}{S}\bar{X}_{AC,c}}{C_{L,\alpha,wf} + C_{L,ah}\left(1 - {}^{d\varepsilon_h}/_{d\alpha}\right)\frac{S_h}{S} - C_{L,ac}(1 + {}^{d\varepsilon_c}/_{d\alpha})\frac{S_c}{S}} \qquad \text{Eq. 14.1 [30]}$$

Because the Baby Jay is the final stage of our aircraft, it will have to be stable by itself during its own independent flight. Therefore, the Baby Jay was the first stage of our aircraft that was evaluated. As stated previously in the report document, the Baby Jay will fly in both a supersonic and a subsonic case which means that two different longitudinal X-Plots would need to be generated. Figure 21.1 and Figure 21.2 show these two X-Plots for the different flight conditions. As it can be seen for the supersonic flight condition of the Baby Jay, the wing would have to have a size of 150 sq-ft to produce a static margin of roughly 40%.

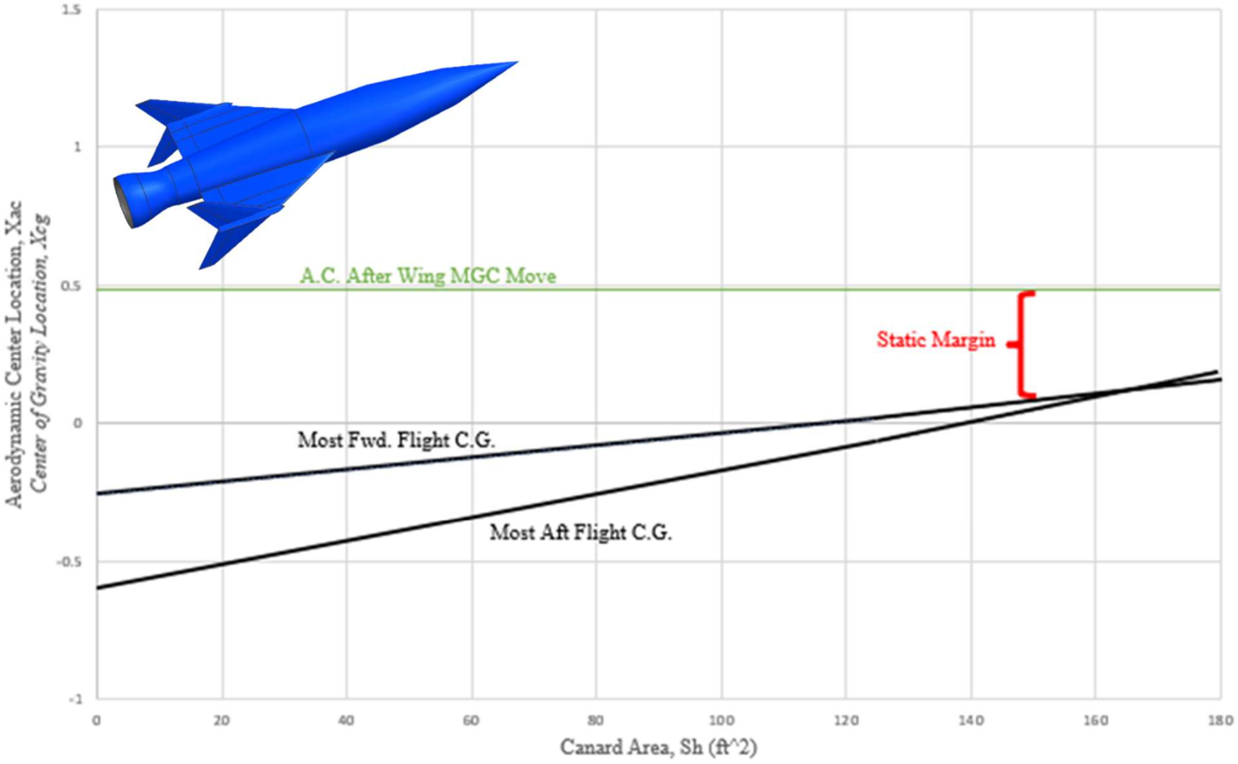

Figure 21.1: Supersonic Flight Canard longitudinal x-plot

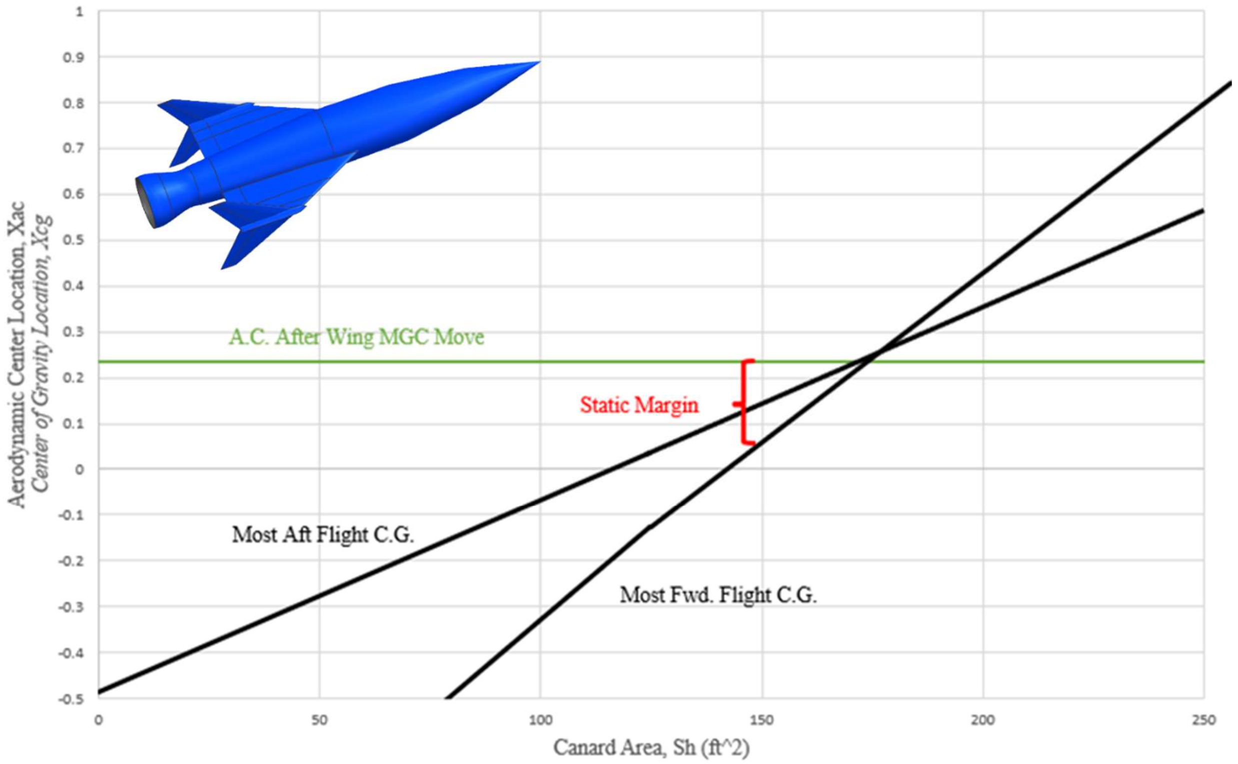

Figure 21.2: Subsonic Flight Canard Longitudinal X-Plot

Although this static margin is rather high with the designed wing under the supersonic case, the Baby Jay should also be analyzed with the same area under the subsonic case. As can be seen in Figure 21.2 a wing area of 150 sq-ft will produce a static margin of about 10% under the supersonic case due to the aerodynamic center of the canard being located at only 25% of the mean geometric chord rather than 50% for the supersonic case. Overall, the supersonic design for the Baby Jay is going to be the governing flight condition, therefore the canard of the aircraft will have to be sized to be 150 sq-ft regardless of the larger static margin under subsonic conditions.

Once the wing located on the Baby Jay has been sized appropriately, the core flight configuration under supersonic conditions can then be evaluated. Following the same steps shown previously, the longitudinal X-Plot for this flight configuration can be seen in Figure 21.3 below. Prior to analyzing the static margin of this configuration, more of the aircraft geometry with respect to the aircraft's center of gravity must first be understood. Because the wing located on the Baby Jay is forward of the center of gravity of the current configuration, the Baby Jay wing will be destabilizing when the angle of attack of the airflow is greater than zero degrees. Therefore, the main wing will have to be sized to be larger to account for any negative effects. From the data shown, it can be seen that in order to produce a static margin of 10%, the main wing of the aircraft would have to be sized to be 900 sq-ft.

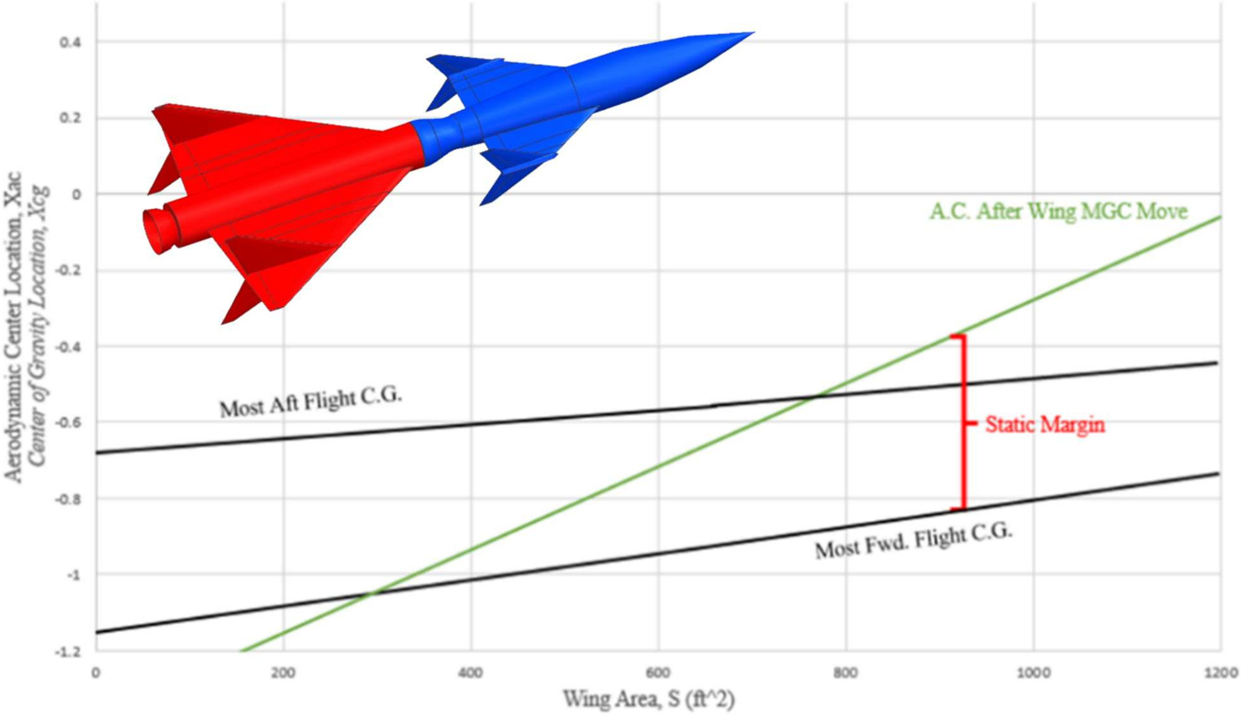

Figure 21.3: Core stage supersonic flight wing longitudinal x-plot

Following the design of the wings of the aircraft, the horizontal tail located on the SRB can also be sized. Similar to what occurred when designing the wing of the Baby Jay, the SRB is also going to have both subsonic and supersonic flight conditions. Upon performing the same longitudinal X-Plot analysis for the X-Plots in Figure 21.4 and Figure 21.5, it can be seen that the supersonic case is the governing flight condition by producing lower static margins for the same hypothetical horizontal tail area. Although the horizontal tail area could be designed to be smaller while also producing a desirable static margin, it was decided for this stage that the horizontal tail areas would be designed to be identical to the size and shape of the vertical tails for the SRB to be both axisymmetric as well as to increase manufacturing simplicity by reducing the different types of parts that have to be assembled and installed. Although the vertical tail sizing will be discussed later in this same section of the report document, it was found that the SRB vertical tails are required to be larger than the horizontal tails for directional stability, thus resulting in the larger static margins for the Hyperhawk flight configuration.

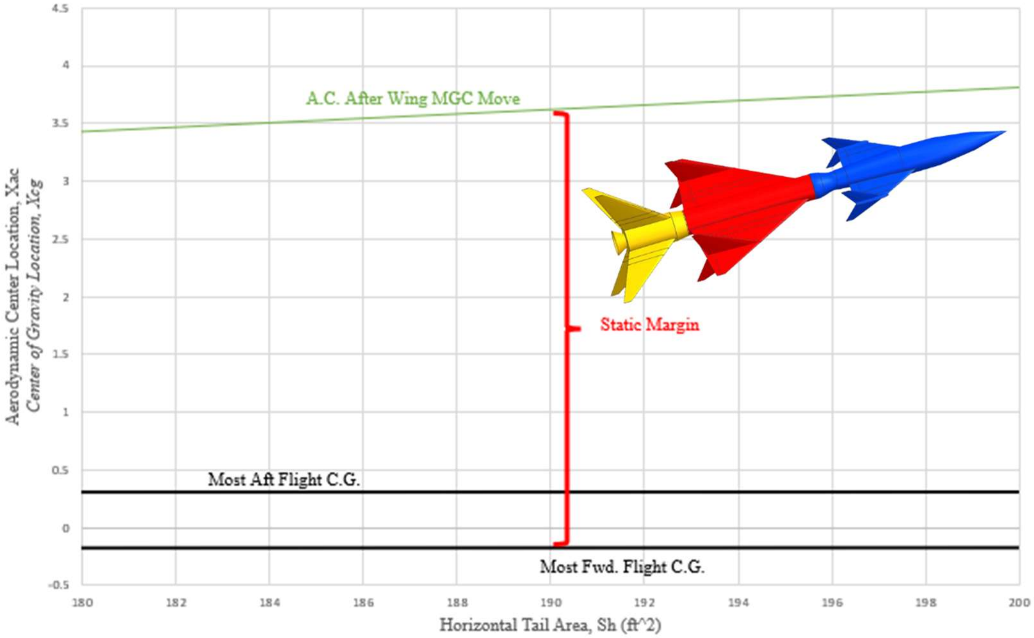

Figure 21.4: Hyperhawk subsonic flight horizontal tail longitudinal x-plot

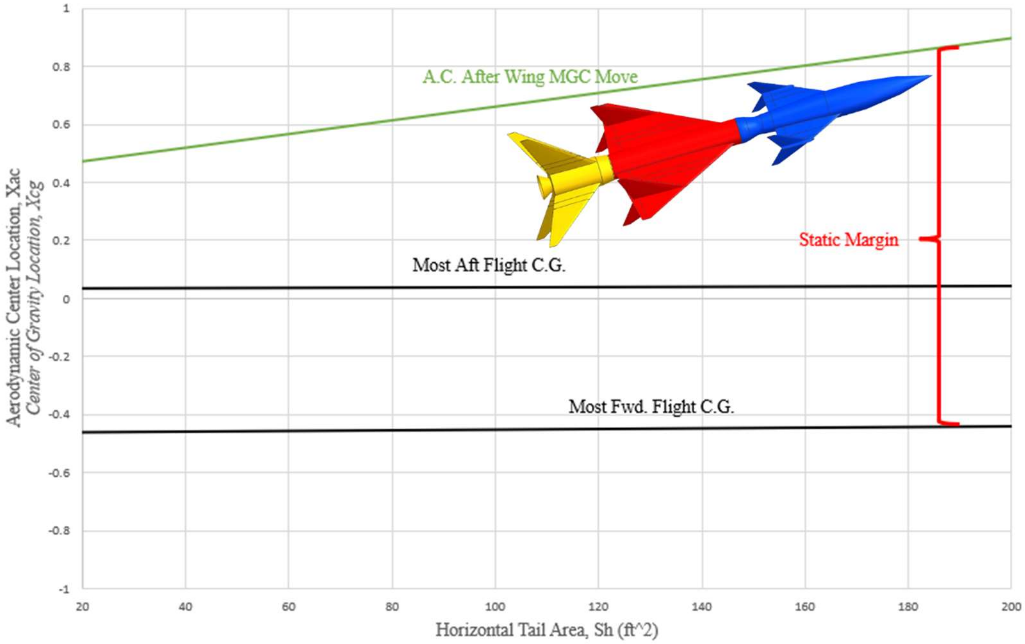

Figure 21.5: Hyperhawk supersonic flight horizontal tail longitudinal x-plot

In addition to the longitudinal X-Plots, directional X-Plots can also be generated which can also be seen in the subsequent figures below. The equation that was used to calculate the value of the yawing moment coefficient due to side slip angle can also be seen below.

$$C_{n\beta} = C_{n\beta,wf} + C_{L,av}\left(\frac{S_v}{S}\right)\left(\frac{x_v}{b}\right) \qquad \text{Eq. 14.2 [30]}$$

For the same reason as stated previously, the Baby Jay would also be the first stage of the aircraft to be designed to have directional stability. Once again, the Baby Jay is evaluated at two different flight conditions, one of which being at subsonic speed while the other is evaluated at supersonic speeds. As it can be seen in Figure 21.6 and Figure 21.7 below, a vertical tail area of roughly 8 sq-ft is required for directional stability under the subsonic case while a vertical tail area of 68 sq-ft is required under the supersonic case for directional stability. Because the supersonic case is governing for the Baby Jay, the vertical tail area is needed to be 68 sq-ft on this stage of the aircraft.

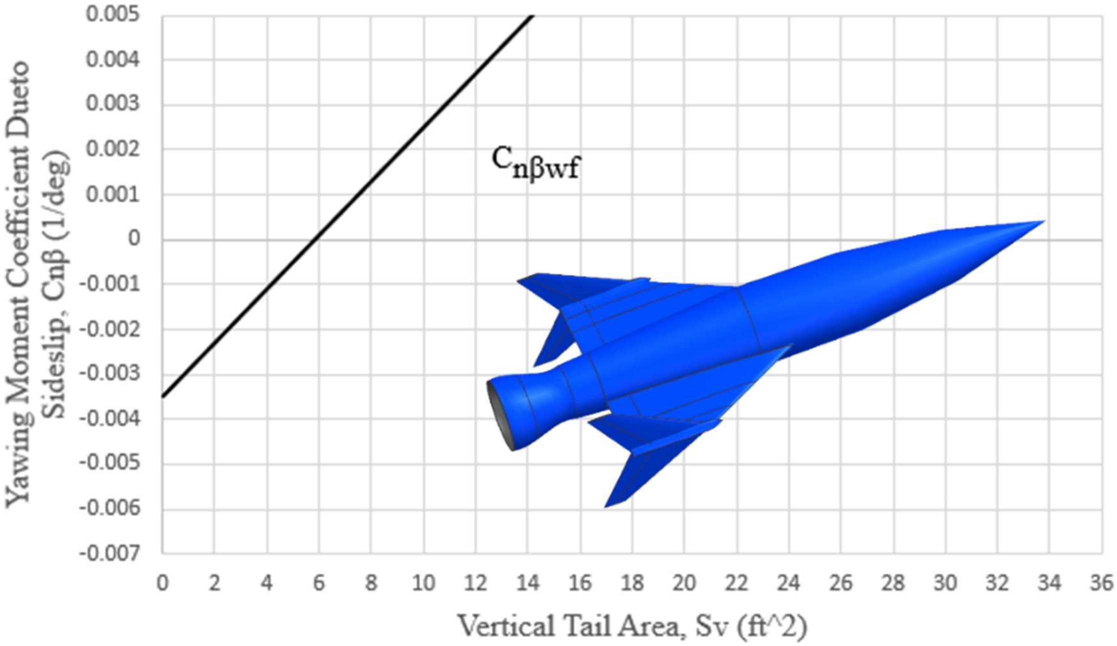

Figure 21.6: Baby Jay Subsonic Directional X-Plot

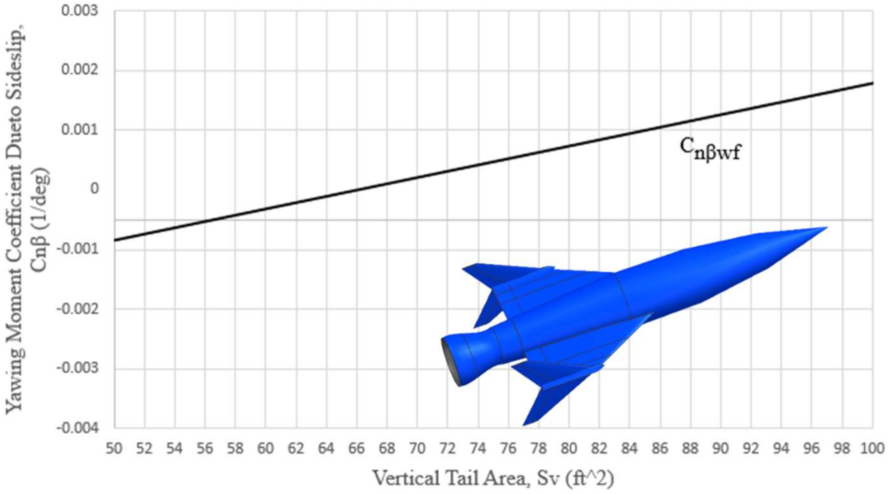

Figure 21.7: Baby Jay Supersonic Directional X-Plot

Once the vertical tail on the Baby Jay was determined to be 68 sq-ft, the vertical tail area for the Hyperhawk can then be calculated. Figure 21.8 below shows the directional X-Plot for the Hyperhawk and Baby Jay in supersonic flight. As it can be seen in this figure, the value for $C_{l\beta}$ to be 0.001 requires a vertical tail area of 174 sq-ft to be directionally stable. It should also be noted that because the vertical tail on the Baby Jay is located forward of the center of gravity for this flight configuration, the Baby Jay vertical tail will be destabilizing when a there is a nonzero sideslip angle present for the aircraft, thus resulting in a large vertical tail area for the core stage.

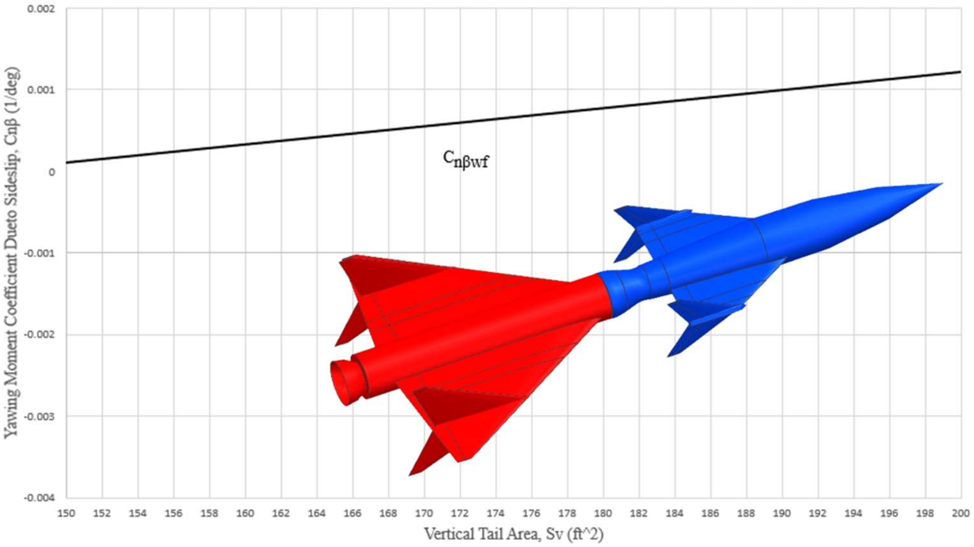

Figure 21.8: Hyperhawk Supersonic Directional X-Plot

Finally, the directional X-Plots for the Hyperhawk can be created using the same method as previously shown. As previously sated, the Hyperhawk flight configuration has two different flight conditions, one in subsonic flight and the other in supersonic flight. As it can be observed in Figure 21.9 and Figure 21.10**,** the required vertical tail areas for the SRB under subsonic and supersonic conditions are 190 sq-ft and 182 sq-ft respectively. As it was previously stated in this section of the report, the vertical and horizontal tails for the SRB would be designed to be the same size. Because the governing design is the subsonic vertical tail on the SRB, every lifting surface on the SRB will be designed to have an area of 190 sq-ft.

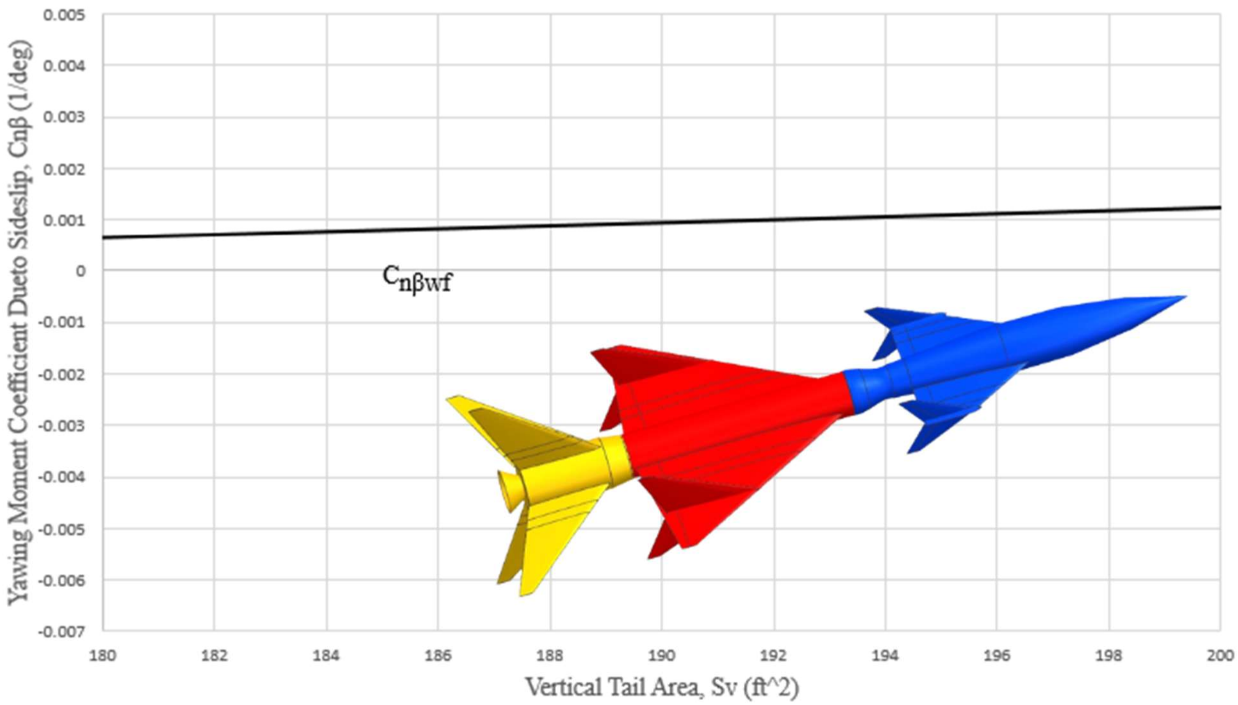

Figure 21.9: Hyperhawk with SRB Subsonic Directional X-Plot

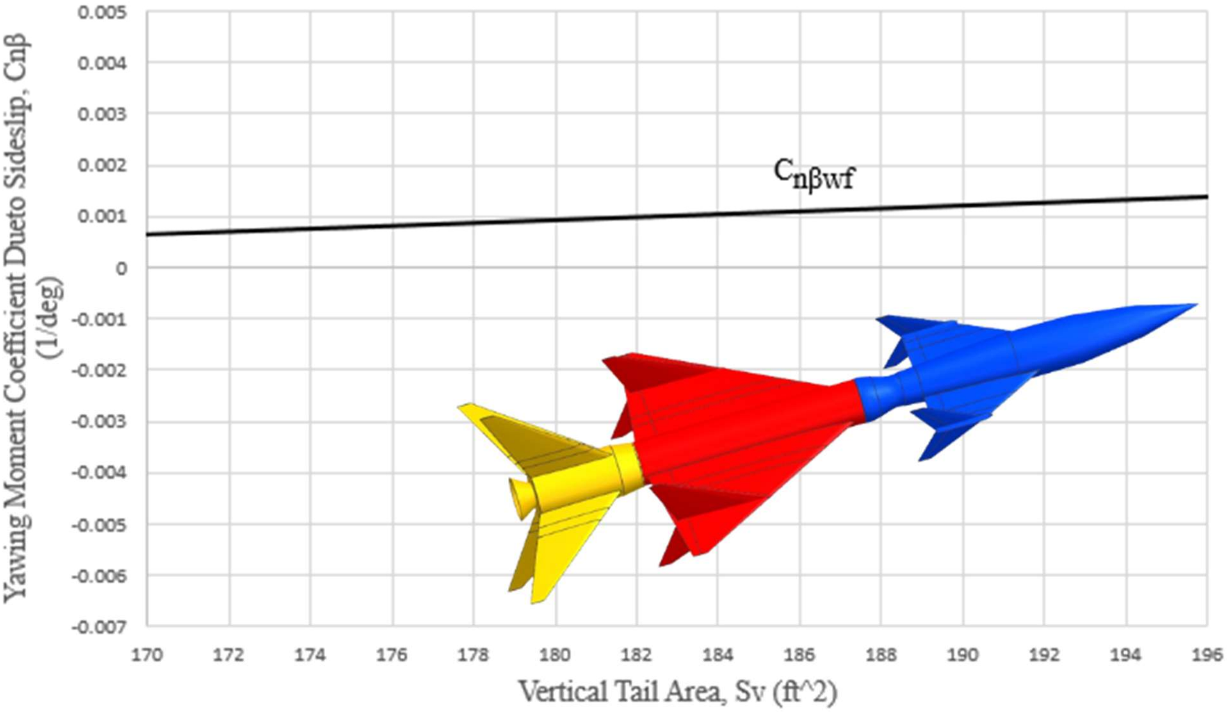

Figure 21.10: Hyperhawk with SRB Supersonic Directional X-Plot

To summarize all of the critical information provided during the class 1 stability analysis, Table 21-1 below outlines all of the lifting surface sizes for each stage of the aircraft design.

Table 21-1: Summary of class I stability and control

Longitudinal Lifting Surface	**Longitudinal Lifting Surface Area**
Baby Jay Canard	150 ft^2
Hyperhawk Wing	900 ft^2
SRB Horizontal Tail	190 ft^2
Directional Lifting Surface	**Directional Lifting Surface Area**
Baby Jay Vertical Tail	68 ft^2
Hyperhawk Vertical Tail	174 ft^2
SRB Vertical Tail	190 ft^2

22. CLASS II STABILITY AND CONTROL

Following the completion of class 1 stability for the aircraft, class II stability and control can be analyzed. For class II stability and control, the Advanced Aircraft Analysis (AAA) software package published by DARCorporation was used. For the three different geometries that were analyzed, each configuration had to be imported into the program before any analysis could begin. Figure 22.1 below shows the geometry of the aircraft after they have been imported into the program.

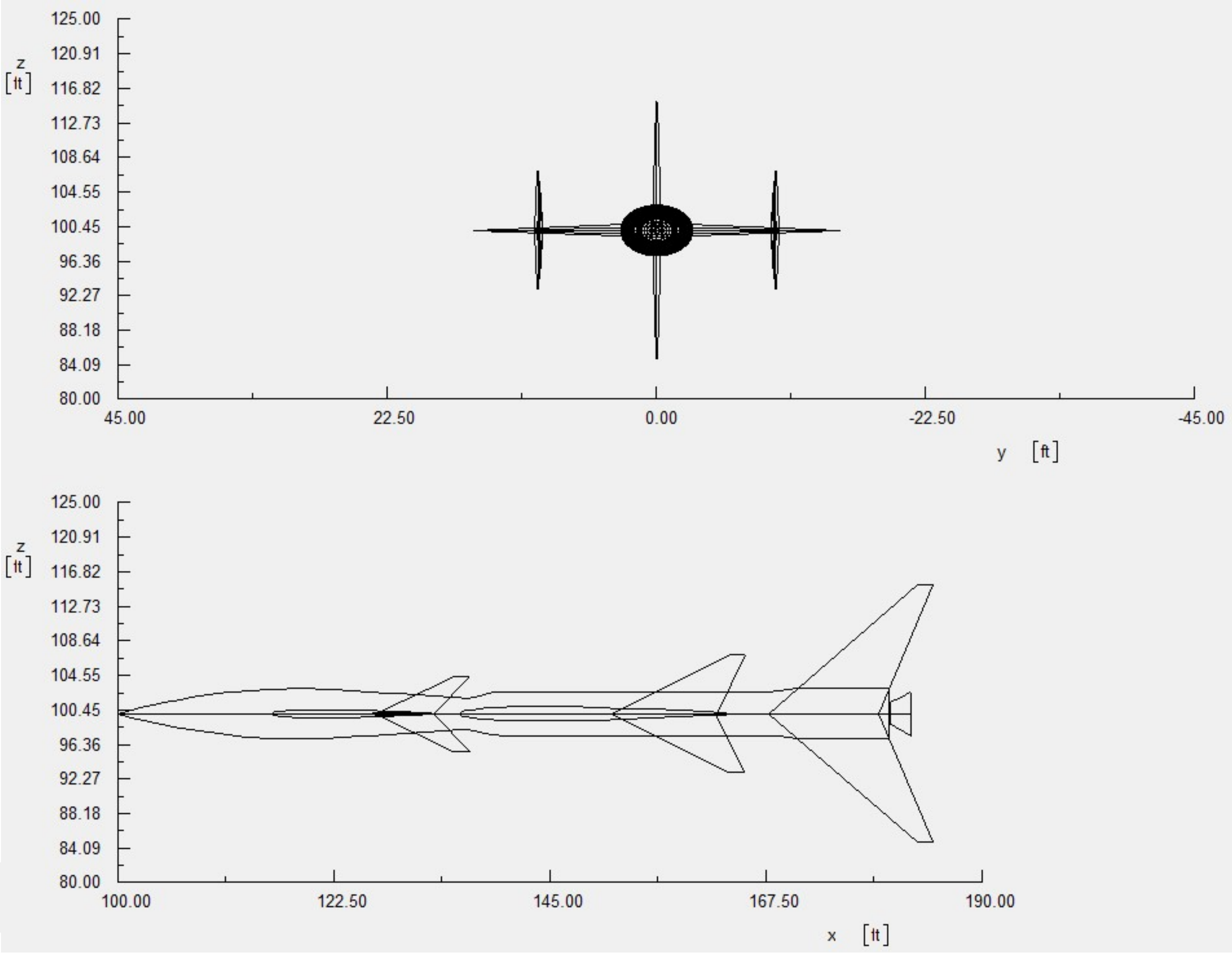

Figure 22.1: Hyperhawk AAA geometry, Z-Y and Z-X

Once the necessary aircraft geometry has been imported into AAA, the class II stability and control analysis can begin. Using the outputs produced by the AAA software, the stability and control derivatives for the aircraft can be ascertained. Additionally, the AAA also provides the user with the damping ratios and natural frequencies of longitudinal and lateral directional dynamic modes. For the Baby Jay in both subsonic and supersonic flight conditions, the stability and control derivatives can be seen in **Error! Reference source not found.** and **Error! Reference source not found.** below.

Table 22-1: Baby Jay longitudinal stability and control derivatives

Stability and control variable	Subsonic	Supersonic
Lift Coefficient due to Forward Velocity, C_{Lu}	0.104	0.104
Drag Coefficient due to Forward Velocity, C_{Du}	0.000	0.000
Pitching Moment Coefficient due to Forward Velocity, C_{mu}	0.000	0.000
Lift Coefficient due to Angle of Attack, $C_{L\alpha}$ (rad^{-1})	2.057	0.321
Drag Coefficient due to Angle of Attack, $C_{D\alpha}$ (rad^{-1})	0.142	0.0027
Pitching Moment Coefficient due to Angle of Attack, $C_{m\alpha}$ (rad^{-1})	-1.111	-0.110
Lift Coefficient due to Angle of Attack Rate, $C_L\dot{\alpha}$ (rad^{-1})	0.000	0.000
Drag Coefficient due to Angle of Attack Rate, $C_D\dot{\alpha}$ (rad^{-1})	0.000	0.000
Pitching Moment Coefficient due to Angle of Attack Rate, $C_m\dot{\alpha}$ (rad^{-1})	0.000	0.000
Lift Coefficient due to Pitch Rate, C_{Lq} (rad^{-1})	4.4432	5.122
Drag Coefficient due to Pitch Rate, C_{Dq} (rad^{-1})	0.000	0.000
Pitching Moment Coefficient due to Pitch Rate, C_{mq} (rad^{-1})	-5.3391	-7.500
Lift Coefficient due to Elevator Deflection Angle, $C_{L\delta el}$ (rad^{-1})	0.2102	0.0246
Pitching Moment Coefficient due to Elevator Deflection Angle, $C_{m\delta el}$ (rad^{-1})	-0.2893	-0.0336

Table 22-2: Baby Jay lateral directional stability and control derivatives

Stability and control variable	Subsonic	Supersonic
Side Force Coefficient due to Side Slip Angle, $C_{y\beta}$ (rad^{-1})	-6.031	-2.573
Rolling Moment Coefficient due to Side Slip Angle, $C_{l\beta}$ (rad^{-1})	-0.018	-17.453
Yawing Moment Coefficient due to Side Slip Angle, $C_{n\beta}$ (rad^{-1})	5.016	2.352
Side Force Coefficient due to Side Slip Angle Rate, $C_y\dot{\beta}$ (rad^{-1})	-4.641	-2.809
Rolling Moment Coefficient due to Side Slip Angle Rate, $C_l\dot{\beta}$ (rad^{-1})	-0.103	-0.0858
Yawing Moment Coefficient due to Side Slip Angle Rate, $C_n\dot{\beta}$ (rad^{-1})	-2.401	-1.0058
Side Force Coefficient due to Roll Rate, C_{yp} (rad^{-1})	0.612	0.286
Rolling Moment Coefficient due to Roll Rate, C_{lp} (rad^{-1})	-0.161	-2.304
Yawing Moment Coefficient due to Roll Rate, C_{np} (rad^{-1})	-0.656	-0.414
Side Force Coefficient due to Yaw Rate, C_{yr} (rad^{-1})	11.6892	6.382
Rolling Moment Coefficient due to Yaw Rate, C_{lr} (rad^{-1})	-0.017	50.171
Yawing Moment Coefficient due to Yaw Rate, C_{nr} (rad^{-1})	-12.036	-9.462
Side Force Coefficient due to Aileron Deflection Angle, $C_{y\delta el}$ (rad^{-1})	0.000	0.000
Rolling Moment Coefficient due to Aileron Deflection Angle, $C_{l\delta el}$ (rad^{-1})	0.018	0.018
Yawing Moment Coefficient due to Aileron Deflection Angle, Cnδa (rad^{-1})	-0.001	-0.0001
Side Force Coefficient due to Rudder Deflection Angle, Cyδr (rad^{-1})	1.786	0.5905
Rolling Moment Coefficient due to Rudder Deflection Angle, Clδr (rad^{-1})	-0.033	4.633
Yawing Moment Coefficient due to Rudder Deflection Angle, Cnδr (rad^{-1})	-2.306	-1.004

These specific stability and control variables are significant because they dictate whether the designed aircraft will be laterally, directionally, and longitudinally stable based upon the signs of the values. To have lateral and longitudinal stability, the values for $C_{l\beta}$ and $C_{m\alpha}$ should both be negative while directional stability requires $C_{n\beta}$ to be positive. As it can be observed by the above tables, the values, in both subsonic and supersonic conditions, for $C_{l\beta}$, $C_{n\beta}$, $C_{m\alpha}$ are reported to have the proper signs for their respective stability requirements.

It should be noted that for the Baby Jay analysis performed in AAA, the canard area was changed from 150 sq-ft to 100 sq-ft. This design change was made for the Class II analysis because otherwise the canard for the Baby Jay would not be able to fit within the fairing panels of the SpaceX Falcon 9 rocket. To allow for such a design change, a longitudinal feedback loop would have to be developed for the canard. This was achieved by utilizing the techniques located in Roskam's Design Series [24,30] whose equations can be seen below. Upon calculating the difference in static margin using the static margin of the Baby Jay with the canard area of 100 sq-ft, the necessary value of k_α is computed to be ~8.56 to have de facto stability with a static margin of 10%.

$$\Delta SM = 10\% - SM_A$$

$$k_\alpha = \Delta SM \frac{C_{L\alpha}}{C_{m\delta el}}$$

$$C_{L\alpha} = C_{L\alpha,wf} + \left(1 + {}^{d\varepsilon_h}/_{d\alpha}\right)\frac{S_h}{S} + C_{L\alpha,c}(1 + {}^{d\varepsilon_c}/_{d\alpha})\frac{S_c}{S}$$

It should also be noted that to achieve level 1 longitudinal stability for both subsonic and supersonic flight, a gain was applied to C_{mq}. To determine what this gain should be, and iterative design process was performed in AAA until the desired handling requirements were met. This gain is quantified as the ratio or the original pitching moment coefficient due to pitch rate to the designed pitching rate coefficient due to pitch rate. Upon further analysis, the value for k_{cmq} was determined to be 14.299 to have level 1 longitudinal handling qualities for subsonic flight and then 1.942 for supersonic flight.

Once the stability and control derivatives have been calculated by AAA, the software can then determine the damping ratios and natural frequencies of the longitudinal and lateral directional modes encountered during flight. Table 22-3 below shows a list of the calculated stability metrics calculated by AAA for both the subsonic and supersonic flight conditions. As it can be observed in this table below, there is not a natural frequency nor damping ratio for the subsonic, longitudinal short period mode, this is because the dynamic mode is so damped that a short period mode simply does not exist for the Baby Jay.

As it can also be seen in this table below, the calculated static margins for the Baby Jay are higher than expected. The subsonic case for the Baby Jay reports having a static margin of 37.49%. Although this value is higher than ideal, this static margin can get trimmed out based upon the data presented in the subsonic trim diagram. Regarding the supersonic case with the static margin of 62.49%, the atmosphere where the Baby Jay flies supersonic is so rarified that the effects of this large static margin will be negligible.

Table 22-3: Baby Jay Stability and Control Metrics

Stability and control variable	Subsonic	Supersonic
Short Period Natural Frequency, ωnsp (rad/s)	~	2.332
Short Period Damping Coefficient, ζsp	~	0.38
Phugoid Natural Frequency, ωnph (rad/s)	6.4199	0.008
Phugoid Damping Coefficient, ζph	0.130	0.260
Dutch Roll Natural Frequency, ωndr (rad/s)	11.871	10.550
Dutch Roll Damping Coefficient, ζdr	0.190	0.125
Roll Mode Time Constant (s)	19.12	0.495
Spiral Mode Time Constant (s)	55.34	8.910
Static Margin (%)	37.49	62.49

Following the analysis of the dynamic modes of the Baby Jay, the trim diagrams of the aircraft for subsonic and supersonic flight conditions can be observed in Figures 21.8 and 21.9 respectively.

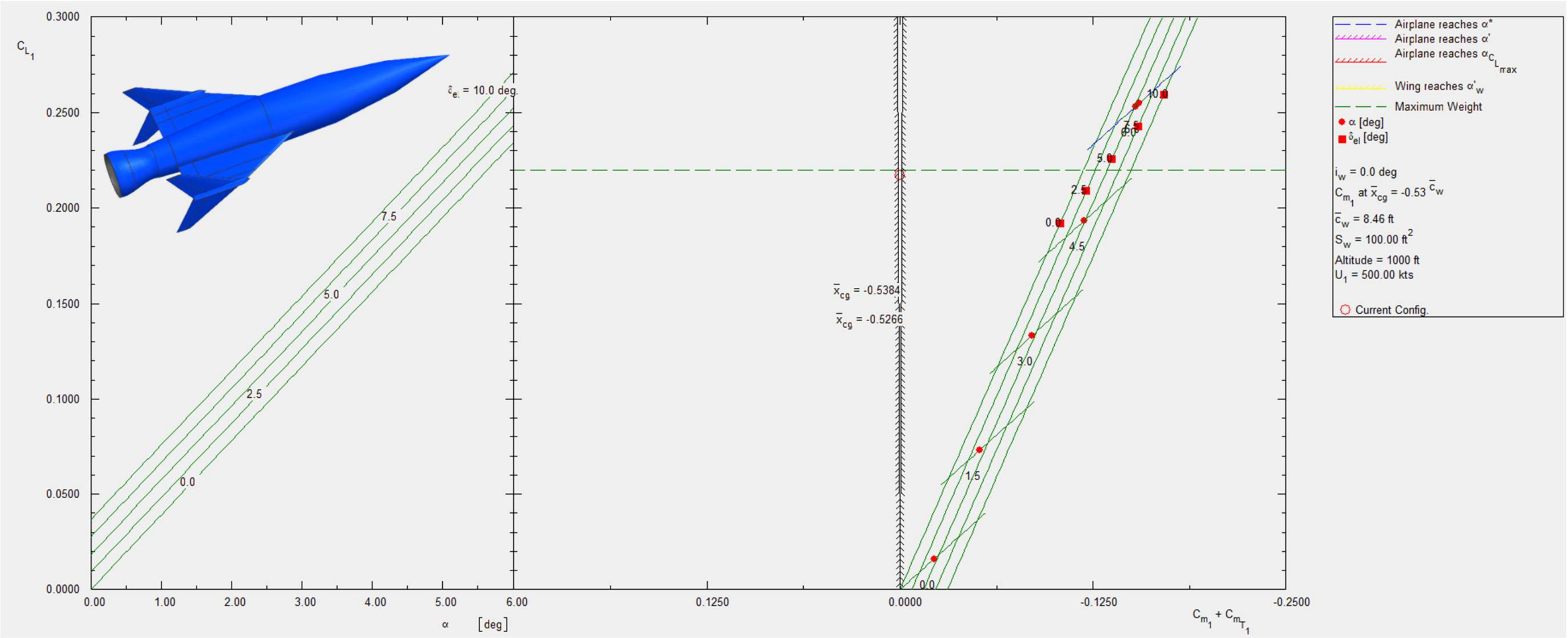

Figure 22.2: Baby Jay subsonic trim diagram

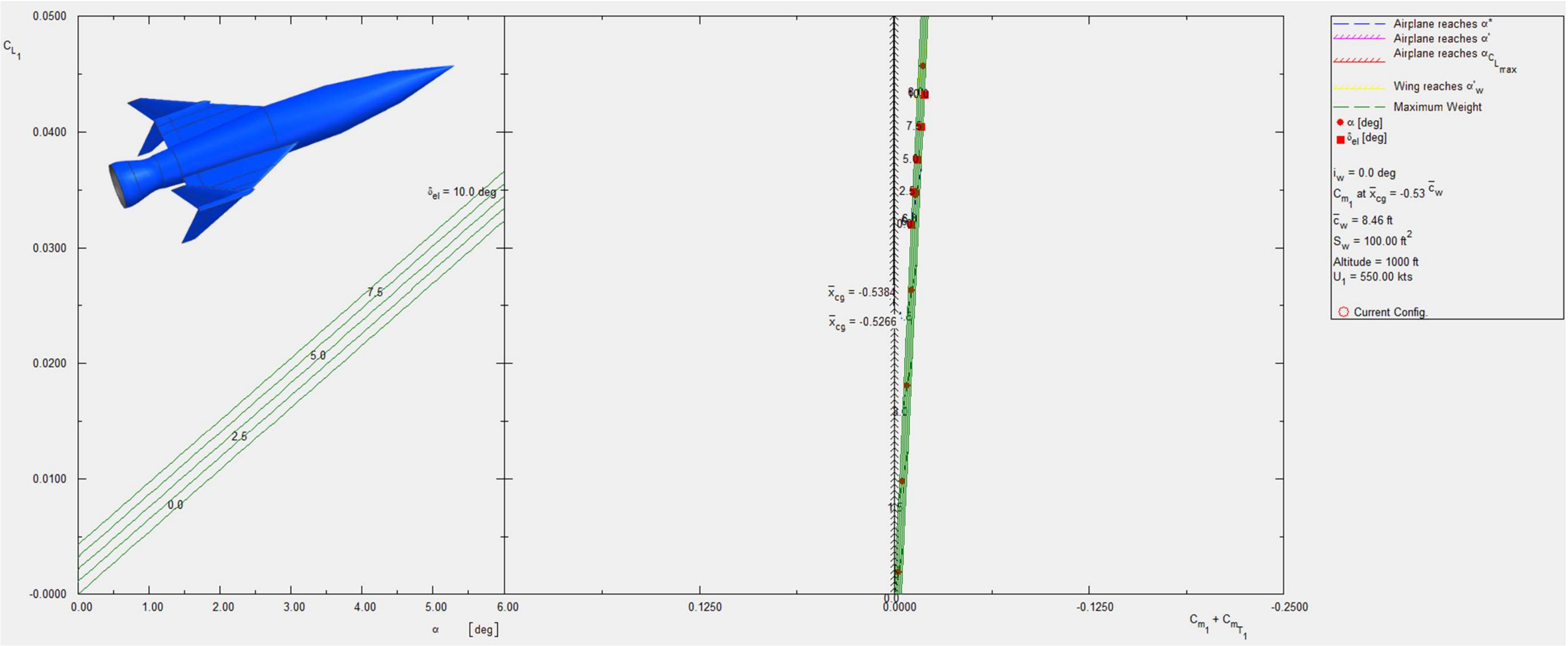

Figure 22.3: Baby Jay supersonic trim diagram

Following the creation of the trim diagrams, Figure 21.10 below shows the short period frequency requirement plot as created in AAA for the different levels of handling requirements. Because there is no short period for the subsonic case of the Baby Jay, the short period requirement plot for the subsonic flight condition is not shown, as there is no design point shown on the plot.

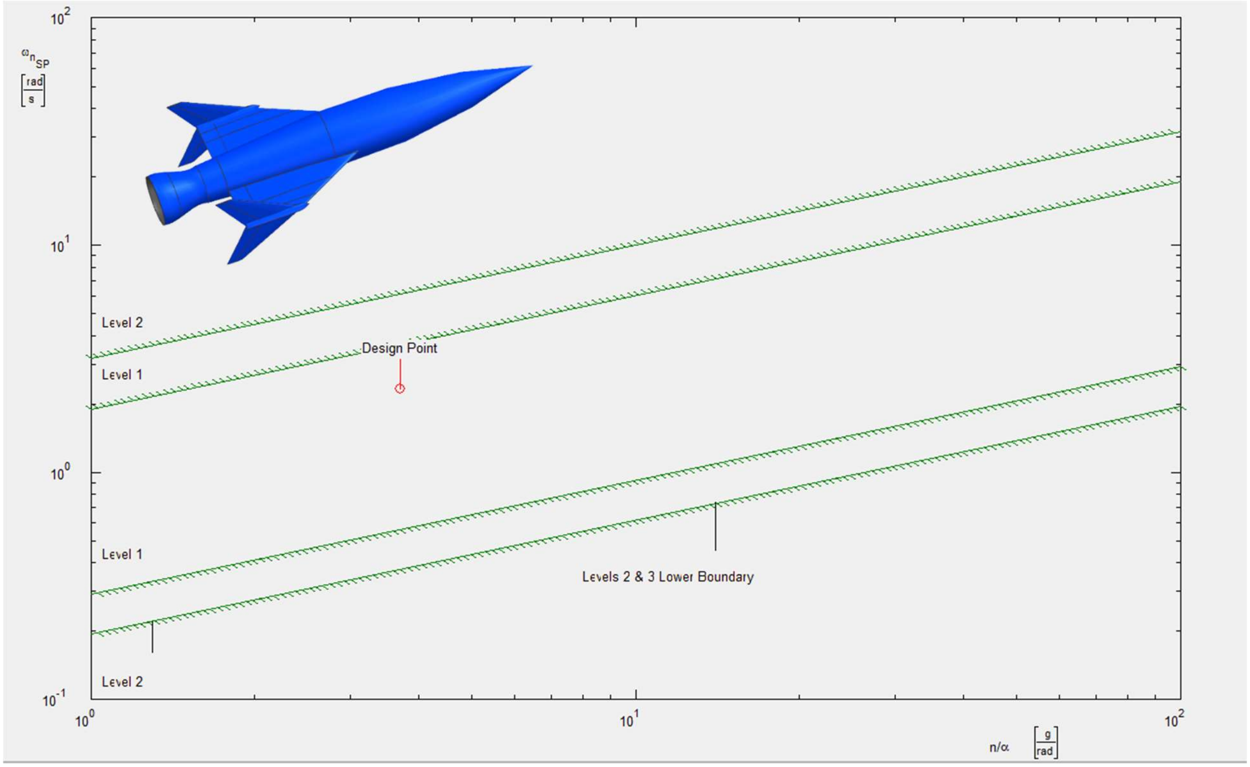

Figure 22.4: Baby Jay supersonic short period frequency requirement plot

Similar to how the short period frequency plot was generated for the Baby Jay, the Dutch roll damping ratio and natural frequency plots can be created which can also be seen in Figures 21.11 and 21.12 below.

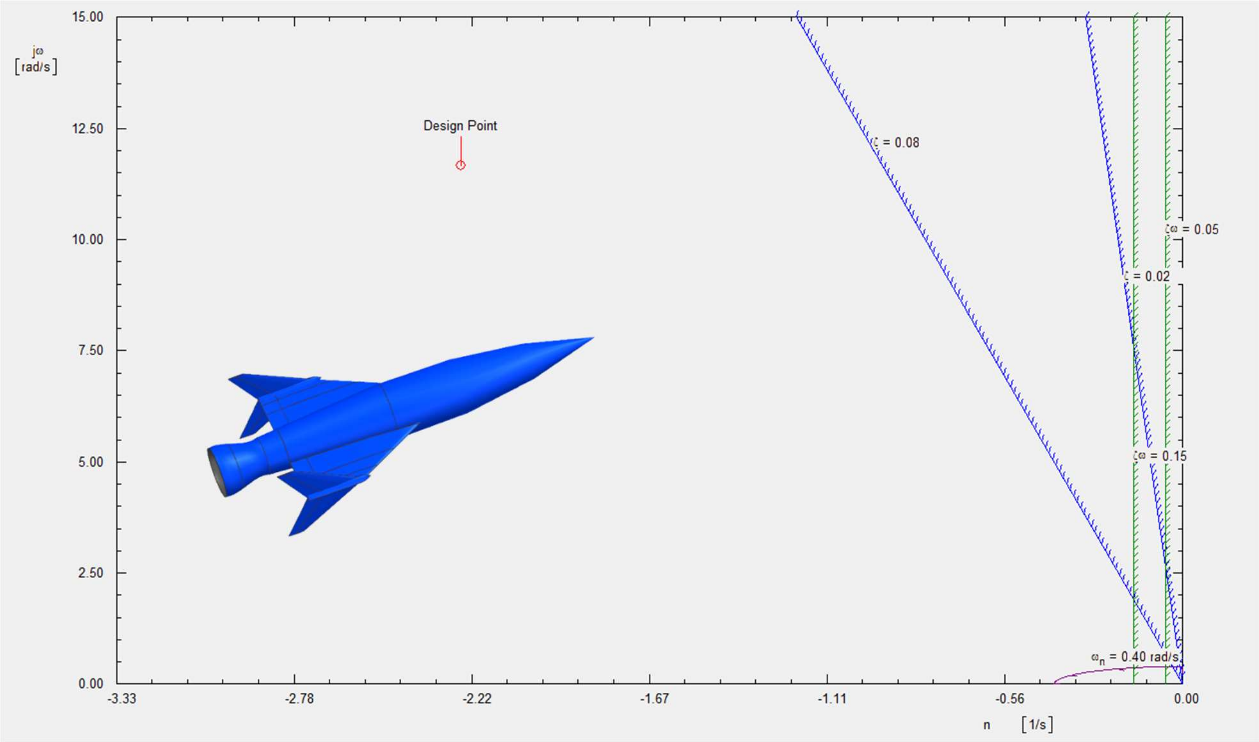

Figure 22.5: Baby Jay subsonic Dutch roll frequency and damping ratio requirement plot

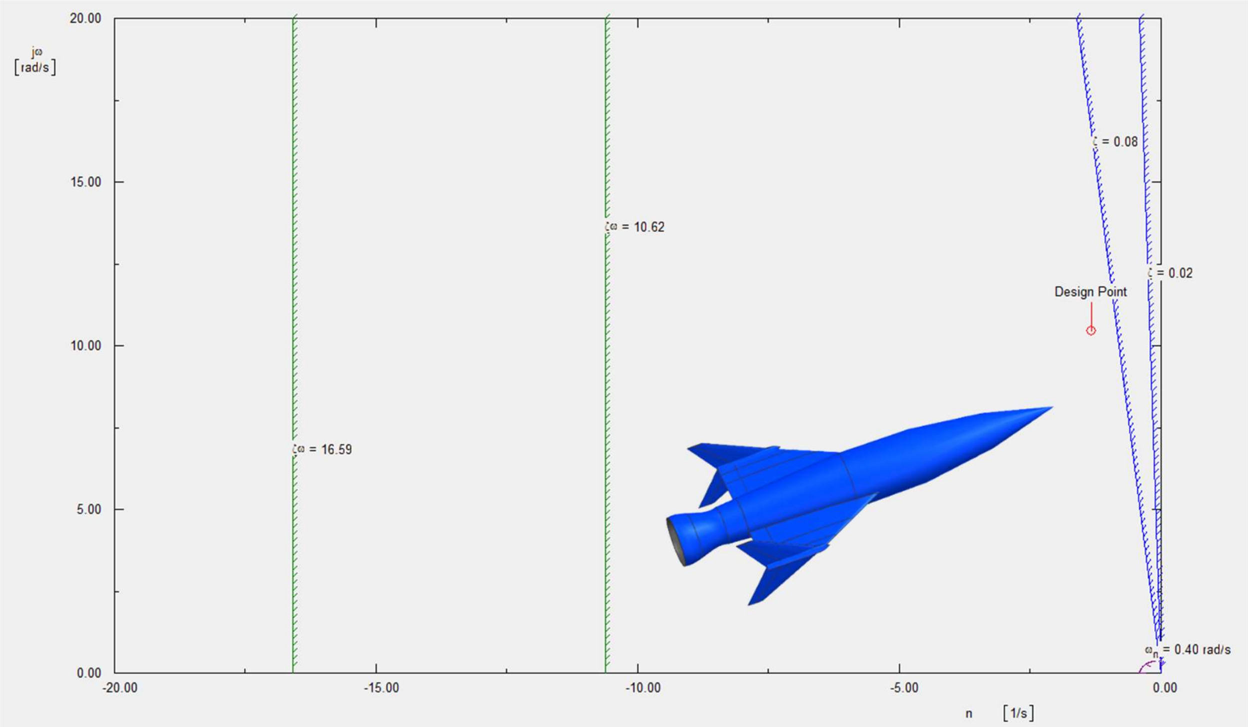

Figure 22.6: Baby Jay supersonic Dutch roll frequency and damping ratio requirement plot

Following the evaluation of the Baby Jay for its two flight conditions, the Baby Jay plus core geometry can also be evaluated for its single, supersonic flight condition. For the core stage in the supersonic flight condition, the stability and control derivatives can be seen in Table 22-4 and Table 22-5 below.

Table 22-4: Baby Jay plus core stage longitudinal stability and control derivatives

Stability and control variable	Supersonic
Lift Coefficient due to Forward Velocity, C_{Lu}	0.052
Drag Coefficient due to Forward Velocity, C_{Du}	0.000
Pitching Moment Coefficient due to Forward Velocity, C_{mu}	0.004
Lift Coefficient due to Angle of Attack, $C_{L\alpha}$ (rad^{-1})	1.526
Drag Coefficient due to Angle of Attack, $C_{D\alpha}$ (rad^{-1})	0.043
Pitching Moment Coefficient due to Angle of Attack, $C_{m\alpha}$ (rad^{-1})	-0.269
Lift Coefficient due to Angle of Attack Rate, $C_{L}\dot{\alpha}$ (rad^{-1})	-0.007
Drag Coefficient due to Angle of Attack Rate, $C_{D}\dot{\alpha}$ (rad^{-1})	0.000
Pitching Moment Coefficient due to Angle of Attack Rate, $C_{m}\dot{\alpha}$ (rad^{-1})	0.008
Lift Coefficient due to Pitch Rate, C_{Lq} (rad^{-1})	2.928
Drag Coefficient due to Pitch Rate, C_{Dq} (rad^{-1})	0.000
Pitching Moment Coefficient due to Pitch Rate, C_{mq} (rad^{-1})	-8.000
Lift Coefficient due to Elevator Deflection Angle, $C_{L\delta el}$ (rad^{-1})	0.409
Pitching Moment Coefficient due to Elevator Deflection Angle, $C_{m\delta el}$ (rad^{-1})	-0.2975

Table 22-5: Baby Jay plus core stage lateral directional stability and control derivatives

Stability and control variable	Supersonic
Side Force Coefficient due to Side Slip Angle, $C_{y\beta}$ (rad^{-1})	-3.049
Rolling Moment Coefficient due to Side Slip Angle, $C_{l\beta}$ (rad^{-1})	-0.373
Yawing Moment Coefficient due to Side Slip Angle, $C_{n\beta}$ (rad^{-1})	1.145
Side Force Coefficient due to Side Slip Angle Rate, $C_{y}\dot{\beta}$ (rad^{-1})	-0.207
Rolling Moment Coefficient due to Side Slip Angle Rate, $C_{l}\dot{\beta}$ (rad^{-1})	0.001
Yawing Moment Coefficient due to Side Slip Angle Rate, $C_{n}\dot{\beta}$ (rad^{-1})	-0.064
Side Force Coefficient due to Roll Rate, C_{yp} (rad^{-1})	0.128
Rolling Moment Coefficient due to Roll Rate, C_{lp} (rad^{-1})	-0.062
Yawing Moment Coefficient due to Roll Rate, C_{np} (rad^{-1})	-0.072
Side Force Coefficient due to Yaw Rate, C_{yr} (rad^{-1})	2.681
Rolling Moment Coefficient due to Yaw Rate, C_{lr} (rad^{-1})	-0.012
Yawing Moment Coefficient due to Yaw Rate, C_{nr} (rad^{-1})	-1.312
Side Force Coefficient due to Aileron Deflection Angle, $C_{y\delta el}$ (rad^{-1})	0.000
Rolling Moment Coefficient due to Aileron Deflection Angle, $C_{l\delta el}$ (rad^{-1})	0.061
Yawing Moment Coefficient due to Aileron Deflection Angle, $Cn\delta el$ (rad^{-1})	-0.0002
Side Force Coefficient due to Rudder Deflection Angle, $Cy\delta r$ (rad^{-1})	0.299
Rolling Moment Coefficient due to Rudder Deflection Angle, $Cl\delta r$ (rad^{-1})	-0.005
Yawing Moment Coefficient due to Rudder Deflection Angle, $Cn\delta r$ (rad^{-1})	-0.178

As it was stated previously, to have lateral and longitudinal stability, the values for $C_{l\beta}$ and $C_{m\alpha}$ should both be negative while directional stability requires $C_{n\beta}$ to be positive. As it can be observed by the above tables, the values for $C_{l\beta}$, $C_{n\beta}$, $C_{m\alpha}$ are reported to have the proper signs to meet requirements.

It should be noted that for the core stage analysis performed in AAA, the wing area was changed from 900 sq-ft to 468 sq-ft. This design change was made for the Class II analysis because otherwise the design would be difficult to manufacture and transport. To allow for such a design change, the static margin calculated in AAA would have to be analyzed. Because this static margin was found to be 6.75% which was considered to be good enough for this geometry due to the rarified atmosphere that this stage of the design would be subjected to. Additionally, any unwanted pitching motions could be counteracted by the thrusters mounted on the tips of the wing on the Baby Jay.

Once again, to achieve level 1 longitudinal stability, a gain was applied to C_{mq}. Using the same process as previously described, the value for k_{cmq} was determined to be 4.019 to have level 1 longitudinal handling qualities. Once the stability and control derivatives have been calculated by AAA, the software can then again determine the damping ratios and natural frequencies of the longitudinal and lateral directional modes encountered during flight. Table 22-6 below shows a list of the calculated stability metrics calculated by AAA. As it can be observed in this table, there are no time constants for the roll or spiral modes, which means that these modes will not be excited during flight.

Table 22-6: Baby Jay plus core stage stability and control metrics

Stability and control variable	Supersonic
Short Period Natural Frequency, ωnsp (rad/s)	2.356
Short Period Damping Coefficient, ζsp	0.421
Phugoid Natural Frequency, ωnph (rad/s)	0.0274
Phugoid Damping Coefficient, ζph	0.855
Dutch Roll Natural Frequency, ωndr (rad/s)	2.997
Dutch Roll Damping Coefficient, ζdr	0.152
Roll Mode Time Constant (s)	~
Spiral Mode Time Constant (s)	~
Static Margin (%)	6.75

Following the analysis of the dynamic modes of the Baby Jay plus Core, the trim diagram of the aircraft for the supersonic flight condition can be observed in Figure 21.13 below.

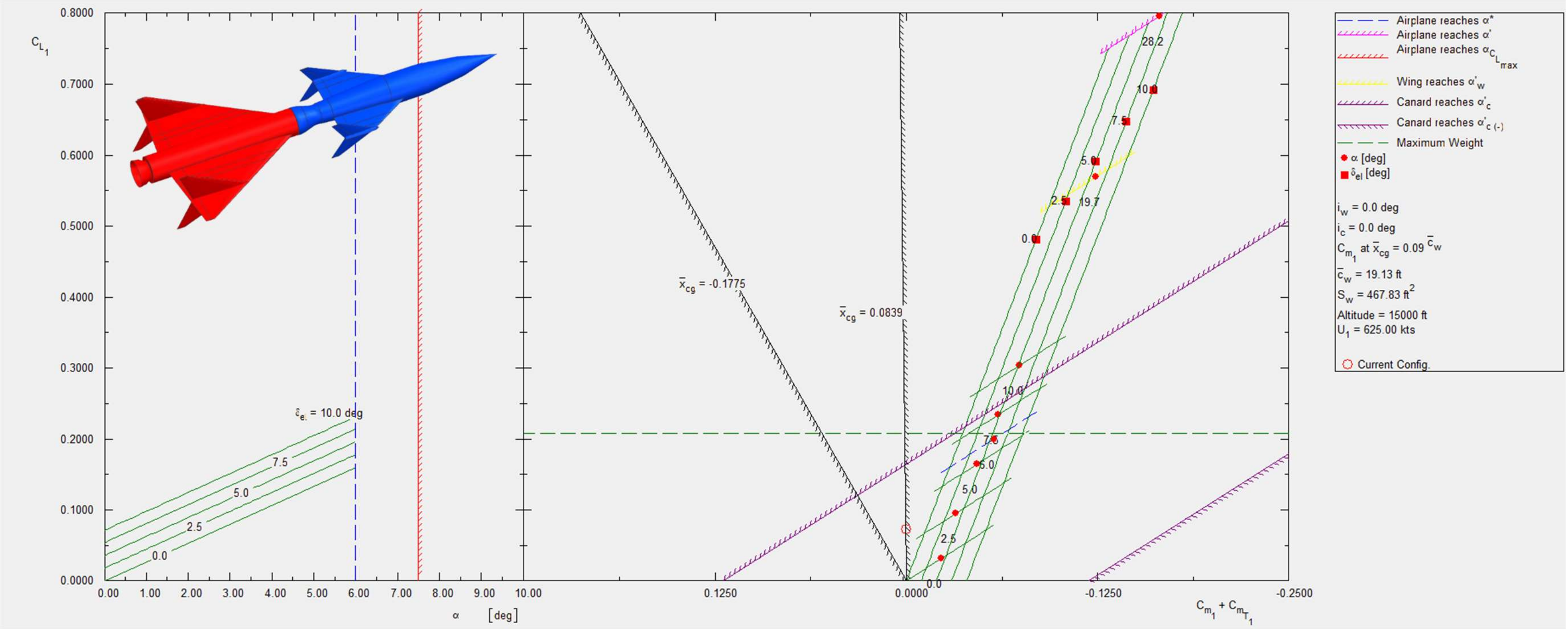

Figure 22.7: Baby Jay plus core trim diagram

Following the creation of the trim diagram, Figure 22.8 below shows the short period frequency requirement plot as created in AAA for the different levels of handling requirements. Because the design point is well within the level 1 boundaries, the Baby Jay plus SRB will have level 1 handling qualities for longitudinal motion.

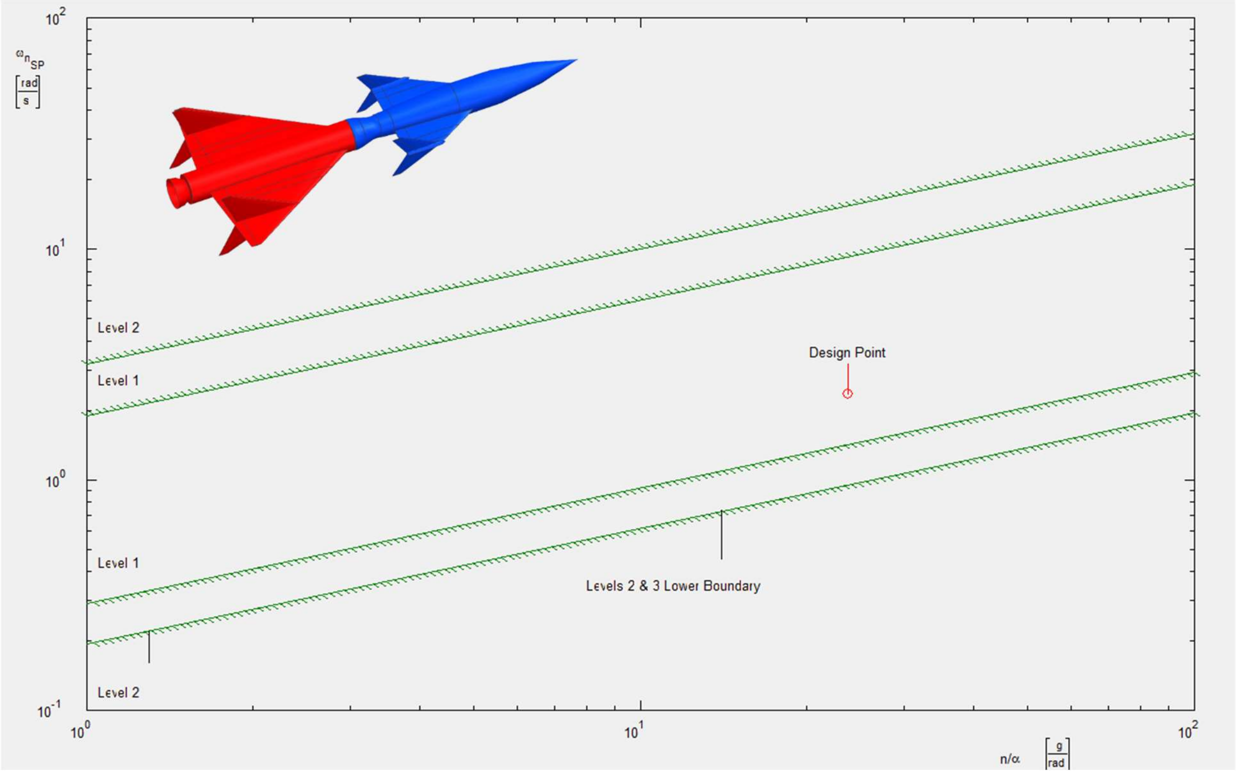

Figure 22.8: Baby Jay plus core short period frequency requirement plot

Similar to how the short period frequency plot was generated, the Dutch roll damping ratio and natural frequency plot can be created which can also be seen in Figure 22.9 below.

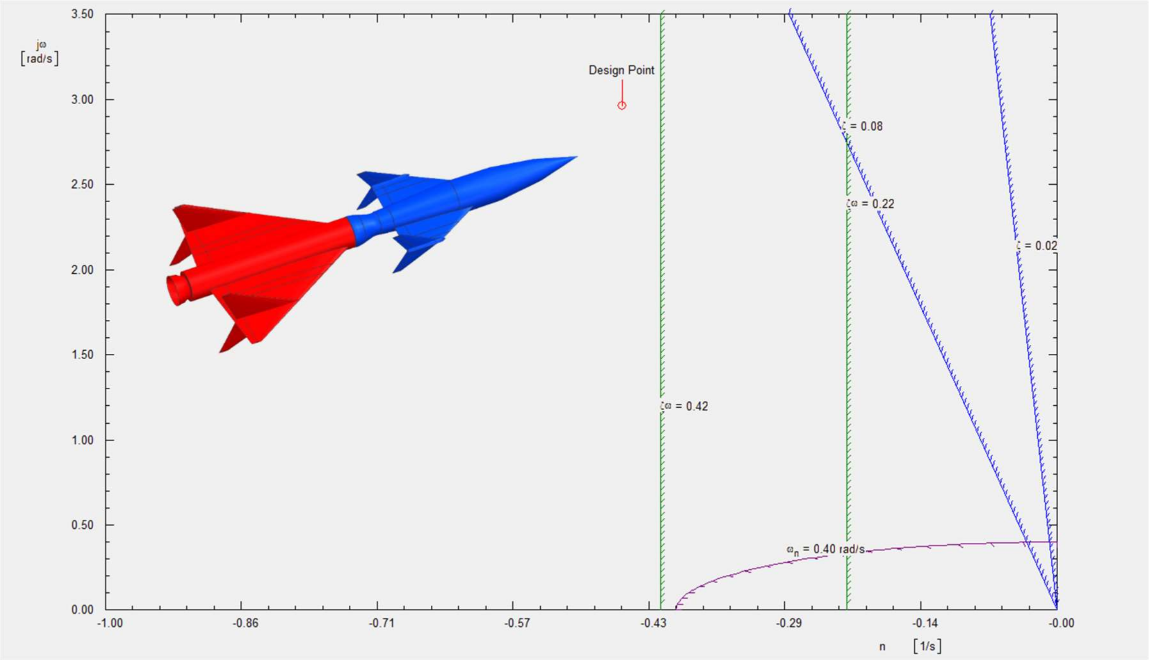

Figure 22.9: Baby Jay plus core stage Dutch roll frequency and damping ratio requirement plot

Finally, now that the core stage is evaluated, the Hyperhawk geometry can also be evaluated for its subsonic and supersonic flight conditions. For the core stage in both subsonic and supersonic flight conditions, the stability and control derivatives can be seen in Table 22-7 and Table 22-8 below.

Table 22-7: Hyperhawk longitudinal stability and control derivatives

Stability and control variable	Subsonic	Supersonic
Lift Coefficient due to Forward Velocity, C_{Lu}	0.446	0.782
Drag Coefficient due to Forward Velocity, C_{Du}	0.000	0.000
Pitching Moment Coefficient due to Forward Velocity, C_{mu}	0.065	-0.001
Lift Coefficient due to Angle of Attack, $C_{L\alpha}$ (rad^{-1})	3.704	2.990
Drag Coefficient due to Angle of Attack, $C_{D\alpha}$ (rad^{-1})	1.369	0.268
Pitching Moment Coefficient due to Angle of Attack, $C_{m\alpha}$ (rad^{-1})	-0.303	-0.115
Lift Coefficient due to Angle of Attack Rate, $C_{L\dot{\alpha}}$ (rad^{-1})	-0.023	2.789
Drag Coefficient due to Angle of Attack Rate, $C_{D\dot{\alpha}}$ (rad^{-1})	0.000	0.000
Pitching Moment Coefficient due to Angle of Attack Rate, $C_{m\dot{\alpha}}$ (rad^{-1})	0.045	-2.607
Lift Coefficient due to Pitch Rate, C_{Lq} (rad^{-1})	1.453	4.860
Drag Coefficient due to Pitch Rate, C_{Dq} (rad^{-1})	0.000	0.000
Pitching Moment Coefficient due to Pitch Rate, C_{mq} (rad^{-1})	-7.225	-0.500
Lift Coefficient due to Elevator Deflection Angle, $C_{L\delta el}$ (rad^{-1})	0.1732	0.1606
Pitching Moment Coefficient due to Elevator Deflection Angle, $C_{m\delta el}$ (rad^{-1})	-0.162	-0.1504

Table 22-8: Hyperhawk lateral directional stability and control derivatives

Stability and control variable	Subsonic	Supersonic
Side Force Coefficient due to Side Slip Angle, $C_{y\beta}$ (rad^{-1})	-4.392	-4.596
Rolling Moment Coefficient due to Side Slip Angle, $C_{l\beta}$ (rad^{-1})	-0.763	-0.740
Yawing Moment Coefficient due to Side Slip Angle, $C_{n\beta}$ (rad^{-1})	1.097	1.272
Side Force Coefficient due to Side Slip Angle Rate, $C_y\dot{\beta}$ (rad^{-1})	-6.229	-2.289
Rolling Moment Coefficient due to Side Slip Angle Rate, $C_l\dot{\beta}$ (rad^{-1})	1.975	0.448
Yawing Moment Coefficient due to Side Slip Angle Rate, $C_n\dot{\beta}$ (rad^{-1})	-4.497	-1.013
Side Force Coefficient due to Roll Rate, C_{yp} (rad^{-1})	0.930	0.619
Rolling Moment Coefficient due to Roll Rate, C_{lp} (rad^{-1})	-0.522	-0.208
Yawing Moment Coefficient due to Roll Rate, C_{np} (rad^{-1})	-0.513	-0.345
Side Force Coefficient due to Yaw Rate, C_{yr} (rad^{-1})	3.437	3.800
Rolling Moment Coefficient due to Yaw Rate, C_{lr} (rad^{-1})	-0.764	-0.724
Yawing Moment Coefficient due to Yaw Rate, C_{nr} (rad^{-1})	-1.686	-1.949
Side Force Coefficient due to Aileron Deflection Angle, $C_{y\delta el}$ (rad^{-1})	0.000	0.000
Rolling Moment Coefficient due to Aileron Deflection Angle, $C_{l\delta el}$ (rad^{-1})	0.064	0.056
Yawing Moment Coefficient due to Aileron Deflection Angle, $Cn\delta el$ (rad^{-1})	-0.002	-0.001
Side Force Coefficient due to Rudder Deflection Angle, $Cy\delta r$ (rad^{-1})	0.545	0.380
Rolling Moment Coefficient due to Rudder Deflection Angle, $Cl\delta r$ (rad^{-1})	-0.163	-0.087
Yawing Moment Coefficient due to Rudder Deflection Angle, $Cn\delta r$ (rad^{-1})	-0.358	-0.247

These specific stability and control variables are significant because they dictate whether the designed aircraft will be laterally, directionally, and longitudinally stable based upon the signs of the values. To have lateral and longitudinal stability, the values for $C_{l\beta}$ and $C_{m\alpha}$ should both be negative while directional stability requires $C_{n\beta}$ to be positive. As it can be observed by the above tables, the values, in both subsonic and supersonic conditions, for $C_{l\beta}$, $C_{n\beta}$, $C_{m\alpha}$ are reported to have the proper signs for their respective stability requirements.

It should also be noted that to achieve level 1 longitudinal stability, a gain was applied to C_{mq}. To determine that this gain should be, the same iterative design process was performed in AAA until the desired handling requirements were met. Upon further analysis, the value for k_{cmq} was determined to be 0.4307 for supersonic flight to have level 1 longitudinal handling qualities, while there was no such gain needed for subsonic flight conditions.

Once the stability and control derivatives have been calculated by AAA, the software can then determine the damping ratios and natural frequencies of the longitudinal and lateral directional modes encountered during flight. Table 22-9 below shows a list of the calculated stability metrics calculated by AAA for both the subsonic and supersonic flight conditions. As it can be observed in this table below, there is not a natural frequency nor damping ratio for the longitudinal short period mode in supersonic flight, this is because the dynamic mode is so damped that a short period mode simply does not exist for the Hyperhawk for supersonic conditions.

As it can be observed in this table, the subsonic case for the Hyperhawk has a static margin of negative 6.3%. Although, using the same equations shown above, a longitudinal feedback loop can be created for the Hyperhawk flight configuration to achieve de facto stability under the subsonic case when a value of -0.652 for k_α is used. Therefore, this feedback loop gives the aircraft de facto stability with a static margin of 10%. A similar process could be done for the supersonic Hyperhawk configuration, however, the static margin of 8.17% is close enough to the desired 10% static margin.

Table 22-9: Hyperhawk stability and control metrics

Stability and control variable	Subsonic	Supersonic
Short Period Natural Frequency, ωnsp (rad/s)	2.448	~
Short Period Damping Coefficient, ζsp	0.343	~
Phugoid Natural Frequency, ωnph (rad/s)	0.0307	2.172
Phugoid Damping Coefficient, ζph	0.386	0.189
Dutch Roll Natural Frequency, ωndr (rad/s)	5.128	5.367
Dutch Roll Damping Coefficient, ζdr	0.068	0.075
Roll Mode Time Constant (s)	1.265	1.929
Spiral Mode Time Constant (s)	14.033	6.658
Static Margin (%)	-6.30	8.17

Following the analysis of the dynamic modes of the Hyperhawk, the trim diagrams of the aircraft for subsonic and supersonic flight conditions can be observed in Figure 22.10 and Figure 22.11 respectively.

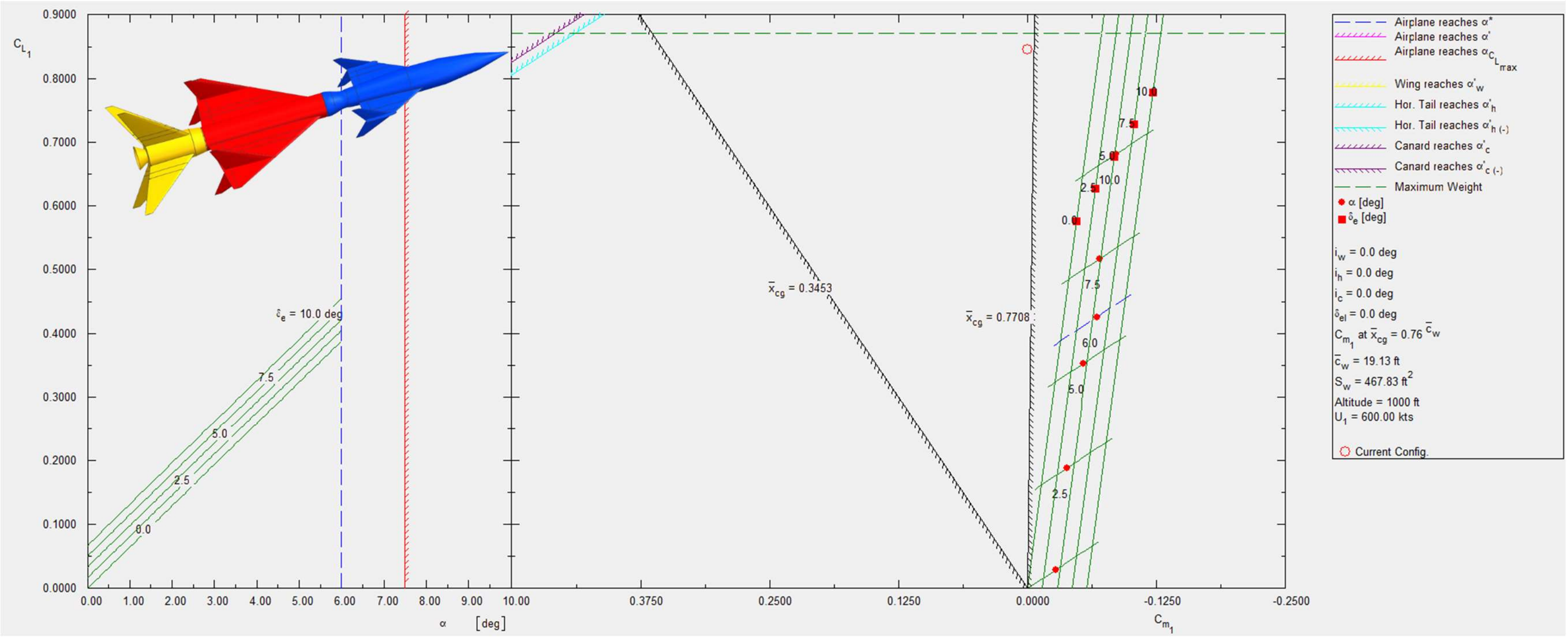

Figure 22.10: Hyperhawk subsonic trim diagram

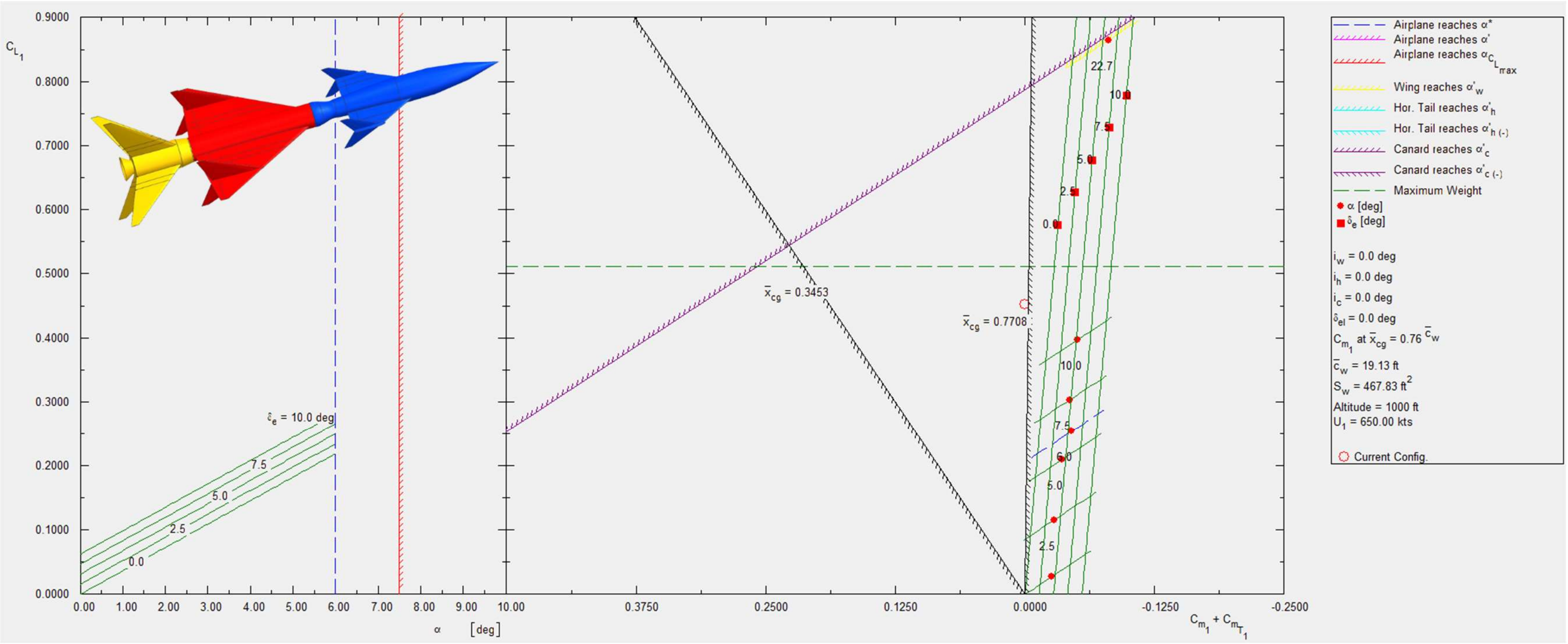

Figure 22.11: Hyperhawk supersonic trim diagram

Following the creation of the trim diagrams, Figure 22.12 below shows the short period frequency requirement plot as created in AAA for the different levels of handling requirements. Because there is no short period for the supersonic case of the Hyperhawk, the short period requirement plot for the supersonic flight condition is not shown, as there is no design point shown on the plot.

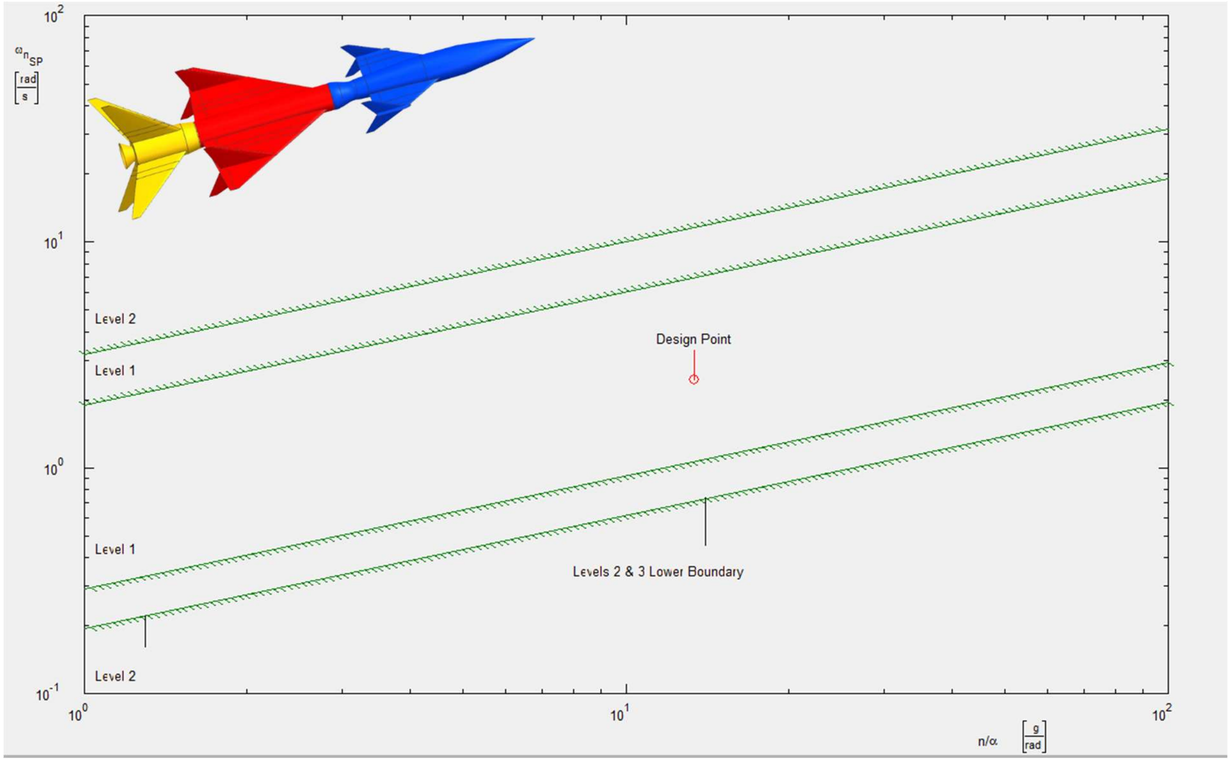

Figure 22.12: Hyperhawk subsonic short period frequency requirement plot

Similar to how the short period frequency plot was generated for the previous geometries, the Dutch roll damping ratio and natural frequency plots can be created which can also be seen in Figure 22.13 and Figure 22.14. It can be observed in these two figures that level one handling qualities are not achieved for the Hyperhawk. However, because the aircraft is axisymmetric, these lateral directional handling qualities can be ignored, as the design of the aircraft should mitigate any negative lateral directional modal effects.

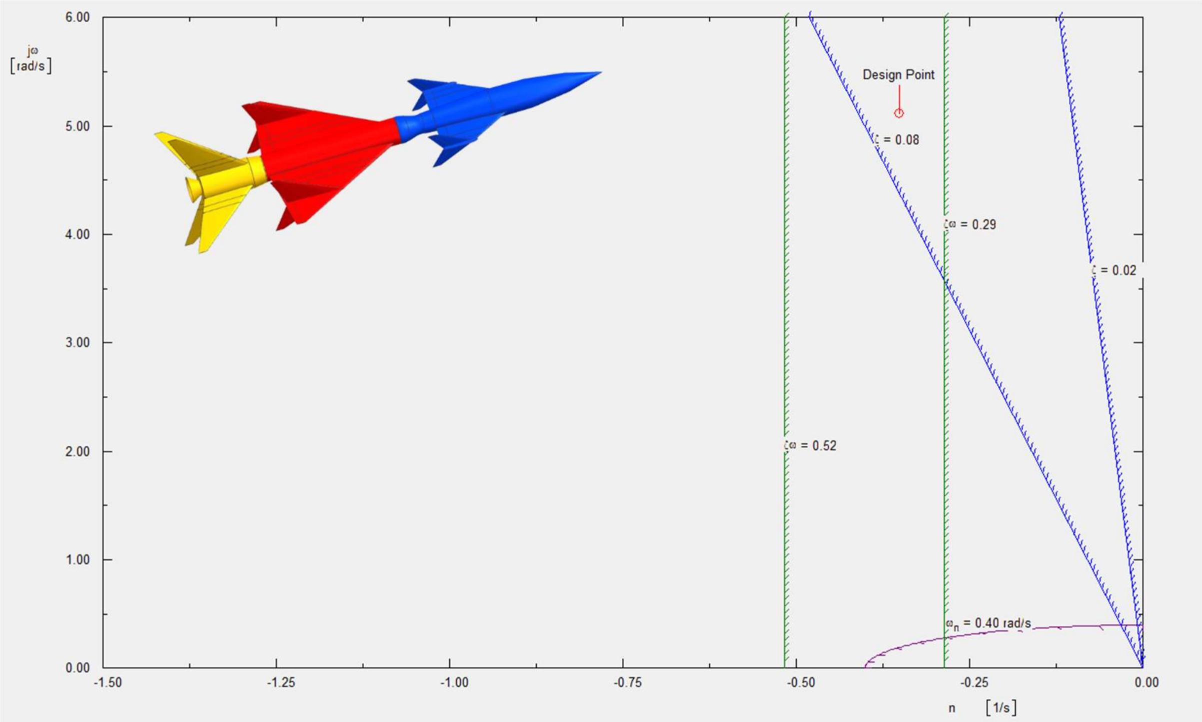

Figure 22.13: Hyperhawk subsonic Dutch roll frequency and damping ratio requirement plot

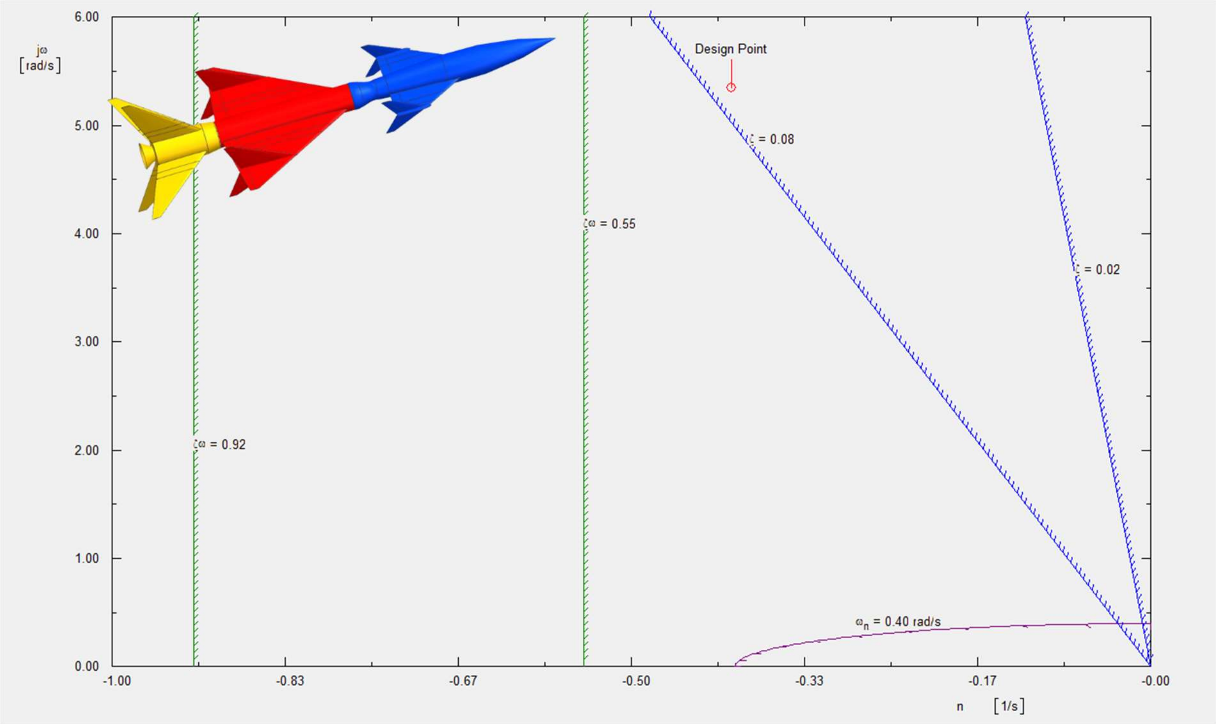

Figure 22.14: Hyperhawk supersonic Dutch roll frequency and damping ratio requirement plot

23. STRUCTURES

The substructures for the Baby Jay are shown below. The wings include 3 spars with ribs evenly spaced at 300mm intervals. Stringers will also be included to prevent skin buckling. The electrical and mechanical substructures will be integrated into the spars and ribs to allow usage of the control surfaces and propulsion systems.

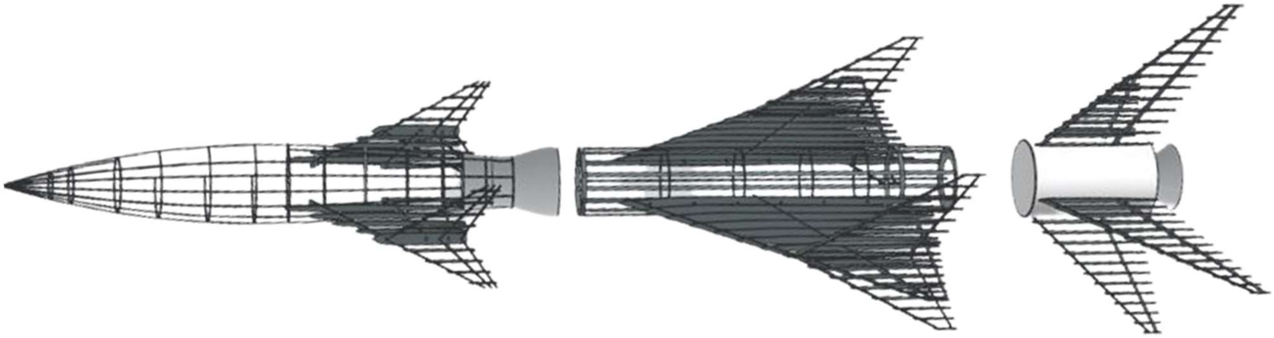

Figure 23.1: Substructure of the Hyperhawk

The primary decision maker for the materials used on the Baby Jay was reusability and ease of repair as this is the only stage completely reused each launch. The materials for the rest of the Hyperhawk were chosen primarily based on ease of manufacturing and low cost as they will not be reused. With this in mind, the core stage and solid rocket booster substructure was chosen to be aerospace grade aluminum to reduce weight and cost. The skin of these stages was chosen to be a graphite epoxy composite. These materials have proven flight heritage having been used on many launch vehicles like the Atlas V rocket and Falcon 9. For the Baby Jay the substructure and skin will use a ceramic carbon composite with aluminum honeycomb layers in order to keep weight at a minimum while also allowing for high heat tolerance to further aid in heat reduction.

24. COST ANALYSIS

The purpose of this chapter is to present the costs associated with the design presented in this report to meet the request for proposal and to compare its associated costs with other approaches. The cost analysis detailed by Roskam in *Airplane Design Part VIII* [15] was used to assess the total costs. Using these methods, a code was created to estimate the cost of the Hyperhawk platform. Because the three stages of the design are very different three separate costing codes where written and then a total cost could be calculated. In addition, this method allows for the cost of each individual component to be estimated to see where further improvements might be made and if a component was to be used on its own. This would be the case in the exo-atmospheric mission where the Baby Jay would be launched on a traditional rocket system.

For the solid rocket booster of the Hyperhawk platform 89 inches of the Atlas V AJ-60A booster is used. Because the design is reusing a well know and tested booster section (just a shortened version). The cost estimation is relatively simple. The Atlas V 401 has a price of 109 million USD [31] and is just the core stage of the Atlas V with no solid rocket boosters. The Atlas V 551 has a price of 153 million USD [31] and has 5 solid rocket boosters. Knowing these two prices the price of each of the 5 solid rocket boosters can be found to be approximately 8.8 million USD. The Hyperhawk platform only uses 89 inches of the 669 inches tall AJ-60A booster [32] (roughly 13% of the size). This means the Hyperhawk solid rocket booster can be estimated as 13% of the AJ-60A booster or 1.14 million USD.

Table 24-1: Solid rocket booster costs

RDT&E Cost (Million ($)	**AEP Cost (Million $)**
$ 0 (using known section of Atlas V so no RDT&E cost)	$1.14

Research, development, test and evaluation costs for the Hyperhawk core rocket stage are given in Table 24-2, Manufacturing, acquisition, operating, and total life cycle costs are given in Table 24-3.

Table 24-2: RDT&E Hyperhawk core rocket stage cost

RDT&E Stage	**Cost (Million $)**
Airframe Engineering Design Costs	$3,648
Development and Support Costs	$330
Flight Test Aircraft Cost	$843
Flight Test Operations Cost	$60
Test and Simulation Facilities Cost	$976
RDT&E Profit	$264
Cost to Finance RDT&E Phases	$306
Total RDT&E Cost	**$6,427**

Table 24-3: Hyperhawk core stage acquisition cost (100 airframes)

Cost of Acquisition Breakdown	Cost (Million $)
Acquisition Cost	$6,607
Manufacturing Profit	$601
Manufacturing Cost	$6,006
Airframe Engineering and Design Cost	$560
Cost of Engineering and Avionics	$560
Aircraft Program Production Cost	$4,545
Labor Cost for Manufacturing	$531
Estimated Cost Per Airframe	**$72**

Research, development, test and evaluation costs for the Baby Jay were also calculated. Table 24-2 shows the RDT&E cost while the manufacturing, acquisition, operating, and total life cycle costs are given in Table 24-5.

Table 24-4: RDT&E cost for Baby Jay

RDT&E Stage	Cost (Million $)
Airframe Engineering Design Costs	$2,551
Development and Support Costs	$207
Flight Test Aircraft Cost	$631
Flight Test Operations Cost	$26
Test and Simulation Facilities Cost	$683
RDT&E Profit	$184
Cost to Finance RDT&E Phases	$214
Total RDT&E Cost	**$4,496**

Table 24-5: Acquisition cost for Baby Jay (100 airframes)

Cost of Acquisition Breakdown	Cost (Million $)
Acquisition Cost	$6,251
Manufacturing Profit	$568
Manufacturing Cost	$5,683
Airframe Engineering and Design Cost	$391
Cost of Engineering and Avionics	$391
Aircraft Program Production Cost	$4,439
Labor Cost for Manufacturing	$397
Estimated Cost Per Airframe	**$67**

With the breakdown of each component of the Hyperhawk platform calculated a comparison can be made between the total cost of the Hyperhawk compared to the SR-71 (corrected for inflation) and a theoretical SR-72 (Mach 5) aircraft in the Figures below. These Figures clearly show how the Hyperhawk not only exceeds these competitors in performance but also in cost.

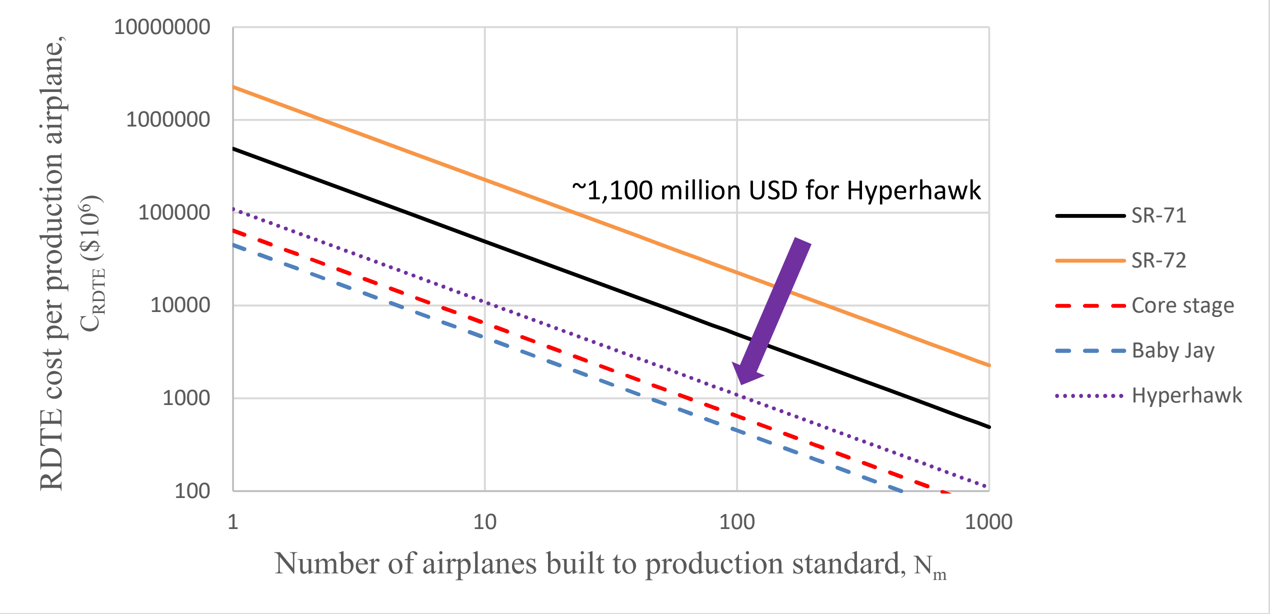

Figure 24.1: Substructure of the Hyperhawk

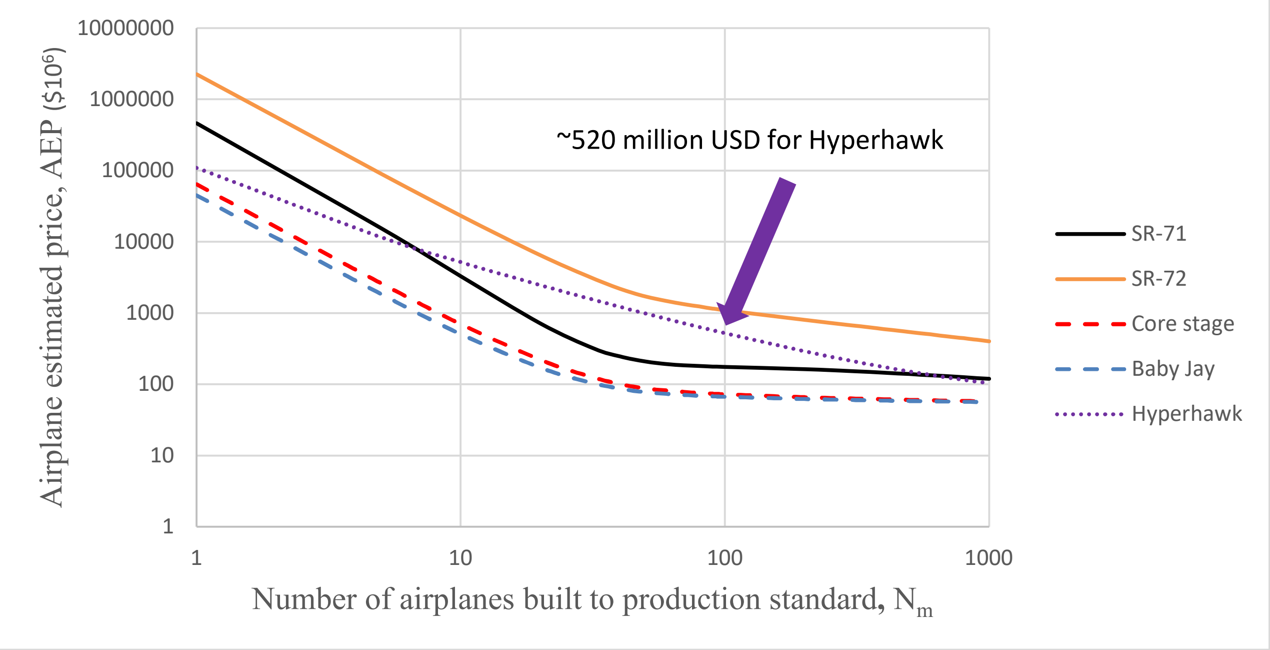

Figure 24.2: Substructure of the Hyperhawk

25. SHIPPING AND LAUNCHING INFASTRUCTURE

To meet the requirements in the RFP to be able to be launched from a traditional runway the Hyperhawk must be transported in its separate stages. In addition, the main wing on the cores stage and the tail on the solid rocket booster must be removed. As these stages are meant to separate in flight as well as the main wing as described in the mission profile of a previous chapter, no modification had to be made to the design. Figure 25.1 and Figure 25.2 below show this disassembly and transportation process for ground transportation and flight respectively.

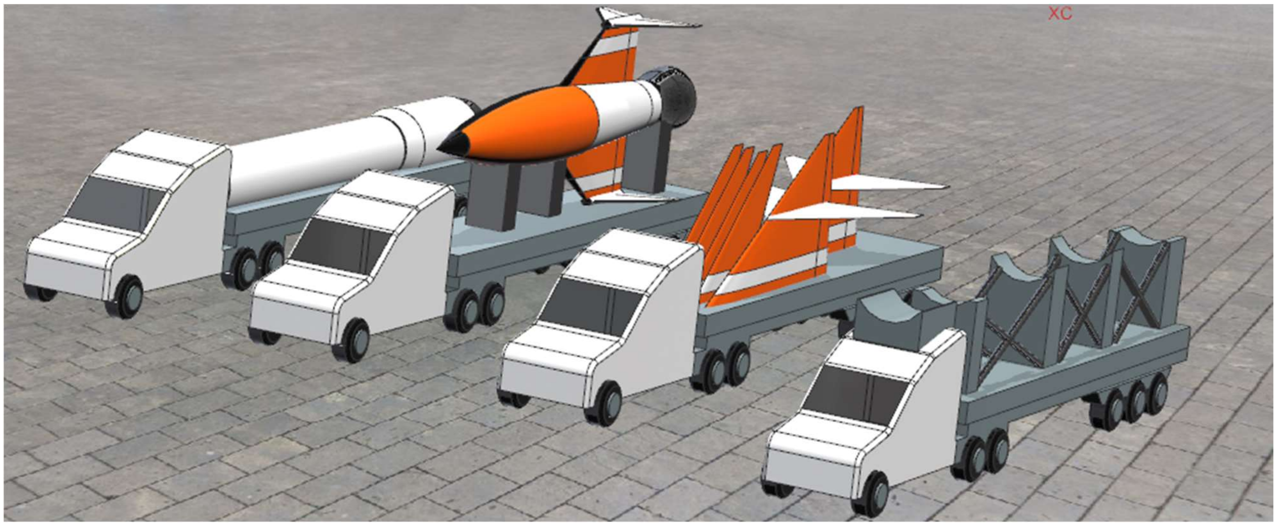

Figure 25.1: Hyperhawk disassembled for transportation on a semi-truck

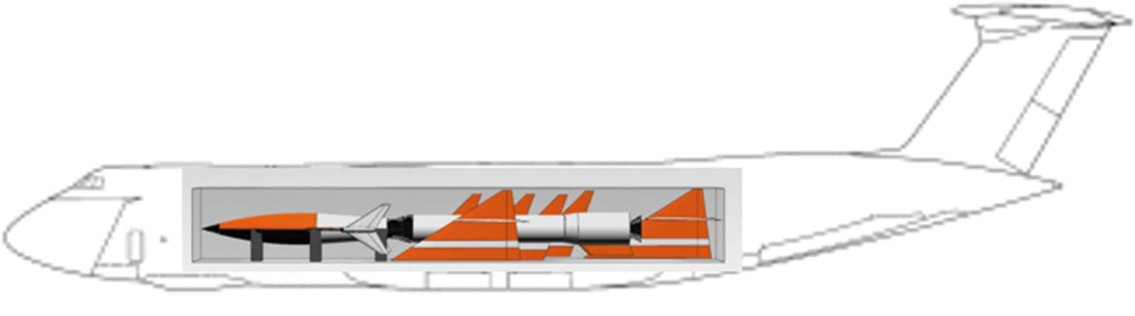

Figure 25.2: Hyperhawk disassembled for transportation in a C-5 galaxy cargo aircraft

In addition, provisions must be made to remove and service the ISR payload as well as replace it with munitions if so desired. Fortunately, to deploy solar panels for the exo-atmospheric mission, doors were previously designed above the payload. Using these doors while on the ground would easily facilitate the removal and replacement of the ISR payload. This can be seen in Figure 25.3 below.

Figure 25.3: ISR payload removal or replacement

Finally, to launch the Hyperhawk, a vertical launch system is required. Looking at historically, similar sized rockets have used a mobile vertical launch stand. This can be seen in below in Figure 25.4 where the Bomarc missile launch system is seen. It was decided that a similar system would both be inexpensive as well as simple for the Hyperhawk. This system is shown in Figure 25.5.

Figure 25.4: Bomarc missile transportation and launch systems [33,34]

Figure 25.5: Hyperhawk transportation and launch systems

REFERENCES

1. Anon., *2021-2022 Graduate Team Missile Systems Design Competition – Reusable Penetrating Hypersonic ISR Platform* 27 January 2022.
2. Anon., “Cold War in Space: Top Secret Reconnaissance Satellites Revealed,” *National Museum of the United States Air Force Web Site* [https://www.nationalmuseum.af.mil/] 27 January 2022.
3. Anon., “NASA Armstrong Fact Sheet: X-34 Advanced Technology Demonstrator,” *NASA Web Site* [https://www.nasa.gov/] 28 February 2014.
4. Anon, “X-37B Extended Space Flights,” *Boeing Web Site* [https://www.boeing.com/] 6 February 2022.
5. Anon, “Boeing X-37,” *Wikipedia Web Site* [https://en.wikipedia.org/] 22 January 2022.
6. Anon., “Lockheed U-2” *Wikipedia Web Site* [https://en.wikipedia.org/] 24 January 2022.
7. Sonawane, V., “U-2 Spy Plane Crash: Pilot Dead, Another Injured in Northern California,” *International Business Times Web Site* [https://www.ibtimes.com/] 21 September 2016.
8. Anon., “Lockheed SR-71 Blackbird” *Wikipedia Web Site* [https://en.wikipedia.org/] 27 January 2022.
9. Anon, “CIM-10 Bomarc,” *Wikipedia Web Site* [https://en.wikipedia.org/] 28 March 2022.
10. Bosco, Joseph, “International Law Regarding Outer Space – An Overview,” *Journal of Air Law and Commerce,* 1990.
11. Anon., “The Edge of Space,” *NASA Web Site* [https://www.nasa.gov/] 24 July 2021.
12. Anon, “Small Satellite Launchers” *New Space Web Site* [https://www.newspace.im/] 1 January 2022.
13. Roskam, Jan, *Airplane Design Part I: Preliminary Sizing of Airplanes*, Lawrence, KS, 2018.
14. Roberts, Kristen, "Analysis and design of hypersonic scramjet engine with a starting Mach number of 4.00," August 2008.
15. Roskam, Jan, *Airplane Design Part VIII: Airplane Cost Estimation: Design Development, Manufacturing, and Operating*, Lawrence, KS, 2018.
16. Wertz, James R., Everett, David F., Puschell, Jeffery J., “Space Mission Engineering: The New SMAD,” Torrance, CA, 2018, pp

17. Kaplinger, Brain, “Handout 2 - Budget Example,” February 2022.
18. Anon., “Propulsion Systems,” *NASA Web Site* [https://history.nasa.gov/] 14 February 2022.
19. Anon., “Monopropellant Rocket,” *Wikipedia Web Site* [https://en.wikipedia.org/] 14 February 2022.
20. Patel, Piyush., “What Is a Scramjet Engine,” *Science ABC Web Site* [https://www.scienceabc.com/] 14 February 2022.
21. Van Wie, David., D’Alessio, Stephen., White, Michael., “Hypersonic Airbreathing Propulsion,” [https://www.jhuapl.edu/] 14 February 2022.
22. Anon., “How Scramjets Work,” *NASA Web Site* [https://www.nasa.gov/] 14 February 2022.
23. Sutton, G. P., Biblarz, O., “Classification,” *Rocket Propulsion Elements,* 8th ed., Vol. 1, John Wiley & Sons, New Jersey, 2010, pp. 9–10.
24. Roskam, Jan, *Airplane Design Part VI: Airplane Calculation of Aerodynamic, Thrust and Power Characteristics*, Lawrence, KS, 2018.
25. Anon., “LauncherOne” *Wikipedia Web Site* [https://en.wikipedia.org/] 27 January 2022.
26. Nowlin, Samual, Luke, Thimons, “Surviving the heat: the application of phenolic impregnated carbon ablators” *University of Pittsburgh Swanson School of Engineering*, 1 February 2013.
27. Anon., “Glass and the space orbiter,” *Corning Museum of Glass,* [https://www.cmog.org] 8 December 2011.
28. Anon., “Technical Information Single Crystal Sapphire,” *AdValue Technology,* [https://advaluetech.com/].
29. Roskam, Jan, *Airplane Design Part V: Component Weight Estimation*, Lawrence, KS, 2018.
30. Roskam, Jan, *Airplane Design Part II: Preliminary Configuration Design and Integration of the Propulsion System*, Lawrence, KS, 2018.
31. Anon., “Atlas V,” *Wikipedia Web Site* [https://en.wikipedia.org/] 5 May 2022.
32. Anon., “AJ-60A,” *Wikipedia Web Site* [https://en.wikipedia.org/] 5 May 2022.
33. Anon., “The Bomarc Missile Controversy,” *Valour Canada,* [https://valourcanada.ca].
34. Anon., “Bomarc missile,” *Wikipedia Web Site* [https://en.wikipedia.org/] 5 May 2022.